Centimetric absolute localization using Unmanned Aerial Vehicles with airborne photogrammetry and on-board GPS

Mehdi Daakir

Mehdi Daakir. Centimetric absolute localization using Unmanned Aerial Vehicles with airborne photogrammetry and on-board GPS. Signal and Image processing. Université Paris-Est, 2017. English. NNT : 2017PESC1223 . tel-01789704

HAL Id: tel-01789704
https://theses.hal.science/tel-01789704
Submitted on 11 May 2018

Université Paris-Est

École Doctorale MSTIC
Mathématiques, Sciences et Technologies de l'Information et de la Communication

Thèse de Doctorat

pour obtenir le grade de

Docteur de l'Université Paris-Est
Spécialité : SIGNAL, IMAGE & AUTOMATIQUE

Présentée par
Mehdi DAAKIR

Localisation absolue centimétrique par photogrammétrie aéroportée et GPS embarqués sur drone

Directeur de thèse : Marc PIERROT DESEILLIGNY

préparée à Univ. Paris-Est/LaSTIG LOEMI/IGN/ENSG
&
Vinci Construction Terrassement/SIXENSE Mapping

Soutenue publiquement le 11 décembre 2017

Jury :

- Directeur de thèse :
  - Marc Pierrot Deseilligny - École Nationale des Sciences Géographiques
- Co-directeur de thèse :
  - Pierre Bosser - École Nationale Supérieure de Techniques Avancées Bretagne
- Examinateur :
  - Pascal Monasse - École Nationale des Ponts et Chaussées
- Rapporteurs :
  - Jan Skaloud - École Polytechnique Féderale de Lausanne
  - Ismael Colomina - GeoNumerics Barcelone
  - Pierre Grussenmeyer - Institut National des Sciences Appliqueés de Strasbourg
- Encadrant Industriel :
  - Yohann Rabot - SIXENSE Mapping
- Membre Invité :
  - Francis Pichard - Vinci Construction Terrassement

Paris-Est University

MSTIC Doctoral School
Mathématiques, Sciences et Technologies de l'Information et de la Communication

PhD Thesis

to obtain the title of

Docteur de l'Université Paris-Est
Speciality : Signal, Image & Automatic

Defended by
Mehdi Daakir

Centimetric absolute localization using Unmanned Aerial Vehicles with airborne photogrammetry and on-board GPS

Thesis Advisor: Marc Pierrot Deseilligny

prepared at Univ. Paris-Est/LaSTIG LOEMI/IGN/ENSG
&
Vinci Construction Terrassement/SIXENSE Mapping

defended on December 11, 2017

Jury :

- Advisor :
  - `Marc Pierrot Deseilligny` - École Nationale des Sciences Géographiques
- Co-advisor :
  - `Pierre Bosser` - École Nationale Supérieure de Techniques Avancées Bretagne
- Examiner :
  - `Pascal Monasse` - École Nationale des Ponts et Chaussées
- Reviewers :
  - `Jan Skaloud` - École Polytechnique Féderale de Lausanne
  - `Ismael Colomina` - GeoNumerics Barcelone
  - `Pierre Grussenmeyer` - Institut National des Sciences Appliqueés de Strasbourg
- Industrial Advisor :
  - `Yohann Rabot` - SIXENSE Mapping
- Invited Member :
  - `Francis Pichard` - Vinci Construction Terrassement

Vinci Construction Terrassement
SIXENSE Mapping
1, Rue du Docteur Charcot
91420 Morangis
France

Institut National de l'Information Géographique et Forestière
73, Avenue de Paris
94160 Saint-Mandé
France

École Nationale des Sciences Géographiques
Université Paris-Est
École Doctorale MSTIC
Département Études Doctorales
6, Avenue Blaise Pascal - Cité Descartes
Champs-sur-Marne
77454 Marne-la-Vallée Cedex 2
France

Acknowledgments

Puisque l'opportunité m'en est donnée ici, je souhaite dédier cette page à toutes les personnes qui ont contribué de près ou de loin à la réalisation de cette thèse.

Comment ne pas commencer par remercier en premier lieu Marc Pierrot Deseilligny, mon directeur de thèse. J'aimerai ici lui témoigner mon plus profond respect. Pour l'encadrement dont j'ai pu bénéficié et tout le savoir qu'il a pu me transmettre durant toutes ces années, je lui en serai éternellement reconnaissant. Je souhaite lui dire qu'il représente pour moi, ainsi que pour l'ensemble de l'équipe `MicMac`, un exemple de tous les jours, une personne qui fait honneur à l'esprit humain.

Je remercie vivement les membres du jury pour l'honneur qu'ils me font. Merci à Pascal Monasse d'avoir accepté d'examiner mon travail et à Jan Skaloud, Ismael Colomina et Pierre Grussenmeyer pour en être les rapporteurs.

Je remercie Francis Pichard, éternel autodidacte, pour m'avoir donné l'opportunité de réaliser ce travail au sein d'un grand groupe et dans des conditions plus qu'idéales. Je le remercie pour m'avoir inculqué le vrai sens du terrain et aussi pour la qualité de sa table. Je lui souhaite une retraite plus que méritée.

Merci à Yohann Rabot pour sa confiance et pour m'avoir permis de finir ma thèse dans les meilleures conditions en m'intégrant à l'équipe `SIXENSE Mapping`. Je le remercie sincèrement pour sa compréhension et pour toute son aide précieuse.

Je remercie mon co-directeur de thèse, Pierre Bosser, pour ses relectures minutieuses, ses critiques et surtout pour sa bienveillance. J'aimerai lui dire qu'il fut pour moi un enseignant admirable et un encadrant de thèse exceptionnel.

Je remercie Christian Thom, mon encadrant et chef de l'équipe `LOEMI` où j'ai en partie réalisé ma thèse dans des conditions parfaites. Je tiens à le remercier pour son accueil chaleureux.

Je remercie tous mes collègues : Vincent Tournadre, Giang Nguyen, Ewelina Rupnik, Jonathan Lisein, Ana-Maria Rosu, Mariam Samaan, Jeremey

Belveaux, Mathieu Devaux, Gerald Choqueux et particulièrement Yilin Zhou pour le travail que nous avons conjointement mené durant ma dernière année et son investissement remarquable. Je remercie aussi tous les membres de l'équipe `LOEMI`: Jean-Philippe Souchon, Jean-Michael Muller, Christophe Meynard, Yann Le Borgne, Ahmad Audi, Amjad Lasri avec une pensée particulière pour Olivier Martin, sans qui tout ce travail n'aurait jamais existé. Je le remercie pour le temps qu'il a pu consacrer à tous mes problèmes, pour sa patience, sa bonne volonté et pour sa gentillesse qui n'a d'égale que son talent.

Aussi, je remercie tous mes collègues du côté de `Vinci Construction Terrassement` et de `SIXENSE Mapping` : Emmanuel Elaudais, Nicolas Gaucher, Denis Mettaie, Benjamin Grigoroff, Pierre-Marin Fabry, Mathieu Peyréga, Phillipe Guillenau et Thomas Nallet.

Je tiens à remercier tout le personnel de l'`ENSG` et leur exprime toute ma gratitude pour l'enseignement de qualité et les conditions de travail dont j'ai pu bénéficié durant toutes ces années. Mes remerciements vont en particulier au `DIAS` et au `DPTS` ainsi qu'à l'équipe des Travaux Spéciaux à Saint-Mandé.

Enfin, je remercie tous mes proches, mes amis et ma famille. Mes parents pour leur sens du sacrifice, mes sœurs que je n'ai pas assez vu grandir et Sofia pour son soutien sans faille.

"Les hommes naissent et demeurent libres et égaux en droits."
Article 1^{er} de la Déclaration des Droits de l'Homme et du Citoyen de 1789.

RÉSUMÉ

Au cours de la dernière décennie, les drones ont largement été utilisés dans divers domaines d'applications civils comme notamment la cartographie ou l'inspection. La photogrammétrie aéroportée sur drone occupe une place considérable dans une grande partie de ces applications, et est aujourd'hui utilisée comme une solution simple et efficace de modélisation 3D à des fins métrologiques. `Vinci Construction Terrassement` est une entreprise privée spécialisée dans le secteur des travaux publics qui intègre depuis 2013 les drones et la photogrammétrie comme une solution de cartographie et de suivi de ses chantiers de terrassement. `SIXENSE Mapping`, l'une de ses filiales, utilise ces mêmes outils plutôt à des fins de surveillance et de suivi d'évolution de grands ouvrages d'art. Le drone et la photogrammétrie s'avèrent être des outils très utiles, par exemple, pour le levé de stocks, pour le suivi temporel de zones spécifiques avec un risque de glissement de terrain (zones généralement inaccessibles) ou pour le relevé exhaustif des défauts d'ouvrages de grandes dimensions. Le but de ce travail de recherche est d'arriver à une mise en référence des acquisitions réalisées par drone en s'appuyant uniquement sur un récepteur `GPS` embarqué avec au plus 1 point terrain utilisé lors de la fusion des données multi-capteurs. En l'occurrence, pour le récepteur `GPS`, c'est le `GéoCube` développé au laboratoire d'instrumentation de l'`IGN` qui est utilisé, tandis que la captation des images est réalisée avec la `CamLight`, une caméra légère développée également au sein de ce même laboratoire. L'enjeu est d'arriver à un système léger, à faible coût comparé aux solutions commerciales existantes, et permettant d'atteindre une précision de localisation centimétrique.

De manière indépendante, ce travail de recherche aborde la problématique de la déformation des images par effet thermique du capteur. Nous montrons que la température du capteur au moment de la prise de vue, induit un effet de déformation sur la géométrie des images. Cet effet existe, est modélisable et sa prise en compte permet d'améliorer la précision géométrique finale en photogrammétrie.

Mots-clés

Drones; Photogrammétrie; `GPS`; Calibration; Bras de levier; Synchronisation temporelle; Fusion de données; Déformation thermique;

SUMMARY

Over the past decade, drones have been widely used in various fields of civilian applications such as mapping or inspection. `UAV` airborne photogrammetry occupies a considerable place in many of these applications and is nowadays used as a simple and efficient 3D modeling solution for metrological purposes. `Vinci Construction Terrassement` is a private company specializing in the public works sector which first integrated drones and photogrammetry in 2013 as a solution for mapping and monitoring of its earthworks. `SIXENSE Mapping`, one of its subsidiaries, uses these same tools rather for the purpose of inspecting and monitoring the evolution of large civil engineering structures. `UAVs` and photogrammetry are very useful, for example, for stock surveying, for temporal monitoring of specific areas with a risk of landslides (generally inaccessible areas) or for the exhaustive survey of large dimension structures. The aim of this research is to achieve the georeferencing of the acquisitions made by drone, relying on an embedded `GPS` receiver with at most 1 ground control point used during the multi-sensor data fusion. In this case, for the `GPS` receiver, the `GéoCube` developed in the `IGN`'s instrumentation laboratory is used, while image acquisition is done with `CamLight`, a light camera developed within this same laboratory. The challenge is to obtain a lightweight, low-cost system compared to existing commercial solutions, and achieve centimeter accuracy.

Independently, this research also addresses the problem of deformation of images induced by the thermal effect of the sensor. We show that the temperature of the sensor at the moment of the acquisition, induces a deformation effect on the geometry of the images. This effect exists, can be modeled and taking it into account improves the photogrammetry geometric accuracy.

Keywords

`UAVs`; Photogrammetry; `GPS`; Calibration; Lever-arm; Time synchronization; Data fusion; Thermal deformation;

Abbreviations

IGN: Institut national de l'information géographique et forestière
SGA: Service Géographique de l'Armée
LaSTIG: Laboratoire des Sciences et Technologies de l'Information Géographique
COGIT: Cartographie et Géomatique
LAREG: LAboratoire de Recherche en Géodésie
LOEMI: Laboratoire d'Opto-électronique et de Métrologie et d'Instrumentation
MATIS: Méthodes d'Analyses pour le Traitement d'Images et la Stéréorestitution
ENSG: École Nationale des Sciences Géographiques
PPMD: Photogrammétrie, Positionnement et Mesure de Déformations
CIFRE: Convention Industrielle de Formation par la Recherche
VCT: Vinci Construction Terrassement
GTM: Grands Travaux de Marseille
SEA: Sud Europe Atlantique

API: Application Programming Interface
GUI: Graphical User Interface
CUI: Command-line User Interface
KML: Keyhole Markup Language

GNSS: Global Navigation Satellite System
GPS: Global Positioning System
QZSS: Quasi-Zenith Satellite System
SBAS: Satellite-Based Augmentation System
C/A: Coarse/Acquisition
SNR: Signal-to-Noise Ratio
ECEF: Earth-Centred Earth-Fixed
TOW: Time Of Week
RTK: Real Time Kinematics
RINEX: Receiver Independent Exchange Format
BINEX: BINary EXchange
NMEA: National Marine Electronics Association
RTCM: Radio Technical Commission for Maritime Services
NTRIP: Networked Transport for RTCM via Internet Protocol
TCP/IP: Transmission Control Protocol/Internet Protocol
CORS: Continuously Operating Reference Station
IGS: International GNSS Service
PPP: Precise Point Positioning
PRN: Pseudo-Random Noise
LIDAR: LIght Detection And Ranging

IMU: Inertial Measurement Unit
OEM: Original Equipment Manufacturer

UAV: Unmanned Aerial Vehicle
UAS: Unmanned Aerial System
RTF: Ready to Fly
ULM: Ultralight aviation

CMOS: Complementary Metal Oxide Semiconductor
GSD: Ground Sampling Distance
SIFT: Scale-Invariant Feature Transform
ANN: Approximate Nearest Neighbor
BBA: Bundle Block Adjustment
SFM: Structure From Motion
GCP: Ground Control Point
SGM: Semi-Global Matching
DSM: Digital Surface Model
MAE: Mean Absolute Error

Contents

1 Introduction - Version Française 1

1.1 Résumé Long 1
1.2 Organisation du document 9

2 Introduction 11

2.1 Context 12
  2.1.1 National Institute of Geographic and Forestry Information 13
  2.1.2 Vinci Construction Terrassement 14
  2.1.3 SIXENSE Mapping 15
2.2 UAVs systems & Regulation 16
  2.2.1 A brief history of drones 16
  2.2.2 Civilian drones today 18
  2.2.3 Regulation in France 21
2.3 Needs & Challenges 21
  2.3.1 Needs in the context of Public Works 21
  2.3.2 Aims & Objectives 23
2.4 Organization of the thesis 26
2.5 Contributions of the thesis 28

3 Literature Review, Hardware & Software 33

3.1 Introduction 34
3.2 Contactless Metrology Techniques 34
  3.2.1 Topometric Instruments 35
  3.2.2 GNSS 36
  3.2.3 LIDAR 38
  3.2.4 Photogrammetry 39
    3.2.4.1 Interior Orientation 41
    3.2.4.2 Thermal Deformation 42
    3.2.4.3 Exterior Orientation 44
    3.2.4.4 Georeferencing Techniques 46
3.3 Hardware 48
  3.3.1 Off-the-shelf Solutions 49
  3.3.2 IGN lightweigth metric camera 50
  3.3.3 IGN GeoCube 53
  3.3.4 UAV platform 54
3.4 Software 54
  3.4.1 MicMac 54

3.4.2 RTKLib 57

4 Integrated Sensor Orientation 61
4.1 Introduction 62
4.2 Calibration aspects 63
4.2.1 Intrinsic Camera Calibration 63
4.2.2 Lever-Arm Calibration 64
4.2.2.1 Auto-calibration method 65
4.2.2.2 Pseudo-materialization method 68
4.2.2.3 Conclusion 75
4.2.3 Synchronization Issue 77
4.2.4 GPS positions & Camera Centers matching 81
4.3 Data Fusion 84
4.4 Experimental Data 87
4.4.1 Calibration flight 88
4.4.2 Second flight 88
4.4.3 GCPs Vs GPS 89
4.5 Conclusion 91

5 Thermal deformation on images 93
5.1 Introduction 94
5.2 Algorithmic aspect 95
5.2.1 Image correlation 95
5.2.2 Thermal model 96
5.2.3 Space resection 97
5.2.4 Dataset processing workflow 99
5.3 Calibration experiments 99
5.3.1 2D Matching 99
5.3.2 Static space resection 106
5.3.3 Standard space resection 108
5.4 Experimental evaluation 110
5.4.1 Terrestrial photogrammetric acquisition 110
5.4.1.1 Standard configuration results 112
5.4.1.2 Single strip configuration results 114
5.4.2 Airborne photogrammetric acquisition 115
5.5 Conclusion 120

6 Conclusions & Perspectives 125
6.1 Conclusions 125
6.2 Perspectives 127

A MicMac Installation 129

B Integrated Sensor Orientation Workflow **133**

C Thermal Deformation Workflow **151**

Bibliography **159**

List of Figures

2.1 Aerial acquisition on a `B17` in 1947 ; source: `www.ign.fr` . . . 13
2.2 `CamV2` (left), `GéoCube` (center) and `CamLight` (right) ; source: `http://loemi.recherche.ign.fr/` 14
2.3 Aerial view of part of a stretch of the `SEA` line; source: `Vinci Construction Terrassement` 15
2.4 Example of a silo 3D model and mapping of orthoimage disorders; source: `SIXENSE Mapping` 16
2.5 Aerial Target in 1920 (left) source: `http://www.ctie.monash.edu/`, Hewitt-Sperry Automatic Airplane in 1918 (center) source: `https://en.wikipedia.org/wiki/Hewitt-Sperry_Automatic_Airplane` and Max Boucher in 1912 (right) source: `http://www.corpusetampois.com/` 17
2.6 3D model of an air cooler (left, source: `SIXENSE Mapping`), 3D model of Chambord castle (center, source: `ENSG`) and canopy model (right, source: [Lisein 2016]) 18
2.7 Market share of civilian drone manufacturers registered in the `USA` ; source: `http://carnets-davenir.com` 20
2.8 Panorama of `UAV` models widely used today ; source: manufacturers' respective websites 20
2.9 Scenarios of flights of drones in France ; source: `http://www.drones-lab.com` 22
2.10 Map of `UAV` flight areas with restrictions in France ; source: `www.geoportail.gouv.fr` 22
2.11 Systematic use of the drone for the calculation of a stock volume of material ; source: `Vinci Construction Terrassement` . . 23
2.12 Different sensors used with the `Pixhawk` flight controller ; source: `www.escadrone.com` 25
2.13 Modified `Mission Planner` interface (left) and `MicMac` interface (right) ; source: `Vinci Construction Terrassement` . . 25
2.14 `IRIS+` `UAV` model manufactured by `3D Robotics` (left ; source: `Vinci Construction Terrassement`) and `DJI-Phantom 4 Pro` (right ; source: `www.dji.com`) 26

3.1 Evolution of stations in topometry. Theodolite (right), tachometer (center) and total station (right) 35
3.2 The double-difference geometry at a single epoch t_k 37

3.3 Principle of laser scanning mechanisms: rotating polygon wheel (a), single-channel oscillating mirror (b), and dual-channel oscillating mirror (c); source: `ww.riegl.com` 39
3.4 The geometry of a pinhole camera; source: [Moulon 2014] . . . 45
3.5 Panel of off-the-shelf solutions 50
3.6 An image of `CamLight` 51
3.7 Examples of shearing effect 52
3.8 `IGN GéoCube` 53
3.9 `UAV` prototype developed during our work 54
3.10 `MicMac` logo (left) and the famous banner displayed at the end of each processing step (right) 56
3.11 Organization of `MicMac` in different layers; source: [Rupnik *et al.* 2017] 56
3.12 Satellite visibility analysis under `RTKPLOT` application 59

4.1 Visualization of the spatial offset (in red) between the optical center of the camera and the antenna phase center; source: `LOEMI` 65
4.2 Variation of lever-arm estimation value per number of used `GCPs` 67
4.3 Targets on sensors: the `GéoCube` (left) and `CamLight` (right) . 68
4.4 Photogrammetric acquisition around the `UAV` on-board camera 69
4.5 Photogrammetric acquisition of the `UAV`'s on-board `GPS` receiver 69
4.6 The circular acquisition geometry for camera optical center calibration 70
4.7 Images acquired around the `GPS` receiver for antenna phase center calibration 71
4.8 Planimetric variation of the antenna phase center 72
4.9 Photogrammetric acquisition around `UAV` before take-off (left) and image geometry acquisition (right) 73
4.10 residuals of exterior orientation positions determined by `GPS` with the lever-arm pseudo-materialization method 75
4.11 Comparison of absolute residuals using two different lever-arm calibration techniques 76
4.12 Adapting `Sony-RX1` camera triggering to `GPS` module `TimePulse` feature 78
4.13 Measurement of electronic delay with an oscilloscope: between `GPS` and `IGN` light camera (left) and `Sony-RX1` (right) 79
4.14 Measurements of electronic delay stability with time difference pulses: `IGN` light camera (left) and `SONY-RX1` (right) 79
4.15 Comparison of residuals with and without taking delay into account. Planimetric components (left and center) and vertical component (right). 81

4.16 Trajectories in various frames with different sampling 82
4.17 Correlation values between ratios distances curves after testing different temporal offset values 84
4.18 Data fusion processing workflow 85
4.19 Flight plan (left), panel of images (center) and acquisition geometry (right) 88
4.20 Comparison between both point clouds using `CloudCompare` . 91

5.1 General pipeline for thermal deformation modeling 98
5.2 General workflow for data processing 100
5.3 The scene of the textured wall (left) and the installation of cameras and peltier cooler (right) 101
5.4 An example of a correlation map (left) and a 2D deformation map (right) 102
5.5 Temperature variation in Type I acquisition: dataset 1-4 (left to right, top to bottom) 103
5.6 Estimation result of translation: dataset 1-3 (from left to right) 104
5.7 Estimation result of rotation: dataset 1-3 (from left to right) . 104
5.8 Estimation result of focal length: dataset 1-3 (from left to right) 105
5.9 One of the deformation maps of the investigated image couples 105
5.10 Image of the scene with equipped GCPs (left) and variation of temperature (right) 106
5.11 `GCP` re-projection error of the first image and mean `GCP` re-projection error of all images 108
5.12 Evolution of estimated focal length and principal point values. 108
5.13 Panel of acquired images (left) and geometry of acquisition (right). Camera positions (green) and 3D positions of `GCPs` (red). 109
5.14 `GCP` reprojection error 110
5.15 Estimated values of focal length and principal point. 111
5.16 Dataset around a pylon 111
5.17 Geometry of terrestrial photogrammetric acquisition with `GCPs` (blue) 113
5.18 Residuals on `GCPs` 113
5.19 Demonstration of image overlapping situation: a single strip configuration is simulated when no tie point extraction is performed for image couples indicated with a red line 114
5.20 Closing error in the terrestrial photogrammetric acquisition on tie point quadruplets 115
5.21 Terrestrial images on a 3D scene for camera calibration 116

5.22 Geometry of acquisition for camera model calibration and `GCP` distribution (left), mean `GCPs` re-projection error (right) 117
5.23 Comparison of the two estimated internal camera models . . . 118
5.24 Panel of acquired corridor dataset (top) and image temperature variation (bottom). 119
5.25 Geometry of corridor acquisition and distribution of `GCPs` along the scene (in purple). 120
5.26 Geo-referencing residuals on each `GCP` for both raw and corrected images 121

B.1 Panel of Images of the dataset 134
B.2 Tie points visualization using `mm3d SEL` command 137
B.3 3D visualization of exterior orientation 138
B.4 Drawing a mask 148
B.5 Orthoimage 149
B.6 Shading image 149
B.7 Hypsometric image 150

C.1 Sample of calibration images acquisition 152
C.2 Deformation Map along x axis between a pair of images 153
C.3 Geometry of acquisition 156

List of Tables

1.1 Panel de capteurs utilisés dans des applications de drones civils 2
1.2 Panel de quelques solutions logicielles photogrammétriques . . 3
1.3 Comparaison des techniques de géoréférencement selon différents critères 7

2.1 Comparison between the two categories of drones according to six performance criteria ; source: [Eisenbeiß 2009] 19

3.1 Comparison of `UAV` off-the-shelf solutions with respect to different criteria 49

4.1 Correlation values between lever-arm, focal and principal point parameters 67
4.2 Different estimates of values of the lever-arm offset 74
4.3 Residuals on check points depending on processing strategies . 85
4.4 Standard deviations of parameters for different strategies . . . 86
4.5 Residuals on check points for fligh calibration parameters . . . 89
4.6 Residuals on check points for second flight 90

5.1 Selected parameters for the correlator 96
5.2 Information of 2D matching datasets 102
5.3 Information of image couples 102
5.4 Statistics of image couple deformation 105
5.5 Information on static space resection dataset 107
5.6 Information on standard space resection datasets 109
5.7 `GCP` re-projection error and estimated focal length and principal point 110
5.8 Information on terrestrial dataset 112
5.9 2 Cases of the terrestrial dataset 112
5.10 Statistics of geo-referencing residuals on `GCPs` 112
5.11 Closing error of the terrestrial acquisition 115
5.12 Information on terrestrial calibration dataset 116
5.13 Information about aerial dataset 119
5.14 Geo-referencing residuals on `GCPs` for airborne dataset 120

CHAPTER 1

Introduction - Version Française

Contents

1.1 Résumé Long 1
1.2 Organisation du document 9

1.1 Résumé Long

Le contexte de notre travail de recherche se situe à la croisée de plusieurs domaines technologiques en pleine révolution. Depuis le début des années 2000, nous assistons au développement de vecteurs aériens légers (hélicoptères, `ULMs`, drones, ...), au développement de capteurs embarqués et de leur miniaturisation ainsi qu'à l'apparition de solutions algorithmiques totalement automatiques de modélisation 3D basées sur la captation d'images. Plus particulièrement, le développement des applications aériennes utilisant des drones civils connaît une révolution spectaculaire depuis la dernière décennie. En France, une réglementation aérienne a fait son apparition dès 2012 afin d'encadrer l'utilisation d'aéronefs télé-pilotés à distance. Cela a permis l'émergence d'un nouveau secteur d'activité ainsi que l'apparition de différents constructeurs de drones civils (semi) professionnels. Les domaines d'applications sont très variés, comme l'architecture, l'agriculture, la topométrie, la surveillance d'ouvrages ou de zones à risques,... La photographie aérienne se positionne aujourd'hui comme une des techniques les plus utilisées dans ce secteur, que ce soit pour des images à vocation médiatique, pour de l'inspection (dans le domaine visible ou infra-rouge thermique) ou bien plus généralement pour de la cartographie. C'est dans ce contexte que la photogrammétrie aérienne connaît un regain d'intérêt considérable. En effet, en embarquant sur un drone un appareil photo grand public de bonne qualité, et sans savoir-faire particulier, il est aujourd'hui possible de réaliser de manière 100% automatique des modélisations visuellement parfaites de la scène survolée. Ces modèles sont généralement utilisés comme supports de communication ou dans des applications qui ne présentent pas de contrainte particulière en termes de précision géométrique.

Le contexte technologique actuel offre un large choix de gamme de capteurs légers notamment grâce aux progrès effectués dans le domaine de l'électronique et l'apparition des nano-technologies. Un appareil photo, un récepteur `GNSS`, un `LIDAR` et une centrale `IMU` sont des capteurs qui sont aujourd'hui couramment utilisés. À titre d'exemple, ces capteurs sont présents quasiment dans tous les téléphones portables grand public. Dans le domaine de la cartographie mobile, l'augmentation des performances des capteurs, offrant des résolutions de plus en plus grandes et des mesures de plus en plus précises, permet aujourd'hui (moyennant des protocoles rigoureux d'acquisition et d'étalonnage des instruments) de restituer avec une grande exactitude les trajectoires des plateformes mobiles ainsi que la géométrie 3D des scènes d'intérêt. Dans le cadre de notre travail, nous nous intéressons à l'utilisation de capteurs légers à des fins métrologiques. Par capteurs légers nous entendons des capteurs qui d'une part offrent un excellent rapport qualité/prix, d'autres part contribuent à réduire la charge utile du drone, ce qui permet, pour un vecteur identique, une autonomie de vol plus importante. Par ailleurs, d'un point de vue réglementaire les restrictions aériennes sont moins sévères pour les systèmes de masses faibles. Le Tableau 1.1 montre un panel de capteurs utilisés dans les applications de drones civils.

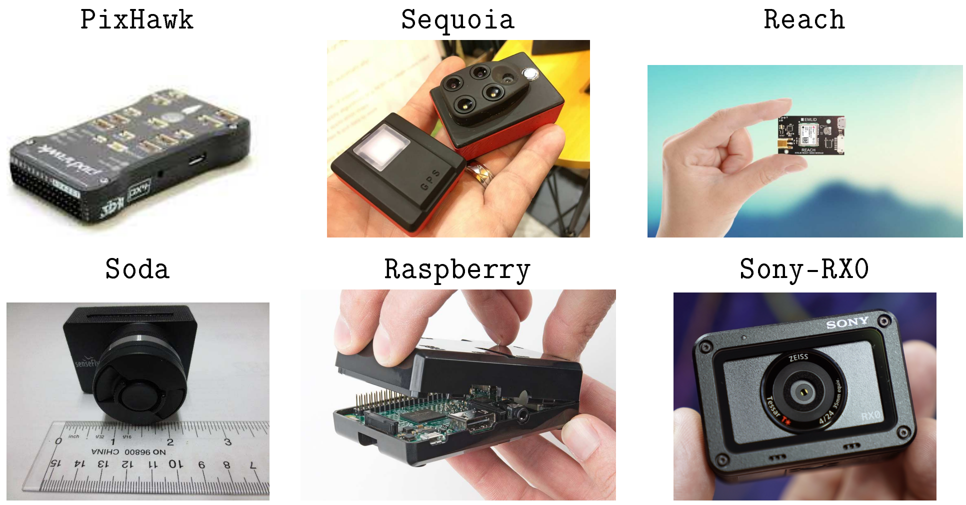

`PixHawk` `Sequoia` `Reach`

`Soda` `Raspberry` `Sony-RX0`

Tableau 1.1 : Panel de capteurs utilisés dans des applications de drones civils

L'émergence de solutions logicielles permettant de générer automatiquement un modèle 3D à partir d'images stéréoscopiques marque aujourd'hui

MICMAC	PIX4D MAPPER	PhotoScan 3D Modeling and Mapping Agisoft

Tableau 1.2 : Panel de quelques solutions logicielles photogrammétriques

une rupture considérable dans la "philosophie" de traitement de données photogrammétriques. Cette rupture est principalement due à l'apport considérable et la grande stabilité d'algorithmes de détection automatique de points d'intérêt entre images stéréoscopiques, à l'évolution des algorithmes d'estimation de pose, de calibration intrinsèque des caméras et de la mise en correspondance des images pour la reconstruction dense de la scène. Nous dénombrons pas moins d'une centaine de solutions logicielles photogrammétriques[1]. Ce progrès est accompagné d'une croissance soutenue de la puissance de calcul offerte par les processeurs et des capacités de mémoire et de stockage jamais égalées auparavant. Cela permet aujourd'hui de traiter des volumes de données considérables, en un temps record et avec un minimum d'interaction de l'opérateur.

Ce travail de recherche est un partenariat entre l'Institut national de l'information géographique et forestière (`IGN`) et `Vinci Construction Terrassement` un industriel du secteur des travaux publics. L'objectif est d'arriver à un système d'acquisition léger qui permet de restituer la géométrie des ouvrages avec une précision centimétrique et un travail topométrique réduit. Typiquement le système pourra comporter :

- un drone léger de type multi-rotors
- une caméra légère de qualité photogrammétrique
- un module `GPS`/`GNSS` bon marché
- une station `GNSS` de référence

La caméra et le récepteur `GPS` adoptés sont développés au laboratoire `LaSTIG` de l'`IGN`, au sein de l'équipe d'instrumentation `LOEMI`. La caméra, appelée

---

[1] https://en.wikipedia.org/wiki/Comparison_of_photogrammetry_software

`CamLight`, est un prototype de caméra aérienne ultra-légère qui présente les caractéristiques d'une caméra métrique. La caméra se base sur un capteur `CMOS` plein format haute résolution de 20M pixels équipé d'un "global shutter" pour éviter les effets indésirables du "rolling shutter" sur un vecteur mobile. Elle présente une cadence d'acquisition qui peut atteindre 10 images/seconde sans compression. La caméra embarque dans sa version la plus récente un module `GNSS` mono-fréquence et une antenne qui permet l'enregistrement des données brutes de phase. Ces données permettent de restituer une trajectoire précise en mode différentiel pour des courtes lignes de bases. L'aspect synchronisation temporelle des deux capteurs est parfaitement intégré dès la conception de la caméra et permet la réalisation d'une échelle de temps commune de manière précise et stable. Enfin, disposer de ce type d'instrument permet aussi l'accès à d'autres types de données non répandues dans les appareils du commerce. En l'occurrence, la `CamLight` fournit une mesure de température du capteur au moment de la prise de vue, ce qui permet d'étudier le phénomène de déformation thermique sur les images et qui fait l'objet du Chapitre 5.

Dans le but d'améliorer le processus d'acquisition des données sur ses chantiers, l'entreprise `Vinci Construction Terrassement` envisage dès 2012 l'utilisation de la photogrammétrie aérienne et terrestre comme outil de mesure. En effet, la photogrammétrie se présente comme une technique de modélisation 3D surfacique simple, pratique et facilement accessible à un public non expert. L'étape d'acquisition des données est de plus en plus automatisée. L'acquisition des images est très peu onéreuse, ce qui offre aussi la possibilité d'atteindre des niveaux de résolution et de densité considérables. La photogrammétrie présente aussi l'avantage de modéliser les scènes dans leur ensemble pour peu qu'elles soient texturées. Les produits photogrammétriques sont adaptés à différents types de problématiques présentes sur les chantiers de terrassement : estimation des volumes de stocks, blocométrie, auscultation des talus,... Néanmoins, la grande force de la photogrammétrie réside dans le fait que la précision géométrique offerte par cette technique peut être modulée de manière presque arbitraire. Cette valeur ne dépend que de la résolution spatiale des images, ce qui permet de l'utiliser aussi dans des configurations de métrologie fine, par exemple pour mesurer la déformation d'un ouvrage entre deux époques. L'utilisation d'un drone présente plusieurs avantages : la facilité d'emploi et de déploiement comparée à un vecteur aérien classique, un coût abordable, et pour un même capteur imageur, le drone offre une meilleure résolution spatiale. Il permet aussi un gain de temps lors de l'acquisition de données sur de grandes surfaces et contribue à la sécurité des employés sur le terrain grâce à sa capacité à survoler des zones inaccessibles ou d'inspecter des constructions complexes et difficiles d'accès.

Les besoins identifiés dans le contexte des travaux publics sont énumérés ci-après :

- utiliser les modèles 3D générés par photogrammétrie comme un support de mesure
- garantir une précision sub-décimétrique en fonction du type d'application
- géoréférencer l'acquisition avec un travail topométrique terrain réduit au strict minimum (une station `GNSS` de référence et, le cas échéant, un point d'appui)
- utiliser un système d'acquisition léger. Typiquement la masse idéale pour des raisons de sécurité et de réglementation est de ~2 kg
- utiliser des capteurs légers bon marché
- enfin, le système à développer devra être utilisable par un public non-expert

La problématique principale de notre travail de recherche est la mise en référence d'une acquisition photogrammétrique par `GPS` embarqué sur drone. Il existe différentes techniques de mise en référence ou de géoréférencement des acquisitions en photogrammétrie :

- le géoréférencement indirect
- le géoréférencement direct
- le géoréférencement assisté

Le géoréférencement indirect est la technique la plus largement utilisée en photogrammétrie aérienne pour des zones de petite échelle. Elle consiste à mesurer des points terrain appelés points d'appui dont les coordonnées servent à convertir l'orientation externe d'un système de coordonnées relatif arbitraire vers un système de coordonnées absolu. Les coordonnées des points d'appui sont généralement mesurées par des techniques de topométrie classiques (station totale, récepteur `GNSS` statique ou temps réel). Cette méthode de géoréfrencement est simple mais est inadaptée dans certain cas comme le relevé de zones de grande étendue (ou alors nécessite un nombre important de points) ou les zones inaccessibles. La mise en place des points d'appui exige un travail considérable sur le terrain dont le coût est non négligeable.

Le géoréférencement direct consiste à calculer directement, en temps réel ou en temps différé, la position et l'orientation des images grâce aux capteurs embarqués sur la plate-forme d'acquisition. Ces capteurs sont constitués à minima d'un récepteur `GNSS` et d'une centrale à inertie. Aujourd'hui les centrales inertielles de qualité présentent encore un coût élevé tandis que les systèmes bon marché permettent d'atteindre une précision de mise en référence plutôt décimétrique. De plus, dans la configuration du géoréférencement direct la masse des capteurs embarqués est inadaptée pour des plateformes de type drone et leur miniaturisation n'a pas encore atteint un degré de compatibilité acceptable. Aujourd'hui, cette technique de géoréférencement est principalement utilisée dans les relevés de cartographie à grande échelle ainsi que sur des chantiers de configuration linéaire (bande de vol unique par exemple).
Le géoréférencement assisté consiste en un couplage entre un récepteur `GNSS` et une caméra. Cette instrumentation est adaptée à des acquisitions photogrammétriques car il existe aujourd'hui des capteurs de qualité, bon marché et dont la masse est relativement faible. Nous présentons dans le cadre de ce travail de recherche un prototype dont la masse n'excède pas 2 kg, drone et capteurs compris. Ce système offre dans des conditions d'acquisition optimales une précision de mise en référence centimétrique. La combinaison des deux capteurs repose sur le principe que les erreurs d'estimation de trajectoires par photogrammétrie et par `GNSS` sont très différentes, ce qui permet en combinant correctement les deux techniques, de bénéficier des avantages de l'un et de l'autre. Les erreurs sur les positions d'une trajectoire `GNSS` sont plutôt décorrélées et de type bruit blanc tandis que les erreurs en photogrammétrie sont des erreurs relatives d'amplitude très faible mais dont la nature systématique donne par effet d'accumulation des grands biais potentiellement importants sur de grands blocs. Nous montrons que la fusion des données issues de ces capteurs permet d'atteindre des précisions en adéquation avec les tolérances types sur des chantiers de terrassement, à savoir, 1 à 5 cm, avec l'utilisation de 0 ou 1 point d'appui. Cette précision n'est toutefois atteignable qu'en modélisant de manière rigoureuse le couplage de ces capteurs. L'utilisation d'un point d'appui permet de s'affranchir des erreurs liées à de grands biais qui pourraient être le résultat d'une mauvaise calibration interne de la caméra ou du bras de levier. Le Tableau 1.3 donne une comparaison des différentes techniques de géoréférencement présentées selon 5 critères :

- la masse totale des capteurs à embarquer
- le temps de mise en œuvre sur le terrain

- l'étendue de la zone à relever
- le coût des capteurs et du vecteur d'acquisition
- l'exactitude atteignable pour chaque technique

	Géoréférencement		
	Indirect	Direct	Assisté
Masse	✓✗✗	✓✗✗	✓✓✗
Temps	✓✗✗	✓✓✓	✓✓✓
Échelle	✗✗✗	✓✓✓	✓✓✗
Coût	✓✓✗	✓✗✗	✓✓✗
Exactitude	✓✓✓	✓✓✗	✓✓✗

Tableau 1.3 : Comparaison des techniques de géoréférencement selon différents critères

La comparaison montre que pour répondre aux exigences de notre configuration (système léger, faible étendue et grande précision), le géoréférencement assisté se présente comme la technique de mise en référence la plus adaptée à nos besoins. Nous exposons dans ce qui suit l'importance du processus de calibration, notamment :

- calibration interne de la caméra
- calibration du bras de levier séparant le centre optique de la caméra et le centre de phase de l'antenne `GPS`
- calibration temporelle entre les capteurs, ce qui permet d'exprimer les mesures brutes dans la même échelle de temps

Nous montrons qu'il est possible d'atteindre une précision centimétrique pour la mise en référence de données photogrammétriques aéroportées sur drone. Le prototype se base sur des capteurs légers développés au sein du laboratoire de recherche. Cela nous permet d'avoir un contrôle fin sur les aspects de calibration. Nous proposons un modèle de calibration complet, qui consiste à mélanger un modèle radial de degrés élevés couplé à un modèle polynomial générique dans le but de modéliser les déformations résiduelles non prises en compte par les modèles physiques classiques. Nous proposons aussi une méthode d'estimation du bras de levier qui repose sur des mesures photogrammétriques et qui s'affranchit d'une contrainte mécanique pour le montage des capteurs sur le drone. Les résultats obtenus donnent une précision équivalente avec la méthode d'auto-calibration en vol qui nécessite de disposer de points d'appui. L'importance de la synchronisation temporelle est rappelée en exposant les résultats de tests de répétabilité montrant une instabilité pour un modèle de caméra commerciale. Différentes stratégies de fusion de données sont ensuite explorées. Des données d'évaluations montrent qu'une précision de 2 cm ± 0.5 cm est atteignable sans l'utilisation de points d'appui dans une configuration optimale.

La précision de localisation en photogrammétrie dépend de la qualité des différentes étapes de la chaîne de traitement globale : qualité de la détection et d'appariement des points de liaisons, orientation interne et externe et qualité de la mise en correspondance. Dans le cadre de notre travail, nous nous intéressons à améliorer la qualité de la localisation en optimisant la calibration interne de la caméra. En effet, il est établi que, à cause des variations de température, la caméra se déforme par dilatation thermique et qu'ainsi ses paramètres internes peuvent varier. Si cette déformation thermique est une fonction déterministe de la température, il est possible de la modéliser et donc de corriger cet effet lorsque l'on dispose de mesures de température. De plus, nous disposons d'une caméra de qualité photogrammétrique dont le modèle interne est stable dans des conditions de température identiques. Nous présentons une nouvelle méthode de calibration de l'effet thermique dans le but d'améliorer la précision de la reconstruction photogrammétrique. La méthode repose sur le calcul d'un champ de déformation pour des couples d'images de températures différentes. Le champ de déformation permet ensuite d'estimer un modèle analytique de correction de l'effet de température. Nous étudions l'influence sur les paramètres de focale et de point principal. Les résultats sont répétables et reproductibles pour le paramètre de focale moyennant deux expériences indépendantes, par relèvement dans l'espace. Des données d'évaluations terrestres et aériennes montrent un ratio d'amélioration d'un facteur 1,5. Une expérience de simulation de bande unique montre un ratio d'amélioration de 3,6 qui peut être interprété comme un facteur d'atténuation de l'effet de courbure de bande.

1.2 Organisation du document

Ce document aborde la problématique du géoéréférencement assisté par `GPS` dans le contexte d'une acquisition photogrammétrique par drone. Les problématiques étudiées se concentrent sur les aspects instrumentaux (calibration géométrique de la caméra et calibration spatio-temporelle entre la caméra et le récepteur `GPS`) et de fusion de données multi-capteurs. Dans un second temps, et dans le but d'améliorer la précision de localisation par photogrammétrie, une étude de l'influence de l'effet thermique sur les paramètres internes de la caméra est proposée.

Le Chapitre 2 est une introduction au contexte général de la thèse. Il présente les parties partenaires de ce travail de recherche, à savoir l'Institut national de l'information géographique et forestière (`IGN`) et `Vinci Construction Terrassement`. Une brève histoire des drones est exposée et quelques dates liées à l'évolution de l'utilisation des drones militaires et civils sont citées. La réglementation en vigueur en France est rappelée. L'importance et l'apport du drone civil et de la photogrammétrie dans le contexte des travaux publics sont soulignés. Les objectifs de ce travail de recherche ainsi que les contributions apportées tout au long de la thèse sont mentionnés à la fin de ce chapitre.

Le Chapitre 3 débute par un état de l'art des techniques de métrologie sans contact dans le domaine des sciences géographiques. Les techniques basées sur des mesures optiques ou des ondes électromagnétiques (station de topométrie, `GNSS` et `LIDAR`) sont brièvement présentées. La photogrammétrie, technique basée image retenue dans le cadre de notre travail, est présentée de manière détaillée. La chaîne de traitement globale est rappelée avec un état de l'art des méthodes de calibration interne et externe. En particulier une étude bibliographique est formulée pour l'étude de l'effet thermique sur les paramètres internes de la caméra. Les différentes techniques de géoréférencement sont présentées, en particulier le géoréférencmeent assisté par `GPS`.
Dans un second temps, la partie instrumentale et logicielle est proposée. Les spécificités techniques des principales solutions commerciales existantes ainsi que des instruments développés au sein du laboratoire d'accueil y sont exposées, en particulier la caméra photogrammétrique légère (`CamLight`) et le récepteur `GPS` (`GéoCube`) développés à l'`IGN`. Enfin, les solutions logicielles utilisées pour le traitement des données sont présentées.

Le Chapitre 4 s'intéresse à la problématique principale de notre travail de recherche, le géoréférencement assisté par `GPS` d'une acquisition photogrammétrique aérienne opérée par un drone. La chaîne de traitement globale est présentée avec les différents aspects de calibration à prendre en compte, à savoir : la calibration interne de la géométrie de la caméra, la calibration spatiale et temporelle entre la caméra et le `GPS`. Une méthode de détermination du bras de levier est proposée qui s'appuie uniquement sur des mesures photogrammétriques et est comparée à la méthode classique d'auto-calibration en vol. L'importance de la synchronisation temporelle entre les capteurs est rappelée et l'étude de la stabilité du retard électronique est exposée pour une caméra commerciale. Un critère de mise en correspondance des positions `GPS` et des centres de prises de vue est proposé. Différentes stratégies de fusion de données multi-capteurs sont ensuite présentées. Ensuite, les résultats de données expérimentales sont commentées et valident le choix des capteurs. Enfin, une conclusion ouvre la discussion sur la réduction du nombre de points d'appui.

Le Chapitre 5 propose une étude sur la déformation de la géométrie des images par effet thermique et sa modélisation en vue d'améliorer la précision des modèles photogrammétriques. Les aspects algorithmiques relatifs aux différentes expériences de calibration et d'évaluation sont présentés : calcul d'un champs de déformation par mise en correspondance 2D, modèle adopté pour corriger l'effet de température, mise en évidence de l'impact de la température sur les paramètres internes par relèvement dans l'espace et, enfin, description de la chaîne de traitement globale pour évaluer le gain en précision. Différentes expériences d'évaluation sont proposées : acquisition terrestre, simulation de l'effet de courbure de bande sur une acquisition terrestre et, enfin, une acquisition aérienne par drone dans une configuration de type corridor.

Le Chapitre 6 donne les conclusions générales de ce travail de recherche. Il étudie plus particulièrement l'amélioration de la méthode de calibration du bras de levier basée sur une modélisation 3D du drone. Pour la chaîne de géoréférencement assisté par `GPS`, des perspectives d'améliorations de la précision et la robustesse sont proposées. Enfin, pour la modélisation de l'effet thermique, une étude sur la stabilité long terme reste à mener.

CHAPTER 2

Introduction

Contents

2.1 Context 12
2.1.1 National Institute of Geographic and Forestry Information 13
2.1.2 Vinci Construction Terrassement 14
2.1.3 SIXENSE Mapping 15
2.2 UAVs systems & Regulation 16
2.2.1 A brief history of drones 16
2.2.2 Civilian drones today 18
2.2.3 Regulation in France 21
2.3 Needs & Challenges 21
2.3.1 Needs in the context of Public Works 21
2.3.2 Aims & Objectives 23
2.4 Organization of the thesis 26
2.5 Contributions of the thesis 28

2.1 Context

The context of this work lies at the crossroads of different fields in full revolution in recent years. The development of applications related to the use of civilian drones is now undergoing a spectacular evolution. Aerial photography is positioning itself as a leading application and `UAV`/`UAS` photogrammetry is making a huge profit from this revolution and is nowadays a technology that is increasingly accessible to the great public. Moreover, `SFM` algorithms now allow to generate visually perfect 3D dense reconstructions of the captured scenes in a quasi-automatic way. The performance in terms of computing power of today's machines also saves considerable time and open doors to unprecedented levels of resolutions.

On the other hand, the miniaturization of electronic components now makes it possible to embark different sensors with a minimum of payload and thus several sources of measurements enabling multi-sensor data fusion to achieve accurate results with very light weights. Digital cameras, `LIDAR`, `GNSS` modules as well as `IMUs` are part of these sensors today widely integrated whether it is in drones, mobile mapping vehicles or, more generally, everyday connected objects like smart-phones. It is possible nowadays to carry out aerial photogrammetric acquisitions for topometric purpose or for metrological need, not exceeding a weight of 2 kg, drone and sensors included.

However, the performance of light modeling methods does not meet the requirements of users when the calculated 3D models serve as a geometric measurement support, such as accurately measuring the absolute position of an infrastructure or establishing a precise topometric plane. However, today there is a strong demand from different users for light airborne acquisition systems capable of providing 3D modeling with centimeter absolute accuracy. This work is a research project in partnership between a public and a private company - `IGN` and `Vinci Construction Terrassement`. The purpose is to develop a system that enables to restore the geometry of structures with centimeter accuracy and minimal topometric work on the ground from images acquired using a light drone. Typically, the system to be developed may include:

- a light multi-rotor drone,
- a light photogrammetric camera,
- a `GNSS` module on the drone,
- a `GNSS` reference station

2.1.1 National Institute of Geographic and Forestry Information

The National Institute of Geographic and Forestry Information (`IGN`) is a public administrative institution the mission of which is to ensure the production, maintenance and dissemination of geographical reference information in France. This institute was founded on June 26, 1940, following the dissolution of the `SGA`, founded in 1887.

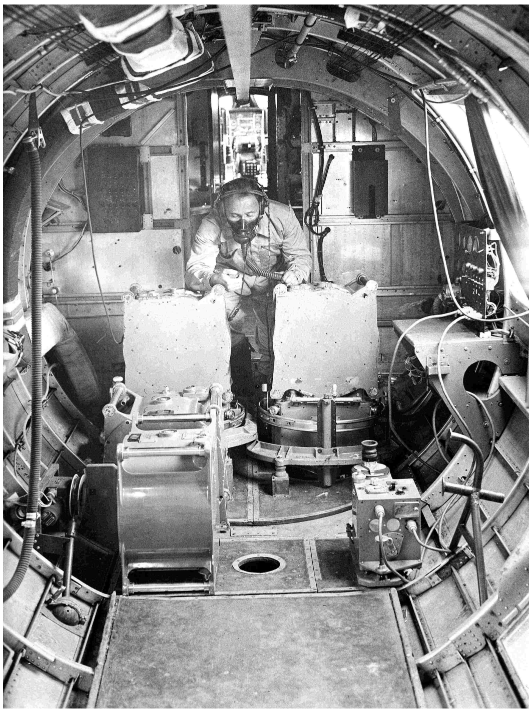

Figure 2.1: Aerial acquisition on a `B17` in 1947 ; source: `www.ign.fr`

The institute is now divided into 6 departments among them, the Research and Education Department, which includes the `ENSG` as well as the `LaSTIG`. This laboratory comprises several research teams: `COGIT`, `LAREG`, `LOEMI` and `MATIS`. The current research work was carried out within the `LOEMI` team.

The `LOEMI` is the instrumentation team of `IGN`'s `LaSTIG` laboratory. It is located in Saint-Mandé, near Paris. `LOEMI` was incorporated into the `IGN` research department in 1988. It is currently headed by Ch. Thom. The laboratory develops specific instruments to meet `IGN`'s needs both for its production and research topics. The team's skills range from mechanical, optical and electronic design to software developments. The activities of the laboratory mainly focus on two axes: the development of new sensors and the improvement of data processing algorithms. Examples of research and development carried out by the team include:

- development of aerial digital cameras used for IGN production acquisitions,
- development of stabilized platforms, used to support cameras in an aircraft,
- development of a system of measurements, monitoring and warning of areas with high risks of ground movement (the GéoCube),
- development of a lightweight camera for UAV and indoor photogrammetry

Figure 2.2: CamV2 (left), GéoCube (center) and CamLight (right) ; source: http://loemi.recherche.ign.fr/

2.1.2 Vinci Construction Terrassement

Vinci Construction Terrassement is a company belonging to the Vinci group and specializing in the implementation of large infrastructures and more generally, facilities of which the earthwork is an essential component. The company was created by the fusion of GTM Terrassement and Entreprise Deschiron on December 19, 2008. The company is widely established in France with a dozen agencies spread over the entire territory. Some notable achievements of the company are:

- the 302 km SEA high-speed line linking Tours to Bordeaux, including the construction of 400 structures,

- `Regina ByPASS` a 66 km motorway length in Canada,
- the `A19`, a 101 km long motorway in France

Figure 2.3: Aerial view of part of a stretch of the `SEA` line; source: `Vinci Construction Terrassement`

The company has a technical department that combines several skills: a design office for the upstream part of the projects, a geotechnical laboratory for the study of soils and a topometry service for the metrological monitoring aspects of its own worksites. This work was carried out in collaboration with the topometric center where photogrammetry was introduced in the early 2010s, notably through the development of an airborne system on `ULM` for monitoring the `SEA` construction site using `LIDAR` and photogrammetry. Since 2013 the topometric department has been using terrestrial and `UAV` photogrammetry. In 2017 the `LIDAR` and photogrammetry team gave birth to a new company called `SIXENSE Mapping`.

2.1.3 SIXENSE Mapping

`SIXENSE Mapping` is a young innovative company in the field of 2D/3D digitization of civil engineering structures. It is part of the `SIXENSE Group`, an entity that registers experts within the `Vinci Group`. This group was set up in 2017 to design, build and operate infrastructures better. It employs

600 people and regroup 10 companies in the fields of soil, structures, and the environment.

The major activity of `SIXENSE Mapping` is the large-scale helicopter and small and medium-scale drone surveys. With its internal resources the company implements the whole chain of data acquisition through the processing until delivery of the final products to customers. One area in full expansion is the very high resolution digitization of structures (0.1-0.5 mm `GSD`). The aim is to map all the defects presented on a work on a given date in order to visualize and understand the deformation of the structure as a whole better, but also to monitor the evolution of all defects over time.

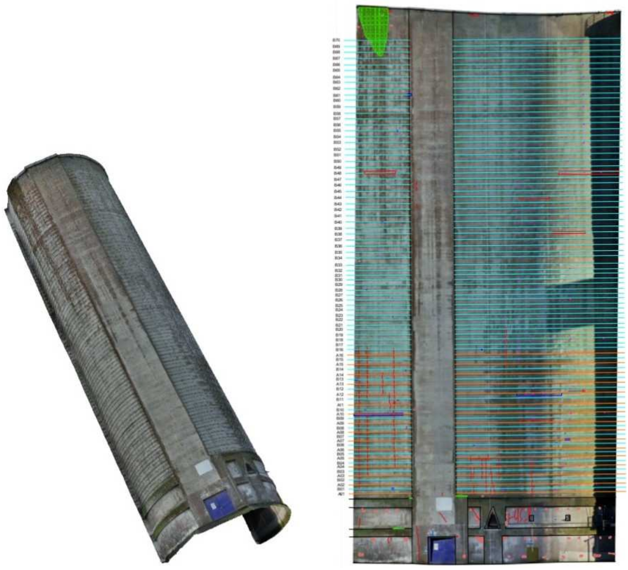

Figure 2.4: Example of a silo 3D model and mapping of orthoimage disorders; source: `SIXENSE Mapping`

2.2 UAVs systems & Regulation

2.2.1 A brief history of drones

We generally define a drone as an unmanned aircraft by the word drone. There are different types of drones: assisted drones that require constant contact with a remote pilot to fully autonomous drones that require almost no human intervention. The history of drones goes back to the early 20^{th} century with the desire to develop unmanned aircraft, for military purposes mainly. In 1916, in England, the project Aerial-Target was launched by Prof. Archibald Low[1]. The purpose of the project was to develop a small radio-controlled unmanned aircraft to drop bombs on targets without risking casualties. Several flight trials were carried out but resulted in failures. In 1917, in the United States, the Hewitt-Sperry Automatic Airplane project was led by Elmer Sperry[2] and Peter Cooper Hewitt[3]. The goal was equivalent to the project carried out in England. However E. Sperry understood that not only did the difficulty of controlling a remote aircraft reside in radio equipment, but for better operation, the aircraft had to be stabilized. In that regard, he tried to perfect the gyroscopes developed for the naval sector and transpose them to aircraft. For example these experiments allowed to drop a load from a distance of 48 km with an accuracy of 3 km. In France, Max Boucher[4] achieved the first drone flight on April 17, 1923, as part of an "automatic aircraft" experiment. Captain M. Boucher resumed the work of Détable Octave[5] on the stabilization of planes with the design of divergent conical wings. He equipped his aircraft with Sperry's gyroscopic stabilization system and enhanced the automation of the flight with a barometer and a stopwatch. His research was called off in 1924 for lack of funds.

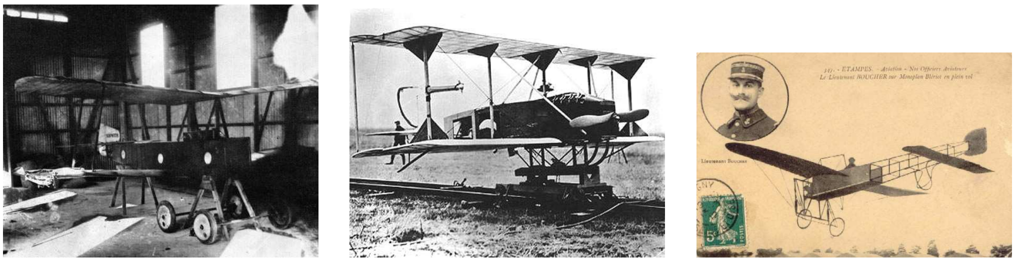

Figure 2.5: Aerial Target in 1920 (left) source: http://www.ctie.monash.edu/, Hewitt-Sperry Automatic Airplane in 1918 (center) source: https://en.wikipedia.org/wiki/Hewitt-Sperry_Automatic_Airplane and Max Boucher in 1912 (right) source: http://www.corpusetampois.com/

The evolution of the drones achieved a great development follow-up in the following decades always under a military impulse. This is the beginning of the democratization of the drones destined to the army. Not only were drones used

---

[1] 1888-1956

[2] 1860-1930

[3] 1861-1921

[4] 1879-1929

[5] X-X

only in times of war but now they were also used for remote surveillance missions. The improvement of these devices was permanent with a reduction in weight, size, and an increased onboard capacity and greater discretion. In the early 2000s the drone made its entry into the civilian field. In order to adapt these machines to the needs of professionals and the great public, the efforts of miniaturization and simplification are supported. The number of civilian drone makers increased and the number of drones operators skyrocketed as systems became more and more accessible. In fact, civilian drones could be found in a many industrial applications. Its first mission was to acquire data in a fast and simple way, where a human operator would spend considerable time in a repetitive task. Therefore the drone represented a major economic challenge for the industry. The civilian sectors in which the drone is used are varied, for instance: agriculture, construction, public works, infrastructure inspection, archeology, architecture, heritage preservation, forestry. Figure 2.6 shows a panel of some of these fields.

Figure 2.6: 3D model of an air cooler (left, source: `SIXENSE Mapping`), 3D model of Chambord castle (center, source: `ENSG`) and canopy model (right, source: [Lisein 2016])

2.2.2 Civilian drones today

To date, civilian drones have undergone a great evolution since early 2010. They have benefited from the technological and mass-media impact so much that both the great public and professionals have been enjoying using them. Nowadays the market for civilian drones has been constantly increasing. Their use is more and more supervised by aerial traffic rules and flying becomes more and more simplified and accessible. This particularly contributes to their development and democratization.

Civilian drones can be divided into two main categories. Recreational drones for the great public and (semi)professional drones intended for a profit-making activity. The field of application generally requires a specific type of drone more adapted to the activity. Civilian drones consists of two main categories: multi-rotor drones and fixed-wing drones. Each category has its pros and cons. Table 2.1 classifies these two categories according to their performance.

	Fixed-Wings	Multi-Rotor
Autonomy	✓✓✓	✓✗✗
Range	✓✓✓	✓✗✗
Weather Sensitivity	✓✗✗	✓✓✗
Takeoff/Landing	✓✗✗	✓✓✓
Speed	✓✓✓	✓✓✗
Payload	✓✓✗	✓✓✓

Table 2.1: Comparison between the two categories of drones according to six performance criteria ; source: [Eisenbeiß 2009]

Depending on the user's need, it is more convenient to use a multi-rotor drone, for example for very high spatial resolution imagery or for take-off terrain constraints where a vertical take-off is less challenging. For large area surveys, the use of a fixed-wing drone with a high autonomy is the most effective solution. In general, in the public works sector, the use of a multi-rotor drone is more common because it is easier to operate. For stock volumes, quarrying or infrastructure inspection, the multi-rotor drone offers the required advantages needed for this kind of acquisitions. The low payload of a fixed-wing drone is a drawback for long distance surveys in public works. Therefore, `ULMs` are more adapted.

There is nowadays a significant number of `UAVs` manufacturers; some produce recreational and semi-professional drones whereas others made the choice to specialize in professional drones for companies. Figure 2.7 shows the distribution of `UAVs` manufacturing according to the drones models registered within `UAS` authorities, whereas Figure 2.8 shows a panel of existing business solutions used widely today.

Another indicator of the trend on the market for civilian drones is the number of operators of drones registered[6]. As of July 14, 2017, France had no fewer than 7922 organizations owning and operating drones whereas on 15 January 2013 only 127 operators were registered. Development forecast remain consid-

---

[6] source: `www.federation-drone.org`

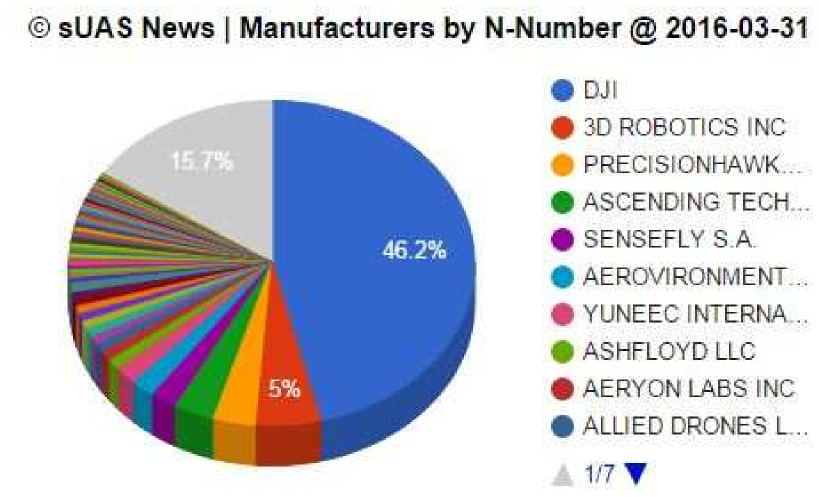

Figure 2.7: Market share of civilian drone manufacturers registered in the `USA` ; source: `http://carnets-davenir.com`

Figure 2.8: Panorama of `UAV` models widely used today ; source: manufacturers' respective websites

erable. Today, the majority of `UAV` operators work in the audiovisual sector. Areas such as surveillance, energy, inspection still have a small but constantly growing market share.

2.2.3 Regulation in France

The acquisition of airborne data by drone is a regulated activity in more and more countries, particularly in developed countries. National mapping agencies, in European countries for example, quickly understood the value of using drones and participating in innovative projects, or even using them in their internal production process [Cramer *et al.* 2013]. Moreover, in Europe, regulation at European level will be launched by 2018 in order to harmonize the existing legislation in the different European countries. In France, the use of civilian drones has been regulated by law since 2012 with the publication of two ministerial decrees which define the design of drones, their usage, the skills of people using them, and the integration of these aircrafts into airspace. This legislation rapidly evolved with the publication of a second decree on December 17, 2015, as amended by the decree of March 30, 2017. The successive and recent evolutions of law give an indication of the dynamism in this business line in full expansion as well as the support of the authorities to supervise the activity better, with a focus on safety aspects.

France, allows the movements of drones in its airspace within the framework of specific scenarios as summarized in Figure 2.9. The main criteria are relative to the flight height of the `UAV` which can never exceed 150 m, the weight of the drone must not exceed 25 kg and in certain scenarios, as in scenario S4, the mass is limited to 2 kg (if the mass of the drone is lower than 2 kg, the use of a parachute is not mandatory for urban scenario S3). The distance to the remote pilot is also a relatively restrictive criterion except in scenario S4 where this distance is unlimited.

French drone regulation also specifies areas where airspace is subject to specific rules, such as airports, nuclear power stations or military zones. Figure 2.10 shows the distribution of these restricted areas.

2.3 Needs & Challenges

2.3.1 Needs in the context of Public Works

Lightweight mapping is now a major issue because, with cheap sensors, we can achieve a level of accuracy that meets the needs of a number of applications. In fact, it is possible to produce metric 3D models using commercial cameras as long as a few precautions are taken into account during data acquisition (for example: use of a fixed focal length, constant acquisition parameters or even a calibration acquisition on a topometric

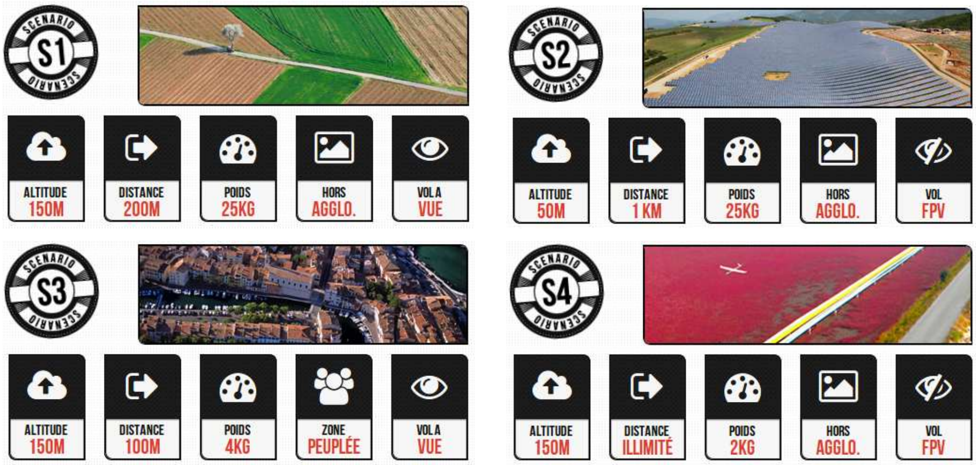

Figure 2.9: Scenarios of flights of drones in France ; source: http://www.drones-lab.com

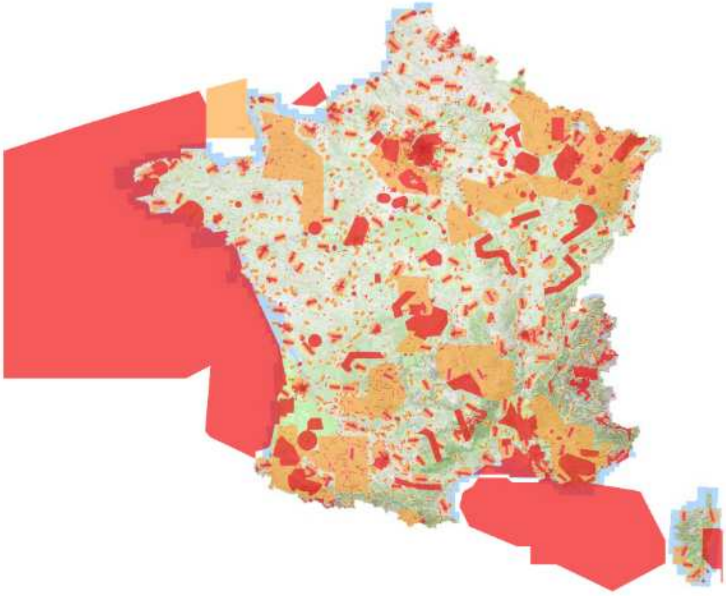

Figure 2.10: Map of `UAV` flight areas with restrictions in France ; source: www.geoportail.gouv.fr

polygon before acquisition in order to freeze the internal camera model during the photogrammetric processing). For companies like `Vinci Construction Terrassement` and `SIXENSE Mapping` the contribution of `UAV` photogrammetry is considerable: first of all the drone is a tool that saves time for acquiring data. A surveyor will be able to carry out a survey up to several tens of hectares per hour. For volume survey, quarries and stocks, `UAV` photogrammetry makes it possible to restore the volume quickly and more accurately, which offers a better monitoring of the variation of volumes and thus a better estimate of expenses (improved management of trucks flows and better predictions on material orders). The drone is also an efficient tool to carry out inventories before the start of a construction site and also during the works. Finally, it also contributes to the safety of employees with the ability to fly over inaccessible areas or to inspect complex buildings with difficult access like power lines. Figure 2.11 shows an example of the new stock volume survey using a `UAV` at `Vinci Construction Terrassement`.

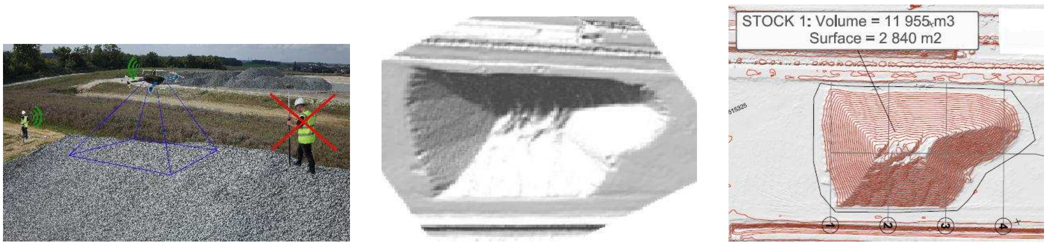

Figure 2.11: Systematic use of the drone for the calculation of a stock volume of material ; source: `Vinci Construction Terrassement`

In the context of public works, the need for data acquisition must meet a number of requirements for the intended applications. For example, for volumetric or blocommetric applications, a high relative precision of the 3D model is required. In theory, these kind of acquisitions require scaling only and georeferencing in a legal coordinate system is not always necessary. In the case of an inventory or surveys to follow the evolution of a construction site, georeferencing in a legal coordinate system is required. The absolute accuracy of the georeferencing may vary from a few decimeters to a few centimeters. Finally, we can identify a third type of applications where a high absolute accuracy of localization is required, centimetric generally, for example in case of the construction of highways, high-speed train lines or monitoring of areas with risk of landslides.

2.3.2 Aims & Objectives

In order to improve the conditions of data acquisition on the field of earthworks, `Vinci Construction Terrassement` - aware of the potential and contribution of photogrammetry on its sites - and `IGN` decided, through a `CIFRE` convention, to study the possibility of restoring the geometry of structures with high localization accuracy. The objective of this work is to set up an aerial photogrammetric acquisition system that allows the production of high-quality data. The `UAV` should be equipped at least with a `GNSS`/`GPS` receiver and a metric camera. In addition, the topometric work on the ground should be kept to a minimum in order to increase productivity (for example: only the installation of a static `GNSS` base station used for processing the trajectory of the `UAV` in differential mode and 1 or 2 `GCPs` depending on the geometry of acquisition). The system will have to carry inexpensive sensors with a mass below 2 kg, drone and payload included.

The aim of this partnership is also to democratize the use of photogrammetry among the `Vinci Construction Terrassement` survey teams (approximately one hundred people) who mainly use total station type instruments and conventional `GNSS` receivers to achieve topographic surveys. These instruments are sometimes unsuitable for acquisitions of large areas or where a high resolution or density of information is necessary. The first photogrammetric acquisitions began on `Vinci Construction Terrassement` sites in 2013 with acquisitions of basins in terrestrial configuration. The first drone experiments were carried out in early 2014. The vectors used at that time consisted of a `DJI-F550` and a `DJI Phantom 1`, which carried a `RICOH-GR` compact camera. By 2015, the `Pixhawk` flight controller ([Meier *et al.* 2011],[Meier *et al.* 2012]) was adopted. The `Pixhawk` is an automatic flight management equipment developed by a community of volunteers (the open-hardware `PX4` project) in collaboration with `3D Robotics`, a manufacturer of drones. The `Pixhawk` embedded system called `ArduPilot` comes in several versions: `ArduCopter` for rotating wing drones, `ArduPlane` for fixed wing drones and `ArduRover` for ground drones. These firmwares are free and open-source. It gives the drone an autonomous and stable navigation thanks to the onboard instruments (`GPS` receiver, accelerometers, gyrometers, magnetometers, barometer, compass, as shown in Figure 2.12). The aim is to keep the same flight controller on different types of drones. Besides, this controller provides configuration possibilities such as synchronization of the camera with the controller to manage image triggering automatically.

For the flight management station, the `Mission Planner` software is chosen. `Mission Planner` is a free and open-source software designed to serve as a ground control station. This software is a tool to configure `Pixhawk` equipped drones. It acts as an interface to the hardware and embedded system. It offers the possibility to plan missions and the real-time transmission of telemetry data of the drone. A modified interface has been developed within the com-

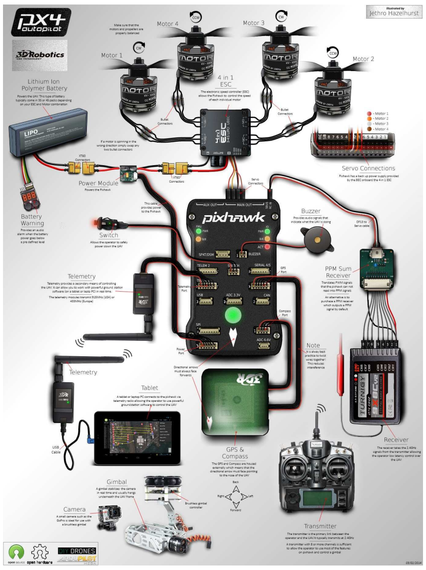

Figure 2.12: Different sensors used with the `Pixhawk` flight controller ; source: `www.escadrone.com`

pany in order to restrict the interaction to only useful parameters and to make it easier to use. Finally `MicMac` photogrammetric suite is used to process acquired images. A graphical interface has also been developed internally to make processing accessible to a majority of employees. Figure 2.13 shows the interfaces developed and used internally.

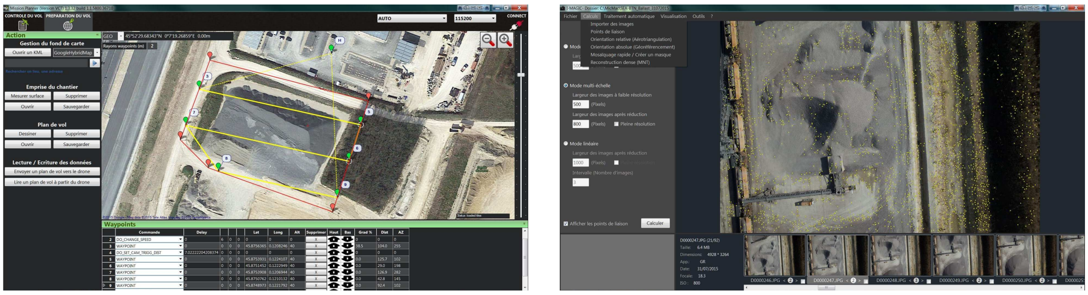

Figure 2.13: Modified `Mission Planner` interface (left) and `MicMac` interface (right) ; source: `Vinci Construction Terrassement`

Since 2015 the `IRIS`/`IRIS+ 3D Robotics UAV` model is adopted (Figure 2.14 left). It offers a maximum autonomy of about 15 min for a total mass of battery and camera less than 2 kg. It is a drone simple to use, practical and with a wind resistance up to 30 km/h. It is delivered `RTF` and costs about $600.

`3D Robotics` has now stopped the production of this model. Today, 5 drones are still in production although they have performed dozens of missions and several hours of flight, it shows the robustness and reliability of these entry-level open-hardware and open-source machines. In 2017, the company trained 10 `UAV` remote pilots located in different agencies on the French territory. The drone selected to equip these agencies is the `DJI-Phantom 4 Pro` model. The choice of this drone is mainly due to the fact that for the first iteration of externalization of `UAV` acquisitions, carried far by the central technical survey service of the company, to local agencies, the choice of an easy to use `UAV`, inexpensive and of high reliability (detection of obstacles in 5 directions, long range control up to 7 km and a large autonomy of flight 30 mins) was adopted. In addition, this drone has a built-in camera with 1" `CMOS` sensor of 20 MPx resolution with a `Global Shutter` (Figure 2.14 right).

Figure 2.14: `IRIS+` `UAV` model manufactured by `3D Robotics` (left ; source: `Vinci Construction Terrassement`) and `DJI-Phantom 4 Pro` (right ; source: `www.dji.com`)

In 2017, the `R'Scan` team from `Vinci Construction Terrassement`, responsible for the acquisition of photogrammetric and `LIDAR` data using `UAV` and `ULM` became an independent operator, `SIXENSE Mapping` 2.1.3, part of the `SIXENSE group`. This company now has 7 drones: `IRIS`/`IRIS+`, `DJI-Phantom 2` and `DJI-Phantom 4 Pro` and the `DroneStar 850 V2` manufactured by `InnovaDrone` which is a `Pixhawk` flight controller based `UAV` and which embedded sensors adapted to integrated sensor orientation processing with aerial position control.

2.4 Organization of the thesis

This thesis addresses the problem of integrated sensor orientation in the context of a `UAV` photogrammetric acquisition. The issues studied focus on the instrumental aspects (internal orientation of the camera and spatial/temporal calibration between the camera and the `GPS` receiver) and multi-sensor data fusion strategies. In a second step, and in order to improve the accuracy of photogrammetric localization, a study of the influence of the thermal effect on the internal parameters of the camera is proposed.

The Chapter 2 is an introduction to the general context of the thesis. It presents the partner parties of this research work, National institute of geographic and forest information (`IGN` the french mapping agency) and `Vinci Construction Terrassement`. A brief history of drones is exposed and some dates related to the evolution of the use of military and civilian drones are cited. A summary of the french `UAVs` aerial regulations is given. The importance and the contribution of the civilian drones and photogrammetry in the context of public works are underlined. The objectives of this research work as well as the contributions made throughout the thesis are mentioned at the end of this chapter.

The Chapter 3 begins with a review of contactless metrology techniques in the field of geographic sciences. Techniques based on optical measurements or electromagnetic waves (topometry station, `GNSS` and `LIDAR`) are briefly presented. Photogrammetry, an image-based technique used in our work, is presented in details. The global processing workflow is recalled with a state-of-the-art internal and external calibration methods. In particular a bibliographic study is formulated for the study of the thermal effect on internal parameters of the camera. The different georeferencing techniques are presented, in particular integrated sensor orientation.
In a second step, the instrumental and software part is proposed. The technical specificities of the main existing commercial solutions as well as the instruments developed within the laboratory are exposed, in particular the light photogrammetric camera (`CamLight`) and the `GPS` receiver (`GéoCube`) developed at `IGN`. Finally, the software solutions used for data processing are presented.

The Chapter 4 focuses on the main issue of our research work, integrated sensor orientation of a `UAV` photogrammetric acquisition using a `GPS` receiver. The global processing workflow is presented with different aspects of calibration to be taken into account: internal orientation of the camera, the spatial and temporal calibration between the camera and the `GPS`. A lever-arm estimation method is proposed which relies only on photogrammetric measurements and is compared to the traditional in-flight self-calibration method. The importance of the temporal synchronization between the sensors is recalled and the study of the stability of the electronic delay is exposed for a commercial camera. A criterion for matching `GPS` positions to camera centers is proposed. Different multi-sensor data fusion strategies are presented. Then, the results of experimental data are commented and validate the choice of sensors. Finally, a conclusion opens the discussion on the reduction of the number of ground control points.

The Chapter 5 proposes a study on the deformation of the geometry of images by thermal effect and its modeling in order to improve the accuracy of photogrammetric models. The algorithmic aspects relating to the various calibration and evaluation experiments are presented: computation of a deformation field by 2D matching, adopted model to correct the temperature effect, highlighting the impact of temperature on the internal parameters by space resection technique and finally, description of the global processing workflow to evaluate the improvement of accuracy. Various evaluation experiments are proposed: terrestrial acquisition, simulation of bowl effect on a terrestrial single strip acquisition and, lastly, an airborne acquisition in a corridor configuration.

The Chapter 6 gives the general conclusions of this research work. We discuss in particular the improvement of the lever-arm calibration method based on 3D modeling of the `UAV` with mounted sensors. For the integrated sensor orientation workflow, prospects for improvements in accuracy and robustness are proposed. Finally, for the modeling of the thermal effect, a study on the long-term stability remains to be carried out.

2.5 Contributions of the thesis

Publications of the author:

- International journals:
  - [Daakir et al. 2017] M. Daakir, Y. Zhou, M. Pierrot-Deseilligny, C. Thom, O. Martin. Improvement of photogrammetric accuracy by modeling and correcting the thermal deformation on images. (submitted to ISPRS Journal of Photogrammetry and Remote Sensing on January 22, 2018).
  - [Daakir et al. 2017] M. Daakir, M. Pierrot-Deseilligny, P. Bosser, F. Pichard, C. Thom, Y. Rabot and O. Martin. Lightweight UAV with on-board photogrammetry and single-frequency GPS positioning for metrology applications . ISPRS Journal of Photogrammetry

  and Remote Sensing, vol. 127, pages 115-126, 2017. Geospatial Week 2015.
  - [Rupnik et al. 2017] Ewelina Rupnik, Mehdi Daakir and Marc Pierrot Deseilligny. MicMac - a free, open-source solution for photogrammetry. Open Geospatial Data, Software and Standards, vol. 2, no. 1, page 14, 2017.

- International conferences with act:
  - [Daakir et al. 2016] M. Daakir, M. Pierrot-Deseilligny, P. Bosser, F. Pichard, C. Thom and Y. Rabot. Study of lever-arm effect using embedded photogrammetry and on-board GPS receiver on UAV for metrological mapping purpose and proposal of a free ground measurements calibration procedure. ISPRS - International Archives of the Photogrammetry, Remote Sensing and Spatial Information Sciences, vol. XL-3/W4, pages 65-70, 2016.
  - [Daakir et al. 2015] M. Daakir, M. Pierrot-Deseilligny, P. Bosser, F. Pichard and C. Thom. UAV onboard photogrammetry and GPS positionning for earthworks. ISPRS - International Archives of the Photogrammetry, Remote Sensing and Spatial Information Sciences, vol. XL-3/W3, pages 293-298, 2015.

- National conferences with an act (poster):
  - [Daakir et al. 2016] M. Daakir, N. Gaucher, Y. Rabot, E, Elaudais, F. Pichard, M. Pierrot-Deseilligny. L'open-source au service des Travaux Publics. Colloque SFPT Photogrammétrie Numérique et Perception 3D, Marne-la-Vallée, 15-17 mars 2016.
  - [Daakir et al. 2014] M. Daakir, F. Pichard, E. Elaudais, N. Gaucher, M. Pierrot-Deseilligny, P. Bosser, C. Thom. Colloque scientifique francophone Drones et moyens légers aéroportés d'observation : recherche, développement, applications : l'état de l'art. Localisation absolue centimétrique par photogrammétrie aéroportée et GPS embarqués sur drone, application au terrassement, Montpellier, 24-26 juin 2014.

- International conferences without an act:
  - [Daakir et al. 2017] M. Daakir, Y. Zhou, J-P. Souchon, J-M. Muller, G. Nguyen, M. Pierrot-Deseilligny, C. Thom, O. Martin. IGN photogrammetric camera for UAVs: concept and results. DGPF Meeting 2017 : UAV Metric Camera session, Würzburg, 8-10 mars 2017

- National conferences without an act:
    - [Daakir et al. 2017] M. Daakir, M. Pierrot-Deseilligny, P. Bosser, Y. Rabot, C. Thom. Couplage GPS et caméra embarqués sur drone pour de la modélisation photogrammétrique industrielle. 26$^{\text{èmes}}$ Journées de la Recherche de l'IGN, Marne-la-Vallée, 23-24 mars 2017.
    - [Daakir et al. 2015] M. Daakir, M. Pierrot-Deseilligny, P. Bosser, C. Thom, F. Pichard. Photogrammétrie aéroportée et positionnement précis par GPS embarqué sur drone : application au terrassement. Journées scientifiques : Photogrammétrie et imagerie 3D, Cerema Rouen, 3-4 juin 2015.
    - [Daakir et al. 2015] M. Daakir, M. Pierrot-Deseilligny, F. Pichard, P. Bosser, C. Thom, O. Martin, Y. Rabot, N; Gaucher. Photogrammétrie aéroportée par drone et positionnement GPS embarqué : application au terrassement. 24$^{\text{es}}$ Journées de la Recherche de l'IGN, Marne-la-Vallée, 19-20 mars 2015.

Participation in academic and scientific life:

- Supervision of internships:
    - Sahar Gaaloul, ENSG-PPMD student: project on the registration of trajectories by photogrammetry and GPS in the case of a one degree of freedom time synchronization.
    - Sébastien Patte, IUT-Chartres student: training on the development of a system allowing the recording of data of a double-frequency GNSS receiver and the synchronization of measurements with a camera. Internship co-supervised with Olivier Martin.
    - Guillaume Hérault and Benjamin Grigoroff, ENSG University Degree students: project on the study of the impact of the variation of the auto-focus and temperature on the internal parameters of a camera.
    - Benjamin Grigoroff, ENSG University Degree student: internship on the development of a pole for terrestrial acquisitions by photogrammetry and geo-referencing assisted by double-frequency GNSS receiver.
    - Terry Moreau and Cécile Petit, 2$^{\text{nd}}$ year ENSG Engineer students: project on the implementation of a supercomputer based on RASPBERRY-PI for the acceleration of photogrammetric data processing. Project co-supervised with Truong Giang Nguyen.

  - Julien Franche, ENSG University Degree student: internship on the development of a 2D/3D visualization tool for cracks visualization on engineering structures.

- Open-source software diffusion:
  - Tutorial at the SFPT 2017 symposium: "Photogrammétrie et télédétection : vers la convergence ?".
  - Tutorial at the SFPT 2016 symposium: ""Photogrammétrie Numérique et Perception 3 D : les Nouvelles Conquêtes".
  - Tutorial at the Foss4G-fr (2016) (co-hosted by Ewelina Rupnik)

- Reviewer :
  - Reviewer for ISPRS Journal of Photogrammetry and Remote Sensing.
  - Reviewer for Guillaume Koehl engineer internship: "Cadastration de piscines par technique photogrammétrique".
  - Reviewer for Gauthier Duponchel engineer internship: "Géoréférencement d'un nuage de points issu d'une caméra stéréoscopique portée par un drone".

Employed work:

- Obtaining of the ULM theoretical diploma and declaration of skill level (drone remote pilot license)

- Performing several UAV photogrammetric acquisitions in a production context

- Participation in the processing of photogrammetric data in a production context

- Participation in meetings, feasibility studies, writing of technical notes (answers to calls for tenders), etc.

- Transfer of skills within the company

Chapter 3

Literature Review, Hardware & Software

Contents

3.1 Introduction 34

3.2 Contactless Metrology Techniques 34

- 3.2.1 Topometric Instruments 35
- 3.2.2 GNSS 36
- 3.2.3 LIDAR 38
- 3.2.4 Photogrammetry 39
  - 3.2.4.1 Interior Orientation 41
  - 3.2.4.2 Thermal Deformation 42
  - 3.2.4.3 Exterior Orientation 44
  - 3.2.4.4 Georeferencing Techniques 46

3.3 Hardware 48

- 3.3.1 Off-the-shelf Solutions 49
- 3.3.2 IGN lightweigth metric camera 50
- 3.3.3 IGN GeoCube 53
- 3.3.4 UAV platform 54

3.4 Software 54

- 3.4.1 MicMac 54
- 3.4.2 RTKLib 57

3.1 Introduction

In this chapter, we present a literature review on the main issues discussed in this document, integrated sensor orientation and thermal effect on camera internal geometry. A brief review of contactless metrology techniques is presented in Section 3.2 where common techniques from geomatic field are selected: topometry stations, `GNSS` and `LIDAR` sensors based on optical or electromagnetic wave measurements. Photogrammetry, the image based technique, is presented in more details in Section 3.2.4 as it is the metrology technique that concerns our work. The general processing workflow is presented and internal/external calibration aspects discussed in Sections 3.2.4.1 and 3.2.4.3. In particular, the mathematical modeling of the internal geometry of the camera adopted is detailed. Various works related to the study of the thermal effect are presented in Section 3.2.4.2. This phenomena is discussed in Section 5. The different photogrammetric georeferencing techniques are presented in Section 3.2.4.4 with a focus on integrated sensor orientation.

Afterwards, we give details on the sensors used in our experiment in Sections 3.3.2 and 3.3.3. These sensors are entirely developed internally within the laboratory. The `UAV` is an entry-level model available on the market as an assembly kit or `RTF` format. Furthermore, one of our purposes is to achieve a light system performing accurate absolute georeferencing without exceeding $2kg$ in compliance with the regulations that govern evolution of `UAVs` in the French airspace.

3.2 Contactless Metrology Techniques

As defined in the third edition of the International Vocabulary of Metrology : "metrology is the science of measurement and its application. Metrology includes all theoretical and practical aspects of measurement, whatever the measurement uncertainty and field of application". In other words, metrology focuses on the methods by which the confidence in a measurement can be qualified according to a criteria. It has a specific terminology which differs from the statistical vocabulary. Metrology is present in different fields, such as: scientific fundamental studies, industrial applied work, legal units determination, among others.

Instruments for collecting information on the surface of an object for metrology purposes consist of two main families: contact and contact-less instruments. As part of our work, we are interested in the use of contact-less sensors for metrology purposes. Below, non-contact surface measuring instruments used in the areas related to geographic sciences are discussed.

3.2.1 Topometric Instruments

Topometry is the science that represents the surface of the earth on a flat surface or map by taking measurements or observations to determine the planimetric and altimetric position, shape, and dimensions of any geographic object on that surface [Brabant 2003]. Topometry has used various instruments throughout its history such as theodolites, tachiometers and today fully automated total stations. `GNSS` receivers and levels are among the instruments commonly used in surveying, to determine geographic objects 3D coordinates.

Figure 3.1: Evolution of stations in topometry. Theodolite (right), tachometer (center) and total station (right)

Topometric observations generally consist of measurements of horizontal angles, vertical angles, direct distances and vertical differences. These observations coupled with external measurements such as `GNSS` or geodesy techniques allow to place in one frame all the details of the studied area. In topometry the observations generally apply to dimensions of the order of a few meters up to a few hundred kilometers. The field of action of topometry is fairly wide. From the a classic survey to large-scale development projects, using more precise techniques for the installation of structures to monitoring and control of the latter by means of auscultation techniques for short period of time or very long duration.

Topometry requires qualified operators and increased rigor for acquisition phase of the observations in order to guarantee the optimal precisions offered by the optical instruments, which are often very expensive. In this regard, topometry often requires the materialization of points measured by prisms, which makes the technique flexible. The data acquisition time is quite vast and the spatial resolution is low. It is in this sense that topometry is a contactless metrology technique suitable for small or large scale projects, requiring very high precision (0.1 - 5 cm) but with a low spatial density.

3.2.2 GNSS

As for all `GNSS` data processing, the most important part is fixing phase ambiguities parameters to integer values. In our case, we have to deal with two constraints: a single-frequency `GPS` receiver and a low number of recorded observations. In fact, this `GPS` chip records raw carrier-phase measurements only in the first `GPS` frequency band. As a consequence, the baselines between the reference station and the mobile antenna are limited. For instance, a combination of "iono-free" type frequencies eliminates the ionospheric delay of the first order cannot be used. Here, the ionospheric delay is estimated using the `Klobuchar` ionospheric model [Klobuchar 1987] whereas tropospheric signal delay is corrected using `Saastamoinen` model [Saastamoinen 1972]. However, given the short baselines we have in our standard flight configurations, atmospheric delays being spatially correlated, they are eliminated by differentiation of observations between the station and the rover. Beyond the influence of atmospheric errors which are eliminated, the tracking of the signal is of great importance. During the first experiments, we noticed strong instability due to temperature variations. Indeed, the `GPS` receiver is not protected and its internal clock showed a large drift because of the ambient temperature variations [Benoit 2014]. This problem is solved by putting the receiver in a waterproof box. Also, the manufacturer allows the configuration of the module according to the dynamics of the platform used, up to accelerations lower than 4g, in order to guarantee the quality of the recorded data.

Recorded observations do not generally exceed 15 minutes for a sampling frequency of 1 Hz, which does not allow correct estimation of the phase ambiguities as parameters of the problem. The computation strategy adopted is called "fix-and-hold" [Benoit 2014]. The ambiguities are fixed before `UAV` take-off. Next, the signal is tracked to detect possible cycle-slips for each observed satellite. With this technique, the unknowns yet to estimate are the unknowns of the receiver's position at each epoch. Figure 3.2

shows GPS carrier-phase double-difference geometry between a known reference station coordinates and on-board antenna phase center GPS at epoch t_k.

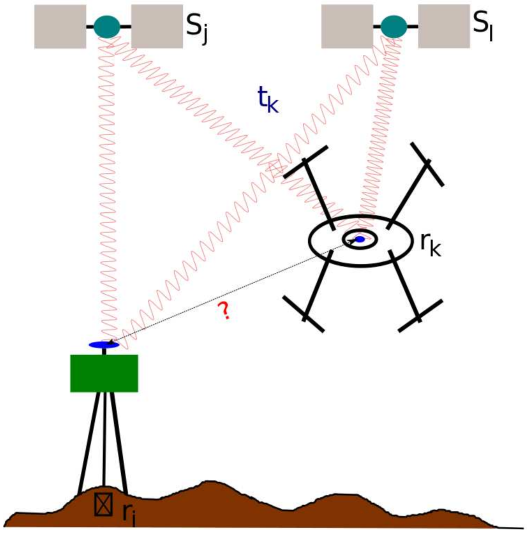

Figure 3.2: The double-difference geometry at a single epoch t_k

The system of equations of double-difference between 2 satellites and 2 receivers expressed in ECEF reference frame at an epoch t_k can be written as follows:

$$\left\{\begin{array}{c} \cdots\cdots \\ \nabla\Delta(\Phi^{s_j,s_l}_{ri,r_k}) = \nabla\Delta(\rho^{s_j,s_l}_{ri,r_k}) - \lambda_1 \cdot \nabla\Delta(N^{s_j,s_l}_{ri,r_k}) \\ -\nabla\Delta(\tau^{s_j,s_l}_{r_i,r_k,iono}) - \nabla\Delta(\tau^{s_j,s_l}_{r_i,r_k,tropo}) - \nabla\Delta(\varepsilon) \\ \cdots\cdots \end{array}\right. \tag{3.1}$$

where: $\nabla\Delta$ = double-difference operator;
$\Phi^{s_1,s_2}_{r_1,r_2}$ = carrier-phase measurements;
$\rho^{s_1,s_2}_{r_1,r_2}$ = geometric distances;
λ_1 = wavelength of GPS first frequency ($\lambda_1 = 19.03\ cm$);
$N^{s_1,s_2}_{r_1,r_2}$ = term of ambiguities;
$\tau^{s_1,s_2}_{r_1,r_2,iono}$ = ionospheric bias;
$\tau^{s_1,s_2}_{r_1,r_2,tropo}$ = tropospheric bias;
ε = multi-path effect and measurement noise.

If at the first epoch t_0, before UAV take-off, an approximate position of our GPS receiver is given with an accuracy higher than $\lambda_1/2 \approx 10\ cm$ the term of double-difference of ambiguities can simply be calculated instead of being estimated using (3.2):

$$\left\{ \begin{array}{c} \cdots\cdots \\ \nabla\Delta N_{r_i,r_k}^{s_j,s_l} = \lfloor \frac{1}{\lambda_1} \cdot (\nabla\Delta(\Phi_{r_i,r_k}^{s_j,s_l}) - \nabla\Delta(\rho_{r_i,r_k}^{s_j,s_l}) \\ -\nabla\Delta(\tau_{r_i,r_k,iono}^{s_j,s_l}) - \nabla\Delta(\tau_{r_i,r_k,tropo}^{s_j,s_l}))\rfloor \\ \cdots\cdots \end{array} \right. \tag{3.2}$$

where: $\lfloor\ \rfloor$ = nearest integer operator

The remaining parameters to estimate in (3.1) are the axial components of the baseline between the reference station and the mobile antenna at each epoch. These parameters are included in double-difference geometric distances terms.

3.2.3 LIDAR

`LIDAR` is a technology that can describe the geometry of a 3D scene from a measurement of the flight time of a beam emitted by a laser. This principle consists of measuring the travel time between the emitting source and the wave reflected by the surface of the object to be modeled. Knowing the speed of light, the distance is deducted from the travel time. `LIDAR` is an instrument used in different fields of applications such as geosciences, environmental sciences, industrial metrology, etc. The application of this technique to the study of the topography appeared in the years 1980 and has seen a significant evolution since the 1990s, thanks to the evolution of the coupling of these instruments with navigation sensors based on inertial measurement units and `GNSS` receivers.

`LIDAR` is a total station-like instrument with the ability to perform a large number of measurements automatically and without the use of a prism. It is an active instrument that has different characteristics, for example: wavelength, measurement frequency, scan frequency, scan angle, laser beam divergence, maximum permitted flight altitude and distance measurement accuracy [Vallet 2002]. There are different types of `LIDAR` depending on the laser scanning mechanism. Most of today's scanner systems are either rotating or oscillating mirror. Figure 3.3 shows the scan pattern on the ground for different laser scanning technologies.

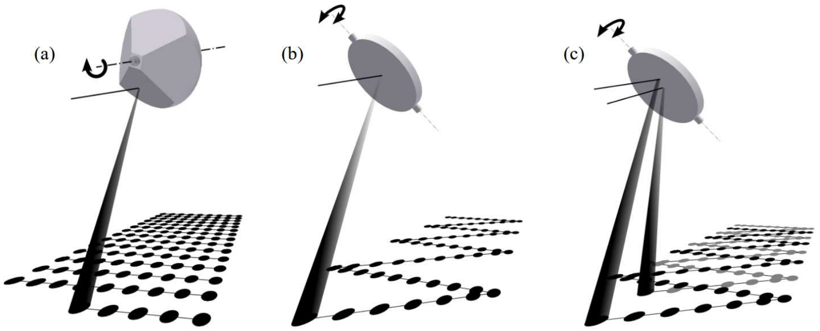

Figure 3.3: Principle of laser scanning mechanisms: rotating polygon wheel (a), single-channel oscillating mirror (b), and dual-channel oscillating mirror (c); source: `ww.riegl.com`

`LIDAR` is positioning itself today as a highly competitive surface metrology technology. Indeed, the technological evolution allows today to have light systems, having low consumption and easy to use. They can be used in terrestrial configuration or embedded on mobile vectors (cars, `UAVs`, aircrafts, ... etc). Laser scanning has several advantages. The 3D geometry of the scene is available quickly after the acquisition. Also, as it is an active technique, it is insensitive to light conditions. The distance measurements have a low noise, which makes it possible to provide centimeter relative accuracy. This precision is compatible with the tolerances practiced in many fields, including requirements in the field of public works. `LIDAR` also allows to obtain informations on the nature of the elements which reflect the wave according to the intensity of the signal. In the other hand, this technology has some disadvantages. First of all, a laser scanner represents a significant financial cost. Terrestrial `LIDAR` has some limitations including range of use and relative angle of incidence to the surface to be modeled. It is thus rather adapted to scenes of small extent. The aerial `LIDAR` is useful for surveying large areas. Its use is relatively complex and its degree of miniaturization has not yet reached a degree of maturity to be embarked on UAVs and used in industrial conditions. Finally the visual interpretation of the scene is more complex with a laser scanner as the scene is represented in a discrete way.

3.2.4 Photogrammetry

Photogrammetry is the science, technique and art of making geometric measurements in three dimensions from two-dimensional stereoscopic images. Photogrammetry is based on fundamental geometric concepts dating back to the 15th century. The appearance of photogrammetry, as a new technique, dates back to 1849 when Aimé Laussedat [1], an officer of the French army, had the idea to use terrestrial photographs of the Hotel des Invalides to perform measurements by making topographic plans of the facades. During certain time, photogrammetry appeared as a complex technique and was intended to be replaced by scanners. Since the 2000s we are witnessing a constant evolution of the discipline. Mainly thanks to the accessibility of imaging sensors, their miniaturization, their growing quality and the considerable contribution of algorithms for automatic detection of points of interest between stereoscopic images and their stability [Grussenmeyer 2016].

Photogrammetry is a contact-less metrology technique that has a large number of advantages: the accuracy is flexible and depends on the ground sampling distance, the technique is applicable with cheap material, data acquisition can be fast, the measurement is instantaneous, the processing is more and more automatic, etc. In photogrammetry, the conic projection hypothesis is used. This means that the rays coming from the same image pass through the same point which is the center of projection. The camera is a rigid object and its movement is characterized by 6 degrees of freedom, a translation and a rotation. The photogrammetric process follows several steps:

1. Detection of points of interest
2. Matching points of interest
3. Internal orientation
4. External orientation
5. Georeferencing
6. Matching
7. Generation of photogrammetric products

The quality of each step has an influence on the final products (3D cloud points and orthoimage). As part of our work the `SIFT` detector is used and the matching of points of interest is done using `ANN` algorithm. The internal orientation is a step that has long been independent from the next step of external orientation. Today these steps are performed at the same time in a self-calibration bundle block adjustment strategy. Different georereferencing techniques can be adopted for sensor orientation depending on the context of acquisition and the on-board sensors. As part of our work we are exclusively

---

[1] 1819-1907

interested in the self-calibration bundle adjustment stage and the georeferencing based on coupling the camera with a `GPS` receiver for integrated sensor orientation approach. A review of these methods is given in sections 3.2.4.1-3.2.4.4. The matching and generation of photogrammetric products can be seen as independent steps and are not the focus of our work.

3.2.4.1 Interior Orientation

The internal orientation is determining the parameters of the model that describes the geometry of the camera. Different methods exist: instrumental methods (such as calibration on an optical bench) or estimation methods (processing image acquisition using a controlled geometry scene such as a calibration polygon). The internal orientation step is mainly today done with the external orientation step. This strategy is known as self-calibration [Fraser 1997]. In photogrammetry there are a multitude of models that describe the geometry of the camera. These models generally describe the camera from a physical point of view [Duane 1971]. The main parameters taken into account are:

- principal distance
- principal point
- radial distortion polynomial

This minimal physical model is generally extended with the following additional parameters: decentering distortion and an affine correction that models the non-orthogonality of the sensor. The distortion radial polynomial is usually modeled up to the 3^{th} order ($\delta r = k_1 r^3 + k_2 r^5 + k_3 r^7$). These models are widely used in aerial or terrestrial photogrammetry. The determination of the physical model that best fits the camera is often estimated from examples of acquisitions, thus on sample measurements. However, it must be ensured that this model is valid outside the learning examples. Measurement samples must also meet certain criteria in order to guarantee the reliability of internal parameters estimation. Among these criteria one can mention: a high density of images and high overlapping rates, a strong relief of the scene, a convergent image acquisition, changes of rotation of the camera, constrain the estimation of the parameters with the use of ground control points of a higher accuracy than the ground spatial distance of the images. The acquisition dedicated to the calibration should be carried out under the acquisition conditions. Most often these calibration data are acquired in terrestrial which introduces effects, in particular on the parameters of distortion, for the configurations of aerial use. Then the analysis of the estimation of the parameters and the deviations on the control points give an indication on the adapted photogrammetric model.

On the one hand, if the model does not have enough degrees of freedom it poorly models the observations. On the other hand, if the model has a large number of parameters, the observation errors are learned by the model. In general, it is recommended to avoid sub-parametrization and over-parameterization. The accuracy needs in photogrammetry led to propose models with more parameters in order to take into account some small imperfections such as sensor defects, the crossing of the porthole, optical filters effects, etc [Jacobsen 2007]. With the evolution of lenses, in particular used with commercial cameras, the complexity of modeling of these systems increases and impacts the capacity to model by simple physical formulation the geometry of the camera. However, the large number of measurements offered by automatic tie points algorithms allow, without taking any risk, to use on one hand high degree distortion radial polynomials coupled to a generic polynomial model which can be interpreted as additional distortion parameters [Tang *et al.* 2012].

We present in section 4.2.1 the formulation of this hybrid camera model which is a composition of two models as well as the strategy adopted during the data processing.

3.2.4.2 Thermal Deformation

Photogrammetric methods have been proved to be particularly useful in engineering where high precision measurements are required [Kölbl 1976]. However, multiple factors can have an impact on photogrammetric accuracy. First of all, a higher resolution of images can result in a higher accuracy since items are more precisely located in images. Secondly, camera self-calibration can be crucial to determining intrinsic and extrinsic parameters of a camera, e.g., focal length, principal point and lens distortion. The quality of camera pose estimation has an important role in photogrammetric accuracy, pose estimation quality increases as the quality of tie point extraction improves, as well as the multiplicity and spatial distribution.

The development of metric cameras enables and facilitates the acquisition and restitution of images with high accuracy. A metric camera is a camera of which interior orientation is known, stable and reproducible [Mcglone *et al.* 1980]. Normally, images taken with metric cameras can be exploited for photogrammetric purposes without additional control of inner and relative orientation. Charge-coupled device (`CCD`) and complementary metal-oxide semiconductor (CMOS) image sensors are commonly used in metric cameras. Traditionally, `CCD` sensors have been thought to produce higher quality images with less visual noise, particularly in low light conditions. However, they consume more energy and provide lower data-throughput speed. Therefore, `CMOS` image sensors have become major players in the solid-state imaging market, a market in which `CCD` image sensors were once the dominant product. `CMOS` image sensors utilize an array of active pixel image sensors and can be easily integrated into `CMOS` process peripheral circuitry since they are made with the same `CMOS` process technology.

[Schwartz 2010] points out that the temperature range of `CMOS` sensors is quite an improvement compared to that of `CCD` image sensors. Nonetheless, the temperature change of `CMOS` image sensors during image acquisitions can still introduce a thermal effect on images. [Lin *et al.* 2010] quantifies the radiometric effect on a `CMOS` image sensor, fixed pattern noise is observed to increase with temperature. [Sauer 2001] presents a method correcting fixed pattern noise of a `CMOS` image sensor which can be a result of temperature changes during standard operation.

The influence of temperature on the internal parameters of the camera is a known effect since the appearance of aerial photogrammetry. In 1958, [Hothmer 1958] lists various sources of errors to be considered in the context of aerial mapping. Among the sources it is mentioned that "the effect of temperature can possibly be considerable". [Yastikli & Jacobsen 2005] specifies that, during flight conditions, the vertical temperature gradient causes a significant deformation of the camera lens. [[Merchant 2006],[Merchant 2012]] investigations carried out with an aerial camera show that the effect of temperature change induces a focal variation of 0.068 pixels per degree. For a flight with a height of 2000m, this effect represents a systematic error of 1 m in elevation. Experience with the `Helimap Mapping System` highlights the importance of the calibration step in the process pipeline and particularly the stability of the camera calibration [Vallet 2007]. The various datasets acquired with this system show that the focal length and the principal point are not very stable. These parameters are mainly influenced by the variation of temperature and vibrations. Over a period of one year the observed variation in focal length is ∼30 microns and ∼15 microns in focal length. [Smith & Cope 2010] presents a study that investigates the influence of temperature on a commercial digital camera. The experiment consists of leaving the camera for several hours in a fridge to lower its internal temperature. The variation observed in the focal length is ∼0.13 pixel per degree. [Fiedler & Müller 2013] study the thermal effect on the `Kinect` sensor. By alternating and combining different states - variation of internal and external temperature, the impact on sensor measurements is proved to be considerable. The distribution of observations show that the increase in temperature can be interpreted as a zoom-in effect.

3.2.4.3 Exterior Orientation

External orientation is the issue of determining the position and orientation of the camera for each image. During this step, the internal parameters of the camera are also determined as described in Section 3.2.4.1. In the following we will only consider the algorithmic aspects of the external orientation, i.e. the estimation of position and attitude of each image.

In the photogrammetric processing workflow, the external orientation is generally divided into two main steps. The first step consist of the determination of initial values based on direct algorithms. The second step is about refining the initial solution based on a number of observations [Grussenmeyer & Al Khalil 2002]. There are different direct algorithms for the estimation of the external parameters, whether for an image, a couple of images or for several images. These algorithms can use different matched geometries: tie points, lines or planes. In photogrammetry, tie points are generally used as image observations for the estimation of external orientation. Space resection and essential matrix are common algorithms used in photogrammetry. In the case where only tie points are used, the exterior orientation is a relative orientation as it is determined to a 3D spatial similarity factor. Some algorithms can use properties of the scene to estimate these parameters, for example in the case of a planar scene where the image transformation can be expressed as a homography. There are different variants of algorithms for calculating the relative orientation of a couple of images using a minimum number of tie points varying between 5 and 8 points (`Stevenius`, `Kalantari`, ...).

There are today a large number of software solutions for automatic orientation of blocks of stereoscopic images. The most part of these software programs implement bundle block adjustment algorithm but with very limited parameterization that sometimes turns these tools to black boxes [Remondino *et al.* 2012]. As part of our work, the exterior orientation is performed with `MicMac` software presented in Section 3.4.1. The external orientation module is called `APERO` [Pierrot-Deseilligny & Clery 2011]. This module offers a fine-tuning of this step of the photogrammetric worflow. The step of computing initial solutions based on tie points uses the essential

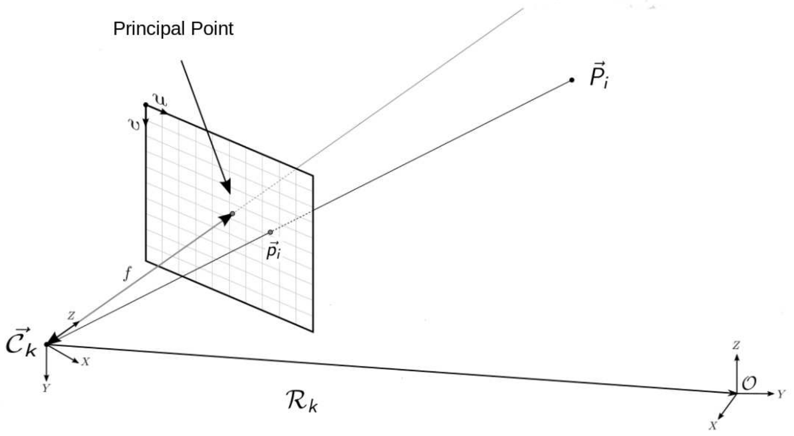

Figure 3.4: The geometry of a pinhole camera; source: [Moulon 2014]

matrix and space resection algorithms in a robust estimation strategy using `RANSAC` [Fischler & Bolles 1987]. The best solution is selected a posteriori according to a quality criteria. The second step consist of a bundle block adjustment [Triggs *et al.* 1999] solved with the `Levenberg-Marquardt` method. The `APERO` offers the possibility to perform this step using heterogeneous observations (tie points, lines, ground control points and `GNSS` centers) which can be coupled to constrained equations (rigid relative orientation, evolution variation of the internal model, ...). Each observation gives one or several equations.

The approach adopted by `APERO` is an energy minimization strategy. Assuming a pinhole camera model (Figure 3.4), the observation equation can be written as follows:

$$\begin{cases} \cdots\cdots \\ \vec{p_i}|_k - \zeta(\pi(\mathcal{R}_k(\vec{P_i} - \vec{\mathcal{C}_k}))) = \vec{0} \\ \cdots\cdots \end{cases} \tag{3.3}$$

where: $\vec{p_i}|_k$ vector of $2d$ image coordinates of point i on image k;
ζ is a $\mathbb{R}^2 \rightarrow \mathbb{R}^2$ application describing the camera model;
π is a $\mathbb{R}^3 \rightarrow \mathbb{R}^2$ projective application;
$(\vec{\mathcal{C}_k}, \mathcal{R}_k)$ position and orientation of image k;
$\vec{P_i}$ vector of $3d$ position of point i.

The expression minimized by can be written as follows:

$$E = \sum_{i,k} \frac{(\vec{p}_i|_k - \zeta(\pi(\mathcal{R}_k(\vec{P}_i - \vec{\mathcal{C}}_k))))^2}{\sigma_{pix}} \tag{3.4}$$

The module offers the user the possibility of setting the weighting and rejection thresholds for each type of observation. Among the accessible quality indicators we can mention: average reprojection error for each image, the number of tie points, the multiplicity of tie points, the percentage of rejected tie points during the adjustment, the uncertainty on the estimation of the parameters. The reader interested in the details of the `APERO` module is invited to consult [Pierrot-Deseilligny 2017].

3.2.4.4 Georeferencing Techniques

There are different georeferencing techniques in photogrammetry. The purpose of georeferencing is to express the external orientation in an absolute coordinate system where the different photogrammetric products will be generated. In the following, we present the main georeferencing strategies for sensor orientation.

Indirect sensor orientation is the most widely used technique in aerial photogrammetry for small scale areas. It consists of measuring ground control points whose coordinates are used to convert the external orientation from an arbitrary relative coordinate system to an absolute coordinate one. The coordinates of ground control points are generally measured by conventional topometry techniques (total station, static or real time `GNSS` measurements). This georeferencing method is relatively simple but is unsuitable in certain cases such as the survey of large areas (or requires a large number of `GCPs`) or inaccessible areas. The survey of `GCPs` requires considerable field work whose cost is not negligible. Furthermore, this sensor orientation method requires the processing of a large number of tie points in order to estimate relative positions and orientations. This implies a considerable processing time and is conditioned by the fact that the scene has enough texture for the detection of points of interest. The spatial distribution of tie points and `GCPs` as well as their multiplicity determine the external orientation accuracy. However, one of the advantages of this technique is the possibility of performing camera self-calibrating thanks to the presence of a large number of image measurements and the constraint of the bundle block adjustment by the presence of a generally sufficient number of `GCPs`.

Integrated Sensor Orientation is the technique used to determine the external orientation based on one or several embedded sensors. Aerial photogrammetry has undergone a revolution with the appearance of on-board sensors for trajectories estimating. The first technique is to use a `GPS` receiver to determine the projection center called `GPS-AT` [Colomina 1993]. In parallel the concept of direct georeferencing by `GPS/INS` integration [Skaloud 1999]. Direct integrated sensor orientation consists of directly measuring, in real time or delayed time, the position and the orientation of the images thanks to embedded sensors [Skaloud 2002]. These sensors consist at least of a `GNSS` receiver and an inertial unit. With this technique, image measurements are directly georeferenced. The internal orientation parameters and the offset between the sensors are generally known and the external parameters are determined by `GPS/INS` integration. These external parameters are fixed during bundle block adjustment performed without the use of `GCPs` [Skaloud *et al.* 1996]. This georeferencing technique is mainly used in large scale mapping surveys as well as on linear configuration sites (single flight strip). In general decimeter to centimeter accuracy can be achieved with the use of high end sensors and rigorous pre-calibration procedures. Better accuracy can be achieved in relative aerial configuration [Blázquez & Colomina 2012] with the use of ground control points and thousands of tie points. In this case the self-calibration approach can be adopted for internal orientation and lever-arm/boresight calibration parameters are not mandatory ans thus the processing chain is facilitated. The evolution of full aerial control integrated senor orientation and a summary of different approaches can be found at ([Colomina 1999],[Colomina 2007]). Today high-quality inertial units still have a high cost. Moreover, in the configuration of integrated sensor orientation with absolute aerial control, the mass of the on-board sensors is unsuitable for `UAV` platforms and their miniaturization has not yet reached an acceptable degree of compatibility to achieve calorimetric accuracy. Today, this georeferencing technique is mainly used in large scale mapping surveys as well as on linear configuration sites (single flight band for example).

For over a decade, we have been witnessing an evolution in the development of `UAV` systems. These systems are nowadays increasingly miniaturized, lightweight, and carry various sensors. These systems have a very high potential due to the fact that the fields of applications are various. For example `UAV` photogrammetry is employed in agriculture [Grenzdörffer *et al.* 2008], forestry [Lisein *et al.* 2013], cultural heritage [Eisenbeiß 2004], 3D modeling dedicated to archeology [Remondino *et al.* 2011], metrology and monitoring [Tournadre *et al.* 2014], geology [Niethammer *et al.* 2012], etc. Moreover, as regulation of air space evolves, it gives these airborne systems the opportunity to grow in the context of a clear regulatory framework. `UAV` photogrammetry takes advantage of this trend to establish itself as an essential application of aerial photography today ([Eisenbeiß 2009],[Colomina & Molina 2014]). Since the advent of `UAV` photogrammetry, relative and absolute integrated sensor orientation approaches have been transposed to these new types of mobile platforms [Rehak & Skaloud 2016]. Large studies have been investigating integrated sensor orientation using absolute exterior orientation based on position observations only or on position and attitude observations with the purpose to achieve maximum accuracy without the use of ground control points or to considerably reduce their number (for example assisted aerial triangulation with 1 `GCP`). The absolute aerial control based on GPS/INS integration is not adapted to lightweight `UAV` systems due to the limited quality of the inertial sensors. However, other fusion approaches can improve accuracy compared to the classical workflow [Cucci *et al.* 2017]. In the case of our work, we focus on integrated sensor orientation with absolute and relative position control strategies to perform centimeter mapping accuracy. Our system is based only on a `GPS` ship and a camera without using any navigation sensor. The absolute and relative aerial control using a `GNSS` receiver have many advantages as it reduces considerably the number of `GCPs` and allows the use of single-frequency carrier-phase receivers [Skaloud *et al.* 2014]. Early researches focuses on the "low-cost" aspect of on-board sensors and platforms ([Bendea *et al.* 2008], [Bláha *et al.* 2011], [Stempfhuber & Buchholz 2011], [Pfeifer *et al.* 2012],[Chiang *et al.* 2012]). These solutions are generally based on single-frequency C/A code observations which is certainly sufficient for navigation, but the aerial position control accuracy remains metric and do not fit industrial applications. ([Turner *et al.* 2014],[Mian *et al.* 2015],) achieved decimeter to centimeter accuracy based on dual-frequency `GNSS` receivers. ([Rehak *et al.* 2013], [Rieke *et al.* 2011]) achieve a typical absolute georeferencing accuracy of 1-5 cm with the use of 0 or 1 ground control point. Recent studies comparing the use of a low-cost `GNSS` receiver and a geodetic grade `GNSS` receiver have shown that the degree of accuracy achieved by these two types of receivers is equivalent [Rehak & Skaloud 2017a] under optimal conditions.

3.3 Hardware

After reviewing contactless metrology techniques related to the field of geographic sciences and presenting with more details the adopted technique (photogrammetry) and different concepts of sensor orientation, we will focus in this section on hardware aspects. We present an overview of existing commercial solutions, then we present the sensors used in our work.

3.3.1 Off-the-shelf Solutions

Nowadays there are many commercial `UAV` solutions dedicated to aerial photogrammetric acquisition. These `UAVs` are equipped with navigation sensors that allow metric sensor orientation when synchronization with the camera is proposed. Since the years 2010 and the constant evolution of `UAVs` platforms and miniaturization of `GNSS` receivers and antennas, more and more commercial solutions allow accurate aerial positioning control. These solutions are often based on multi-frequency `GNSS` receivers and high-end antennas. These platforms generally works on the principle of real time kinematic (`RTK`) estimation of the `UAV` trajectory. Therefore the accuracy of positioning depends mainly on the quality of the `GNSS` receiver carrier-phase measurements and the `RTK` engine. The embedded cameras are almost exclusively commercial devices, sometimes modified to achieve accurate time synchronization and better interior orientation stability. Figure 3.5 presents principal commercial solutions dedicated to photogrammetry acquisition and allowing accurate aerial position control and Table 3.1 compare these solutions according to different criteria.

Specifications	eBee	MAVinci	BRAMOR	Aibotix
Absolute Precision (cm)	3.0	5.0	1.5	-
Mass (Kg)	0.73	2.7	4.5	4.6-6.6
Autonomy (h)	0.6	0.75	2.5	0.3
GPS Module	RTK	RTK 100 Hz	RTK 20 Hz	RTK
Maximum GSD (cm)	1.5	1.6	0.9	$<$ 1 cm
Price (k€)	25	30	58	20

Table 3.1: Comparison of `UAV` off-the-shelf solutions with respect to different criteria

These solutions are largely fixed-wing `UAVs` except the `Aibotix` model which is a hexacopter. These platforms mass exceed 2 kg which is not suitable to operate in a more flexible way from UAV air law point of view (except for the `BRAMOR` model). For fixed-wing models, the ground sampling distance value is limited because of the minimum flight height required. However, for these same models the flight autonomy is comfortable. Finally, the financial cost of


eBee MAVinci
BRAMOR Aibotix

Figure 3.5: Panel of off-the-shelf solutions

these solutions is quite important and does not allow a large scale deployment of these solutions as part of a large corporate structure.

3.3.2 IGN lightweigth metric camera

Nowadays, `UAV` photogrammetry allows to achieve high accuracy under optimal acquisition conditions. Most of the time, commercial cameras are used in the acquisition and a self-calibration with ground control points is required [Nex & Remondino 2014]. However, there is a need of light metric camera for more rigorous acquisitions. There are some "photogrammetric optimizations" applied to commercial cameras by users in order to improve the internal orientation stability [Klaas Pauly 2017], e.g., locking screw in focus and aperture rings. Moreover, some manufacturers offer lightweight professional cameras "optimized for `UAV` photogrammetry acquisitions " [Francois Gervaix 2017]. Nevertheless, the performance of these cameras is not yet evaluated by photogrammetry community. To our knowledge, the only light metric camera for photogrammetric `UAV` surveys, besides the `IGN` camera presented below, is the `MACS-Micro` system [Kraft *et al.* 2017]. One of the characteristics of this system is the stability of internal parameters. The deviations observed over one year are smaller than the pixel pitch of the sensor [Kraft *et al.* 2016].

`CamLight`, the metric camera employed for research here is a home-made camera which meets the needs of close range photogrammetric `UAV` acquisitions. Team `LOEMI` of `LaSTIG IGN` laboratory started to design this new imaging system (Figure 3.6) in 2012 after having studied market demands of the image sensor and the processor of the camera [Martin *et al.* 2014].

Figure 3.6: An image of `CamLight`

In the past decades, the number of companies using different types of `UAVs` for large scale aerial photography has increased significantly. Cameras embarked on `UAVs` for aerial photographic uses are preferred to be light; lightweights allows to have an integrated system with `UAVs` with low payload and an increase of autonomy. `CamLight` with a lens included, has a low mass of 300g and gives possibilities for future applications.

To avoid the shearing effect (Figure 3.7), induced by rolling shutters in the case of a moving camera or a mobile subject, a global shutter is adopted in `CamLight`. In terms of image sensor, both `CCD` and `CMOS` image sensors suit this metric camera. In practice, a low frame rate can be a limitation when a camera is embarked on high speed drones. Therefore, `CMOS` image sensors are eventually chosen for the capability of high acquisition rates. For `CamLight`, a full frame image sensor `CMOSIS CMV20000` of 20M pixels (5120×3840) offers a frame rate up to 30 images per second [CMOSIS 2015]. The camera is used in its monochromatic version with the benefits of a better spatial resolution.

Furthermore, a `GPS` chip module can be integrated within the same enclosure to provide measurements of camera position when each image is taken.

Since the prototypes of `CamLight` became available, several aerial photogrammetric acquisitions have been made. [Tournadre 2015] utilized `CamLight` for

Figure 3.7: Examples of shearing effect

linear aerial photogrammetric acquisition in the context of `DEM` restitution of dykes. [Daakir *et al.* 2017] integrated a single-frequency `GPS` receiver to `CamLight` for metrology applications: centimeter accuracy can be achieved with a system consisting of low-cost `UAV` and `GPS` module coupled with `CamLight`. [Audi *et al.* 2017] employs `CamLight` to acquire several images with a short exposure time and presents an image processing algorithm to produce a stacked image equivalent to an image with a long exposure time; this operation avoids motion blur due to the erratic movements of the `UAV` with long exposure time.

For temperature recording, the `CMOSIS CMV20000` incorporates a temperature recorder that provides a value which can be translated to a device temperature [CMOSIS 2013]. This value depends on an offset which equals the value of the register at $0°C$ and a slope, both are input clock frequency dependent.

$$Temperature[°C] = \frac{Register\ value[DN] - Offset[DN]}{Slope[\frac{DN}{°C}]}$$

The temperature recorded is quite close to the absolute temperature as we use typical calibration values offered by constructors. However, these parameters vary slightly from recorders and need to be re-calibrated when the absolute temperature is required. In our research, we are only interested in the variation of temperature.

The recorded temperature is the image sensor temperature and does not fully equal to the temperature of the camera. However, we consider it as the internal temperature of the camera as it is complicated to separate completely the thermal effect introduced by internal and external temperature. In our research, the external temperature is the room temperature and is assumed to be constant during calibration acquisitions. Therefore, we consider the external temperature constant; the thermal deformation is entirely induced by the variation of the internal temperature and a zoom-in effect is expected.

3.3.3 IGN GeoCube

The `GPS` module chosen is the one used by the `GéoCube`, a multi-sensor geo-monitoring system developed at the `IGN LOEMI` team. The `GéoCube` was initially developed for deformation monitoring applications [Benoit *et al.* 2015] over long periods of static observation sessions. In this study, the `GéoCube` is used in a kinematic configuration. The integrated `GPS` chip is the `u-blox LEA-6T-0-001` model ([u-blox 2015],[u-blox 2013]). It records raw C/A code, carrier-phase and Doppler data of `GPS` satellites constellation on `GPS L1`[2] band. Post-processing of recorded data makes it possible, for short baselines, to get an accurate relative positioning with respect to a known reference station.

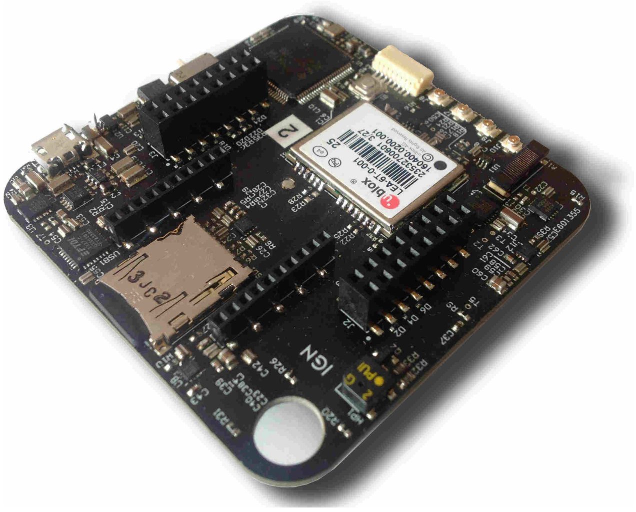

Figure 3.8: `IGN GéoCube`

---

[2] 1575.42 MHz

3.3.4 UAV platform

The `UAV` used in our experiments is a type of `F-550` model developed by `DJI` [DJI Innovations 2015a]. This `UAV` is a hexacopter which allows a more stable flight, making it a good choice for aerial photography. This `UAV` uses the `WOOKONG-M` [DJI Innovations 2014] autopilot, also developed by `DJI`. This system offers a flight control software, `DJI Ground Station` [DJI Innovations 2015b], to allow performing acquisitions in automatic mode. One disadvantage of this model is its flying range that remains below 15 minutes. However, this `UAV` can take-off with a payload capacity of only $2kg$. It is very affordable: the assembled copter is available on-line for under €500.

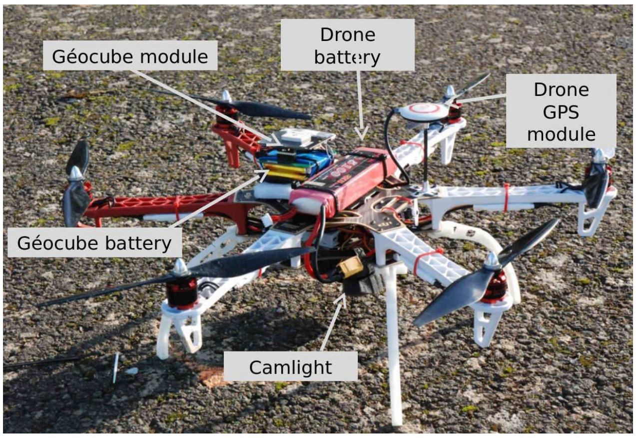

Figure 3.9: `UAV` prototype developed during our work

3.4 Software

In this section, we will present the main software solutions used in the frame of our study. Firstly, these software are free and open-source. In addition, they allow the user a very fine setting of the algorithms that intervene in the processing of acquired data.

3.4.1 MicMac

A brief history of MicMac

`MicMac` is a free and open-source photogrammetric solution. In 2003, Marc Pierrot Deseilligny began developing the software to meet `IGN`'s internal needs. In particular, this requirement consisted in developing a generic image matching code for `DSM` generation and 2D displacement maps. In parallel, the development of a bundle block adjustment module was started, which will then give the `Apero` module for automatic calibration and orientation of set of images. In 2005, `XML` interfacing format is adopted for passing parameters to the various modules existing in `MicMac`. In 2007, the software was distributed under the `CECILL-B` license. In 2010, simplified command line tools emerged to make the software more accessible to less expert users. Since 2012, `MicMac` has benefited from the financing of a few collaborative projects such as `Culture3D` and `Monumentum`, allowing the portability of the software to other platforms (`Windows` and `Mac OS`) and graphical image measurement interfaces under `QT`.

`MicMac` has a number of advantages over existing photogrammetric solutions. As well as being free and open-source, it offers a very precise control of the parameters of each calculation step. It allows all intermediate results to be exported in open formats so that the user can control the quality at each stage. `MicMac` is modularly designed and can be used, for example, only for the adjustment stage or for image matching only. `MicMac` supports images with conical geometry and matrices (satellite imagery). It incorporates a large number of camera models. It is now used in production at `IGN` and in photogrammetric course at `ENSG`, but also in various research laboratories (`MAP-CNRS`, `CEREMA`, `INRAP`, `IPGP`) and by private companies (`Thales`, `Vinci`, `AvionJaune`). However, `MicMac` has some disadvantages: access to a large number of parameters sometimes makes it a very complex tool and thus reserved for researchers and experts. The processing time of large datasets can be a blocking point and suffers particularly from the computation time of tie points. Finally, the absence of a general graphical user interface restricts its diffusion to the great public.

Organization of MicMac

`MicMac` is organized according to various possible levels of use. The user can use the internal `ELISE` library, which offers several tools such as: image processing filters, reading/writing `TIFF` format or matrix computation. In fact, `MicMac` uses few external libraries. Using the `XML` format offers an extensive level of parameterization as well as the possibility to adapt the algorithms to the user's needs or even create specific models. The vast majority of `MicMac` community uses the command line interfaces which are programs calling `MicMac` core modules with `XML` files according to particular parameters

```
************************************************************************
**                                                                    **
**    MicMac: a  free open source project  for photogrammetry         **
**     hosted at Ecole Nationale des Sciences Geographiques           **
**               in Marne-la-Vallee, for IGN-France                   **
**                                                                    **
**                                                                    **
**  The project is funded by :                                        **
**                                                                    **
**  - Institut National de l'Information Geographique et Forestiere   **
**    (IGN main funder since 2003)                                    **
**  - the french FUI Project "Culture 3D Cloud" (and MAP-CNRS)        **
**  - the french ANR Project "MONUMENTUM"(collaborating with MAP-CNRS)**
**                                                                    **
**  Research also currently supported by :                            **
**  - CNES (French Space Agency) - via TOSCA Committee (and IPGP)      **
**  - Compagnie Nationale du Rhone                                    **
**  - Vinci-Construction-Terrassement                                 **
**  - ERC Advanced Grant A.Kaeaeb "ICEMASS" (University of Oslo)      **
**                                                                    **
**                                                                    **
**  Current Team: MP Deseilligny, D Jouin, J Belvaux, G Maillet,      **
**    L Girod, E Rupnik, JM Muller, M Daakir, TG Nguyen               **
**                                                                    **
**    Contact for participating : Marc.Pierrot-Deseilligny@ensg.eu    **
**                                                                    **
**    Hope you enjoy, todo list in case of any problem using MicMac : **
**      (0) Take a Pastis                                             **
**      (1) Switch your computer off and on again                     **
**      (2) Install it on Gnu-Linux (work better on)                  **
**      (3) See the wiki at http://micmac.ensg.eu/                    **
**      (4) Contact the forum http://forum-micmac.forumprod.com/      **
**                                                                    **
************************************************************************
```

Figure 3.10: `MicMac` logo (left) and the famous banner displayed at the end of each processing step (right)

configuration. A number of `GUI` exist but do not offer the same experience of use and are generally limited to classical photogrammetric configurations. Figure 3.11 gives an image of the standard architecture.

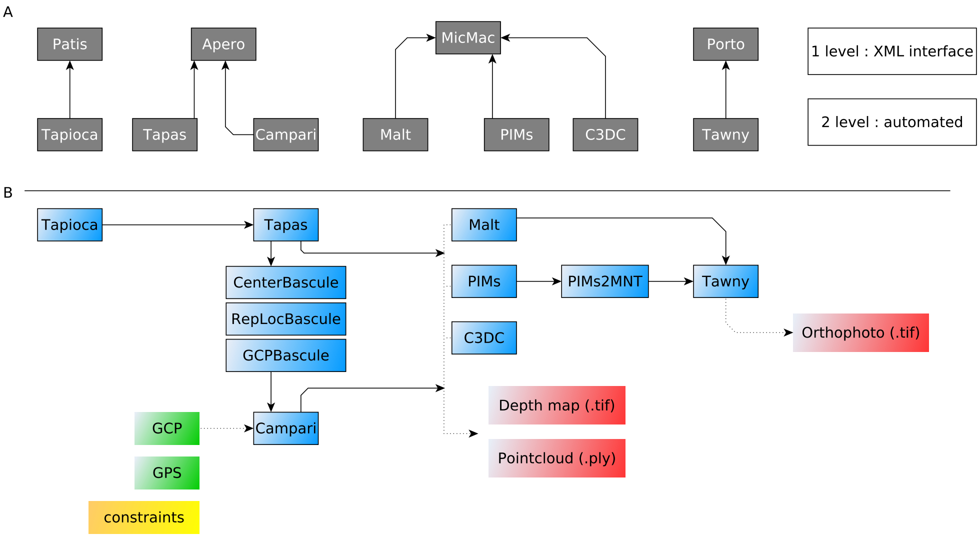

Figure 3.11: Organization of `MicMac` in different layers; source: [Rupnik *et al.* 2017]

Main algorithms

From an algorithmic point of view `MicMac` mainly use:

- `SIFT` for the detection and description of points of interest
- `ANN` for points of interest matching
- `BBA` for pose estimation
- Self-calibration of camera
- `SGM` algorithm for depth reconstruction

`MicMac` also integrates a multitude of algorithms specific to each major step of photogrammetric processing, such as:

- An improved `SIFT` detector
- Several tie points filters
- Constraint `BBA` using heterogeneous observations: tie points, lines, `GNSS` centers, `GCPs`, rigid relative orientation between cameras
- 2D Matching, for example in movement detection

The reader interested in the features offered by `MicMac` can refer to [Rupnik *et al.* 2017] which gives a general overview of the software, and for further details refer to [Pierrot-Deseilligny 2017].

3.4.2 RTKLib

A brief history of RTKlib

`RTKlib` is an open-source program package for `GNSS` positioning [Takasu & Yasuda 2009]. It has been developed by Takasu Tomoji from Tokyo University of Marine Science and Technology since 2006 and has been distributed under the `BSD 2` clause license. `RTKlib` is a portable program library providing several features [Tomoji 2013] (satellite and navigation system functions, post-processing positioning, integer ambiguity resolution). It supports several positioning satellites constellations: `GPS`, `Glonass`, `Galileo`, `QZSS`, `BeiDou`, `SBAS` and many input open formats: `RINEX` observation files, navigation and precise ephemeris files, `NMEA` and `RTCM`, clocks and antenna corrections. `RTKlib` also provides different standard communication protocols, such as serial, `TCP`/`IP` and `NTRIP` as well as the conversion of some proprietary receiver raw data and `BINEX` to open formats (`NovAtel`, `u-blox`, `Hemisphere`, `Javad`, ...etc) and offers some pre-processing features of `GNSS` data.

Organization of RTKlib

`RTKlib` can be used at different levels of difficulty. It offers an `API` that integrates the majority of state-of-the-art algorithms in `GNSS` positioning. `CUI` tools that allow real-time or post-processing modes and `GUI` tools that carry out the same processing as the tools on the command line. Graphical applications include:

- `RTKNAVI`: Real-time positioning application,
- `RTKPOST`: Post-processing analysis application,
- `RTKCONV`: Translates receiver raw data to `RINEX` observations and `RINEX` navigation files,
- `RTKPLOT`: View observations and positioning solutions,
- `RTKGET`: Download data from a `CORS` network and `IGS` precise `GNSS` products

Command-line applications include:

- `RTKRCV`: Real-time positioning application,
- `RNX2RTKP`: Post-processing analysis application,
- `POS2KML`: Convert solution file to `Google Earth KML` format,
- `CONVBIN`: Translates receiver raw data to `RINEX` observations and `RINEX` navigation files,
- Translates receiver raw data to `RINEX` observations and `RINEX` navigation files,
- `STR2STR`: Input data from a stream and divide and output them into multiple streams

Main algorithms

`RTKlib` provides a `Kalman` filter that supports different positioning modes: standard absolute positioning on the code, differential positioning on the code, static and kinematic carrier-phase differential positioning, static and kinematic carrier-phase absolute positioning in `PPP` [Subirana *et al.* 2013]. It supports single frequency, dual frequency, and triple frequency receivers [Takasu & Yasuda 2008]. `RTKlib` offers the usual `GNSS` data processing tools

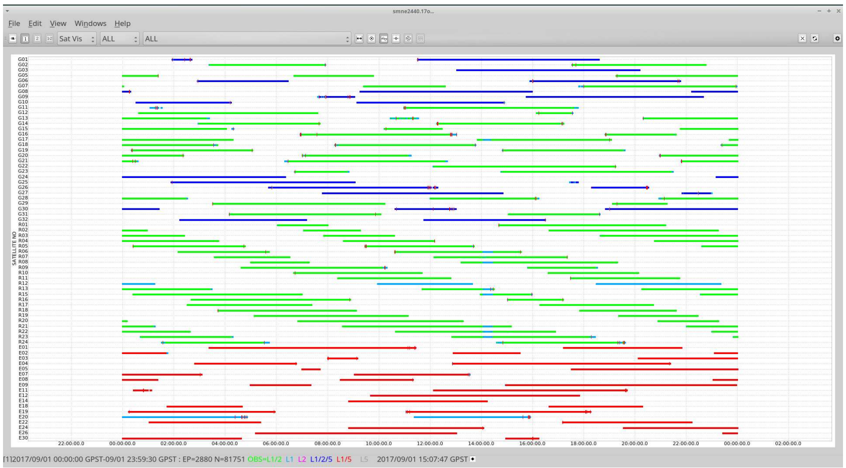

```
[1]2017/09/01 00:00:00 GPST-09/01 23:59:30 GPST : EP=2880 N=81751 OBS=L1/2 L1 L2 L1/2/5 L1/5 L5 2017/09/01 15:07:47 GPST
```

Figure 3.12: Satellite visibility analysis under `RTKPLOT` application

such as a `PRN` filters, `SNR` filter on carrier-phase measurements, atmospheric corrections (ionosphere and troposphere). `RTKlib` also supports the use of precise ephemeris and clock corrections as well as antenna corrections. Different Integer Ambiguity Resolution strategies are available. The most effective is the "fix-and-hold" strategy: once ambiguities are fixed, they are maintained as long as the satellite is locked. Several constraints can be applied in order to improve the robustness and fidelity of the resolution such as the validation threshold or the minimum lock count to fix integer ambiguity [Tomoji 2013]. Statistics on measurements standard deviations (pseudo-range, carrier-phase, `Doppler`, clock stability, accelerations, atmospheric delays) can be set in order to parameterize the `Kalman` filter to meet the receiver specificities, in particular in the context of the use of low-cost `GNSS` receivers.

Chapter 4

Integrated Sensor Orientation

Contents

4.1 Introduction . . . 62

4.2 Calibration aspects . . . 63

  4.2.1 Intrinsic Camera Calibration . . . 63

  4.2.2 Lever-Arm Calibration . . . 64

    4.2.2.1 Auto-calibration method . . . 65

    4.2.2.2 Pseudo-materialization method . . . 68

    4.2.2.3 Conclusion . . . 75

  4.2.3 Synchronization Issue . . . 77

  4.2.4 GPS positions & Camera Centers matching . . . 81

4.3 Data Fusion . . . 84

4.4 Experimental Data . . . 87

  4.4.1 Calibration flight . . . 88

  4.4.2 Second flight . . . 88

  4.4.3 GCPs Vs GPS . . . 89

4.5 Conclusion . . . 91

This chapter corresponds to:

- *[Daakir et al. 2017] M. Daakir, M. Pierrot-Deseilligny, P. Bosser, F. Pichard, C. Thom, Y. Rabot and O. Martin. Lightweight UAV with on-board photogrammetry and single-frequency GPS positioning for metrology applications . ISPRS Journal of Photogrammetry and Remote Sensing, vol. 127, pages 115-126, 2017. Geospatial Week 2015.*

- *[Daakir et al. 2016] M. Daakir, M. Pierrot-Deseilligny, P. Bosser, F. Pichard, C. Thom and Y. Rabot. Study of lever-arm effect using embedded photogrammetry and on-board GPS receiver on UAV for metrological mapping purpose and proposal of a free ground measurements calibration procedure. ISPRS - International Archives of the Photogrammetry, Remote Sensing and Spatial Information Sciences, vol. XL-3/W4, pages 65-70, 2016.*

- *[Daakir et al. 2015] M. Daakir, M. Pierrot-Deseilligny, P. Bosser, F. Pichard and C. Thom. UAV onboard photogrammetry and GPS positionning for earthworks. ISPRS - International Archives of the Photogrammetry, Remote Sensing and Spatial Information Sciences, vol. XL-3/W3, pages 293-298, 2015.*

4.1 Introduction

This section presents a coupled system consisting of a single-frequency `GPS` receiver and a light photogrammetric quality camera embedded in an Unmanned Aerial Vehicle. The aim is to produce high quality data that can be used in the context of metrology applications. The issue of Integrated Sensor Orientation of camera poses using only `GPS` aerial accurate position control is presented and discussed. The accuracy reached by this system based on sensors developed at the French Mapping Agency (`IGN LOEMI`) Opto-Electronics, Instrumentation and Metrology team is qualified. These sensors are specially designed for close-range aerial image acquisition with a `UAV`. Lever-arm calibration and time synchronization are presented and performed to reach maximum accuracy. All processing steps are detailed from data acquisition to quality control of final products. We show that, under optimal conditions, an accuracy of a few centimeters (~ 2 cm) can be reached with this system which uses low-cost `UAV` and `GPS` module coupled with the `IGN` home-made camera.

4.2 Calibration aspects

In this section we present the global processing workflow developed within our work. Calibration issues are addressed in order to estimate the influence of each step on the final photogrammetric localization accuracy. In Section 4.2.1, a hybrid internal calibration model of the camera is presented. In Section 4.2.2 the issue of lever-arm estimation is studied. The conventional method of in-flight determination is compared to new method based on photogrammetric measurements. The importance of time synchronization between the `GPS` receiver and the camera is reminded in Section 4.2.3 and an example of electronic delay instability for a commercial camera is shown. In Section 4.2.4, a criterion for camera centers and `GPS` positions matching is proposed in the case of a time synchronization but without information in the meta-data of the images.

4.2.1 Intrinsic Camera Calibration

A critical point in close-range aerial photogrammetry configurations is the estimation of internal parameters by self-calibration technique. With many recent studies on the processing of `UAV` embedded data, the geometric configuration of acquisitions puts forward the drift effect of poses estimation also known as the `bowl effect`, resulting in inaccurate estimates of internal parameters in the bundle block adjustment ([James & Robson 2014a], [Wu 2014]). A strategy, as given in [Tournadre *et al.* 2015], minimizes this effect by combining two kinds of distortion models: a radial and a non radial one. This strategy can be described by the following steps:

1. initializing simple camera model from a sub-set of images
2. using this camera model to estimate all poses
3. using a physical camera model with more parameters and estimates poses in a self-calibration method
4. locking the physical camera model and add a polynomial model

The expression of the system of equations to minimize during the bundle block adjustment can be expressed as follows:

$$\left\{ \begin{array}{c} \cdots\cdots \\ \vec{p_i}|_k - \zeta(\pi(\mathcal{R}_k(\vec{P_i} - \vec{C_k}))) = \vec{0} \\ \cdots\cdots \end{array} \right. \tag{4.1}$$

where: $\vec{p_i}|_k$ vector of $2d$ image coordinates of tie point i on image k;
ζ is a $\mathbb{R}^2 \rightarrow \mathbb{R}^2$ application describing the camera model;
π is a $\mathbb{R}^3 \rightarrow \mathbb{R}^2$ projective application;
$(\vec{\mathcal{C}_k},\mathcal{R}_k)$ position and orientation of image k;
$\vec{P_i}$ vector of $3d$ position of tie point i.

The processing strategy results in the expression of $\zeta(x, y)$ composed of two applications $\zeta_2 \circ \zeta_1(x, y)$ where ζ_1 describes the physical part of the camera model including a high-degree radial polynomial δr and ζ_2 a lower polynomial degree δp for the non-radial residual errors remaining, expressed as follows:

$$\delta r = \sum_{i=1}^{i=7} a_{2i+1} r^{2i+1} \tag{4.2}$$

$$\delta p(x, y) = \sum_{i=1}^{i=7} \sum_{j=1}^{j=7} a_{ij} x^i y^j \tag{4.3}$$

In conventional aerial photogrammetry, it is very common to estimate three parameters for the radial polynomial function used to correct the distortion (r^3, r^5, r^7). Not only was it justified by the use of aerial camera with high professional quality optics but also because of the risk of over-parametrization which is considerable with the low number of manual image measurements. On the one hand, nowadays the risk of over-parametrization with the use of high degree polynomial disappear due to adjustment on thousands of tie points per image resulting from automatic algorithm. On the other hand, the use of standard optics with complex aspherical lenses and relatively high distortion cannot be modeled with a low degree model. The experiment shows that the use of a high degree radial polynomial combined with a lower degree non-radial polynomial improves the accuracy of internal parameters estimation during bundle block adjustment self-calibration ([Tang 2013],B.3.1).

4.2.2 Lever-Arm Calibration

To achieve accurate integrated sensor orientation, it is essential to consider the vector between the optical center of the camera and the phase center of the `GPS` antenna. There are several techniques to determine this vector. In a static way: the drone is positioned over a scene that contains georeferenced targets. This technique enables static `GPS` processing, therefore a more accurate `GPS` positioning but requires a considerable time of acquisition (each image may require several hours of `GPS` carrier-phase observations). The second method consists in using tacheometric measurements and terrestrial photogrammetry [Rehak & Skaloud 2015]. This method can be replaced by a $3D$ modeling of

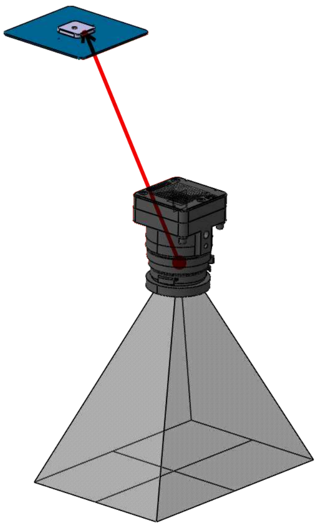

Figure 4.1: Visualization of the spatial offset (in red) between the optical center of the camera and the antenna phase center; source: `LOEMI`

the `UAV` before take-off with the sensors mounted with their centers (optical and antenna phase) previously calibrated according to materialized targets on the sensors. This technique has the advantage of being always valid, even if relative positions of the sensors change from one acquisition to another. This last method is an instrumental calibration method performed by photogrammetric measurements [Daakir *et al.* 2016]. It is the most conventional and common method. A calibration flight over a scene that contains georeferenced targets is performed [Daakir *et al.* 2015].

4.2.2.1 Auto-calibration method

Once the relative camera poses are estimated, the `GPS` trajectory is processed and the `GPS` positions corresponding to images centers are extracted, we have yet to estimate, at least, 10 parameters to achieve the georeferencing of the acquisition, assuming that the time synchronization is perfect. Out of these 10 parameters, 7 correspond to the spatial $3D$ similarity and the remaining 3 to the axial components of the lever-arm vector. The system of equations used can be written for an image k as follows:

$$\left\{ \begin{array}{c} \cdots\cdots \\ \vec{\mathcal{G}_k}|_t - \mu \cdot \mathcal{R} \cdot \vec{\mathcal{C}_k}|_r - \vec{\mathcal{T}} - \mathcal{R} \cdot \mathcal{R}_k^T \cdot \vec{\mathcal{O}} = \vec{0} \\ \cdots\cdots \end{array} \right. \tag{4.4}$$

where: $\vec{\mathcal{G}_k}|_t$ = `GPS` position of image k expressed in absolute frame;
μ = scaling factor;
$\mathcal{R}$ = global rotation
$\vec{\mathcal{C}_k}|_r$ = image k center expressed in relative frame;
$\vec{\mathcal{T}}$ = global translation;
$\mathcal{R}_k$ = image k orientation;
$\vec{\mathcal{O}}$ = lever-arm vector.

In close-range photogrammetry aerial configuration, the orientation of the camera remains almost identical throughout the flight. The `UAV` flight controller system tends to stabilize at horizontal, which gives images a constant altitude. It is possible to solve the system of equations (4.4) relying only on `GPS` data. However, this configuration of acquisition introduces a strong correlation between the parameter of global translation $\vec{\mathcal{T}}$ and the parameter of lever-arm $\vec{\mathcal{O}}$. This ambiguity can be avoided by introducing at least one external measurement. A ground control point equation should be added and the system to minimize can be written as follows:

$$\begin{cases} \cdots\cdots \\ \vec{\mathcal{G}_k}|_t - \mu \cdot \mathcal{R} \cdot \vec{\mathcal{C}_k}|_r - \vec{\mathcal{T}} - \mathcal{R} \cdot \mathcal{R}_k^T \cdot \vec{\mathcal{O}} = \vec{0} \\ \cdots\cdots \\ \vec{\mathcal{P}_i}|_t - \mu \cdot \mathcal{R} \cdot \vec{\mathcal{P}_i}|_r - \vec{\mathcal{T}} = \vec{0} \\ \cdots\cdots \end{cases} \tag{4.5}$$

where: $\vec{\mathcal{P}_i}|_t$ = ground control point expressed in absolute frame;
$\vec{\mathcal{P}_i}|_r$ = ground control point expressed in relative frame.

The equations for ground control points behave as constraint equations during the minimization. To illustrate, a calibration data set with 17 ground control points is used and is described in Section 4.4. Figure 4.2 shows the variation of the lever-arm estimated value according to the number of ground control points used during the minimization.

The variation of the estimated value is wide, of about of 6 cm once a ground control point is introduced. The curves converge, increasing the number of ground control points used. Beyond 5 points, the variation of the estimate value is at millimeter level.

In order to study the quality of the estimation of the spatial offset in a self-calibration strategy, we can study the level of correlation between this

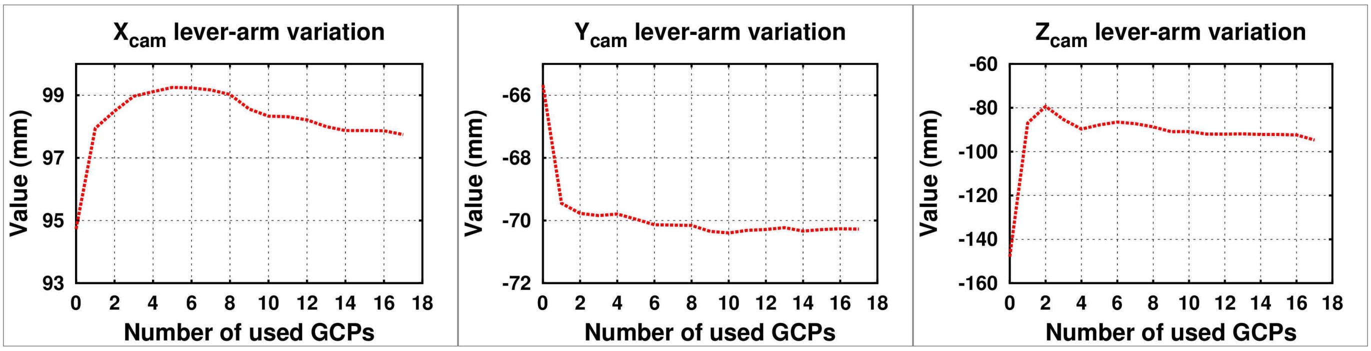

Figure 4.2: Variation of lever-arm estimation value per number of used `GCPs`

parameter and internal parameters, specially focal length and principal point. These values are given in Table 4.1.

$\mathcal{O}_x$	1.000					
$\mathcal{O}_y$	0.085	1.00				
$\mathcal{O}_z$	0.351	-0.628	1.00			
$\mathcal{F}$	0.22	-0.485	0.791	1.00		
$\mathcal{PP}_x$	0.837	0.000	-0.216	-0.279	1.00	
$\mathcal{PP}_y$	0.046	-0.827	0.488	0.602	-0.043	1.00

Table 4.1: Correlation values between lever-arm, focal and principal point parameters

These values show as expected that the correlations between these parameters are very strong. In particular, the planimetric components of the lever-arm are correlated with the principal point and the vertical component with the focal parameter, in the order of 80 %. This shows that this method has certain limits for the robust estimation of all calibration parameters simultaneously. To improve lever-arm estimation by self-calibration strategy, the addition of oblique images as well as images at different heights can significantly improve the quality of estimation by reducing the correlation between these parameters. Another method to improve lever-arm determination is to estimate a pre-calibration value of this vector according to an instrumental measurement methods. One of these methods based only on photogrammetric measurements is proposed below.

4.2.2.2 Pseudo-materialization method

Phase and optical centers cannot be directly measured. This calibration method is to make a pseudo-materialization of them. The idea is to determine their relative position with respect to a network of known points on the `GPS` receiver and the camera in a local frame. Figure 4.3 shows targets fitted to sensors.

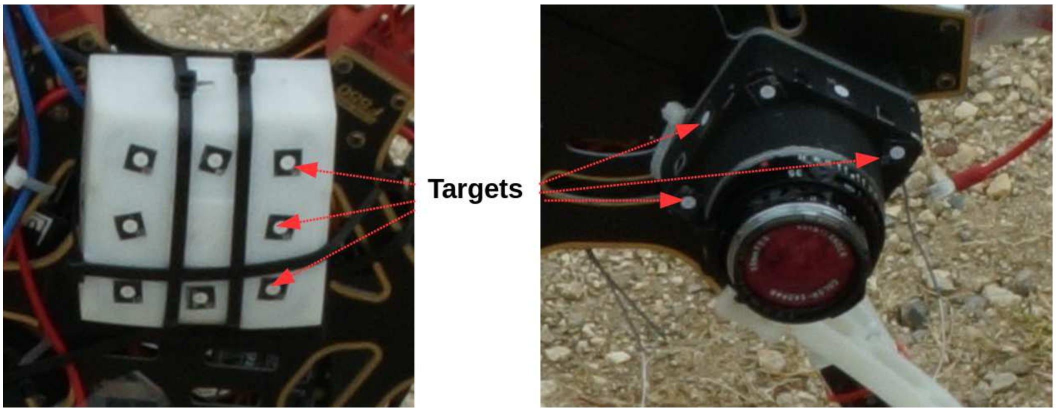

Figure 4.3: Targets on sensors: the `GéoCube` (left) and `CamLight` (right)

The acquisition of the calibration data protocol, which is carried out only once, is based on the following photogrammetric measurements:

1. Camera optical center calibration:
    - a photogrammetric acquisition is performed using the camera to calibrate
    - the camera to calibrate is positioned on a stable surface
    - the camera to calibrate takes a single image when positioned on the stable surface
    - a second camera performs a photogrammetric acquisition around the first one

    Figure 4.4 shows a photogrammetric acquisition around the camera to be calibrated while positioned on a stable surface.

2. `GPS` antenna phase center calibration:

Figure 4.4: Photogrammetric acquisition around the `UAV` on-board camera

- the `GPS` receiver is positioned on a scene that contains already known targets in an absolute reference system
- for each `GPS` observations session, a photogrammetric acquisition is performed
- the `GPS` receiver performs a rotation of about 90° rotation and a new session is started, coupled to a new photogrammetric acquisition

Figure 4.5 shows a photogrammetric acquisition of the `GPS` receiver for a given position.

Figure 4.5: Photogrammetric acquisition of the `UAV`'s on-board `GPS` receiver

4.2.2.2.1 Camera optical center calibration As a result of the data acquisition stage, we have taken two converging photogrammetric acquisitions of the same scene. The first was done with the camera to be calibrated and the second one performed with another camera around the first. A ruler is placed on the scene because the results of cameras poses estimation must be expressed in a scaled frame. A convergent acquisition, in the form of a circle, is the most suitable to ensure high overlap rates. Figure 4.6 shows images acquisition geometry.

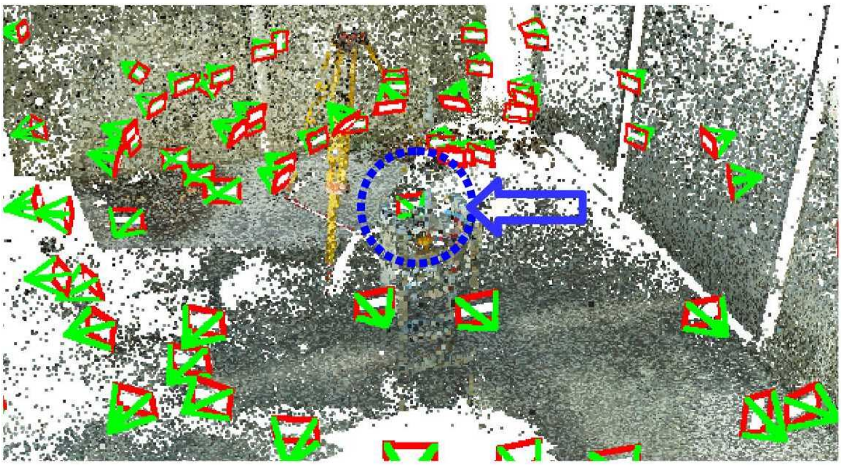

Figure 4.6: The circular acquisition geometry for camera optical center calibration

After performing the bundle block adjustment, the targets $\vec{p}_i|_k$ located on the camera (Figure 4.3) to be calibrated are measured in the images k and their $3d$ coordinates $\vec{P}_i$ estimated by pseudo-intersection. This estimate is carried out by a least square adjustment using system of equation 4.1.

Using the external parameters of the single image s (image with blue circle on Figure 4.4) acquired by the camera to be calibrated while placed on the stable surface, the $3d$ targets positions $\vec{P}_i|_r$ are expressed in the camera frame $\vec{P}_i|_{cam}$ using:

$$\vec{P}_i|_{cam} = \mathcal{R}_s^T \cdot (\vec{P}_i|_r - \vec{\mathcal{C}}_s|_r) \tag{4.6}$$

where:

- $\vec{P}_i|_{cam}$ position of target i expressed in the camera frame
- $\vec{\mathcal{C}}_s|_r, \mathcal{R}_s$ position and orientation of image s expressed in the relative frame
- $\vec{P}_i|_r$ previous estimated $3d$ position of target i expressed in the relative frame

4.2.2.2.2 GPS antenna phase center calibration The calibration of the `GPS` antenna phase center is based on the same principle. Here, we need to express the targets in an absolute reference frame. Photogrammetric acquisitions are performed on a scene where known targets are installed in the same system determined with topometric measurements.

We perform 4 rotations of about 90° to highlight the relative displacement of the antenna phase center position expressed in the local frame of the receiver. For each rotation, three hours of `GPS` raw observations sampled at 1 Hz are recorded. `RTKlib` is used to perform differential static post-processing of L1 carrier-phase measurements. Each session gives an estimate of the `GPS` antenna phase center position. For each rotation, a photogrammetric acquisition is performed. Figure 4.7 shows image acquisition geometry.

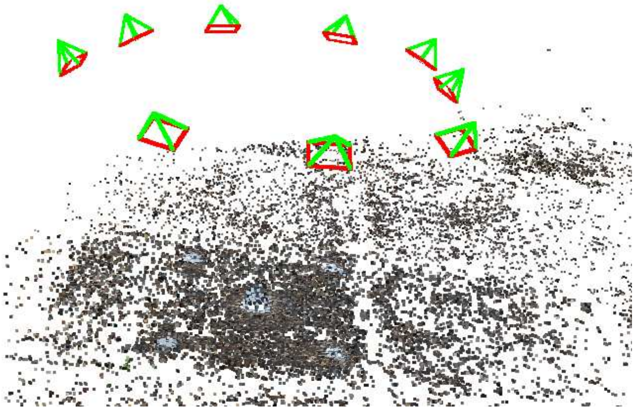

Figure 4.7: Images acquired around the `GPS` receiver for antenna phase center calibration

The estimated camera poses from bundle block adjustment are expressed in the `GPS` absolute reference system using four `GCPs`. The targets $\vec{g_i}|_k$ located on the `GPS` receiver 4.3 are measured in the images k and their $3d$ coordinates $\vec{G_i}$ estimated using system of equations 4.1. Targets positions and the position of the antenna phase center after the first session of measurements are arbitrarily considered as a reference state. Successive positions are expressed in the frame of the first session by estimating the 6 parameters $(R_i, \vec{T_i})$ of the rigid transformation $\mathcal{D}_i$ such that:

$$\mathcal{D}_i(\vec{P_i}) = \vec{P_0} \tag{4.7}$$

where:

- $\vec{P_i}$ position of targets and antenna phase center after session of observations i
- $\vec{P_0}$ position of targets and antenna phase center after the first session of observations

Figure 4.8 shows the planimetric displacement of the antenna phase center expressed in the frame of the first session of observations.

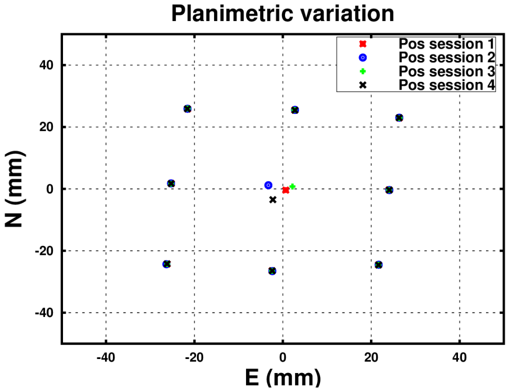

Figure 4.8: Planimetric variation of the antenna phase center

Symbols at the center of Figure 4.8 represent the predictions of the antenna phase center for each session. The mean deviation between all sessions is 0.7 *cm* and the maximum deviation is 1.1 *cm*. Final values for the calibration of targets and antenna phase center positions are the average of estimated positions including all observations sessions.

4.2.2.2.3 Computing lever-arm offset value To get the value of the lever-arm vector after the calibration of optical and phase centers are performed, it is necessary to conduct a photogrammetric acquisition of the `UAV`, with the sensors mounted, before take-off. Figure 4.9 shows images and geometry acquisition of the `UAV` on the ground.

To calculate the lever-arm offset value, only image measurements are needed. Let N be the number of targets measured on the camera and N' the number of targets measured on the `GPS` receiver. Let:

- $\vec{v}|_{R_r} = [\vec{P_1}|_r, \dots, \vec{P_N}|_r]$ camera targets estimated positions in the bundle block adjustment relative frame

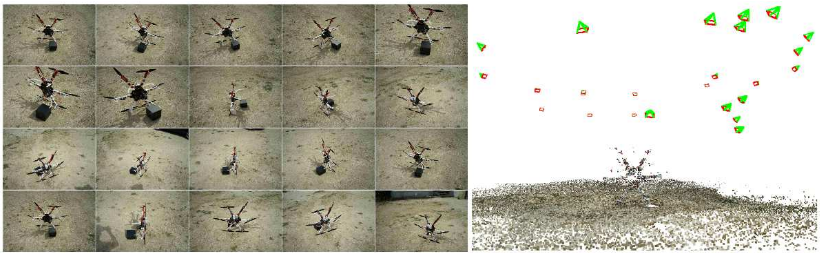

Figure 4.9: Photogrammetric acquisition around `UAV` before take-off (left) and image geometry acquisition (right)

- $\vec{v}|_{R_{cam}} = [\vec{P}_1|_{cam}, \ \dots \ , \vec{P}_N|_{cam}]$ camera targets estimated positions from calibration expressed in the camera frame
- $\vec{v'}|_{R_r} = [\vec{G}_1|_r, \ \dots \ , \vec{G}_{N'}|_r]$ `GPS` targets estimated positions in the bundle block adjustment relative frame
- $\vec{v'}|_{R_l} = [\vec{G}_1|_l, \ \dots \ , \vec{G}_{N'}|_l]$ `GPS` targets estimated positions from calibration expressed in the `GPS` receiver local frame
- $\vec{v'}|_{R_c} = [\vec{G}_1|_c, \ \dots \ , \vec{G}_{N'}|_c]$ `GPS` targets estimated positions expressed in the camera frame
- $\vec{C}_{gps}|_{R_l}$ antenna phase center from calibration expressed in the `GPS` receiver local frame
- $\vec{O}$ lever-arm vector by definition expressed in the camera frame

To estimate the value of the lever-arm offset $\vec{O}$, we have to:

1. estimate the 7 parameters $(\lambda, R_1, \vec{T_1})$ of the $3d$ similarity $\mathcal{S}$ such that camera poses are expressed in the calibrated camera frame:
$$\mathcal{S}(\vec{v}|_{R_r}) = \lambda \cdot R_1 \cdot \vec{v}|_{R_{cam}} + \vec{T_1} \tag{4.8}$$
2. express `GPS` targets in the camera frame:
$$\vec{v'}|_{R_c} = \mathcal{S}(\vec{v'}|_{R_r}) \tag{4.9}$$
3. estimate the 6 parameters $(R_2, \vec{T_2})$ of the rigid transformation $\mathcal{D}_i$ such that:
$$\mathcal{D}(\vec{v'}|_{R_l}) = R_2 \cdot \vec{v'}|_{R_c} + \vec{T_2} \tag{4.10}$$
4. express the lever-arm offset value as:
$$\vec{O} = R_2 \cdot \vec{C}_{gps}|_{R_l} + \vec{T_2} \tag{4.11}$$

4.2.2.2.4 Results A data acquisition has been made. Two photogrammetric acquisitions are performed as shown in Figure 4.9. The first one before the `UAV` take-off and the second one after it has landed. Each acquisition provides a lever-arm value with respect to pseudo-materialization methodology and allows us to control at least the mechanical stability from the start of the acquisition to its end.

Before comparing the values of the lever-arm vector provided by this method and the one obtained by the classical in-flight self-calibration method based on `GCPs`, we can compare the calculated values before the `UAV` takes off and after the `UAV` has landed. Table 4.2 gives lever-arm values for both measurements from two photogrammetric acquisitions of the `UAV` on the ground and the in-flight estimated value using all available `GCPs` (17) during this experiment.

Method	X_c (mm)	Y_c (mm)	Z_c (mm)
Before `UAV` take-off	86	-52	-82
After `UAV` landing	85	-51	-81
In-flight calibration	98	-70	-91

Table 4.2: Different estimates of values of the lever-arm offset

Both photogrammetric acquisitions of the `UAV` give two lever-arm values within 2 mm difference. Firstly, it proves that the mechanical assembly is stable and the sensors keep a fixed relative positions while the difference between the two calibration techniques (self-calibration method and pseudo-materialization method) is 26 mm and is more significant.

To study the impact of this difference a second flight is performed to get independent data sets. The first estimated lever-arm values given in Table 4.2 are used to correct the `GPS` post-processed trajectory to perform integrated sensor orientation based on `GPS` positions. Figure 4.10 shows residuals for exterior orientation positions determined by `GPS` with the pre-calibrated lever-arm value.

Residuals for exterior orientation positions gives a standard deviation of $\sigma_{xy} = 9\ mm$ for planimetric components and of $\sigma_z = 12\ mm$ for vertical component. This gives a good quality indicator on the coherence of the `GPS` solution and the photogrammetric external orientation based on tie points with the constraint of pre-calibration lever-arm value.

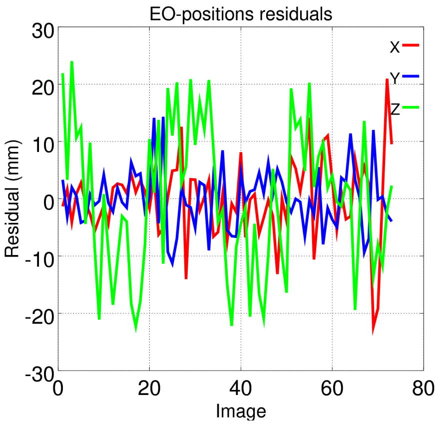

Figure 4.10: residuals of exterior orientation positions determined by `GPS` with the lever-arm pseudo-materialization method

In a second step, the residual on check points is calculated using estimated external orientation based on `GPS` positions as our purpose is to evaluate the accuracy of ground localization. Figure 4.11 gives a comparison of residuals computed on check points for each lever-arm calibration method.

Figure 4.11 shows that residuals are most important for the calibration method based on a photogrammetric acquisition of the `UAV` on the ground. Residuals for this method give an accuracy of 2 cm ± 1.4 cm while the in-flight calibration method gives an accuracy of 1.8 cm ± 0.8 cm. However, the second method requires `GCPs` and a stable mechanical mounting of sensors on the `UAV` to be reused whereas the first one needs only image measurements and requires no special mechanical configuration.

4.2.2.3 Conclusion

Here, we propose a study of a method for estimating the spatial offset in the context of integrated sensor orientation of a close-range photogrammetric acquisition performed with a `UAV`. The proposed method is flexible because it requires no mechanical constraint for the mounting of the sensors on the `UAV` on each flight. Once the optical and antenna phase centers calibrated, the estimation of the lever-arm value is based solely on photogrammetric measurements based on a stereoscopic acquisition of the `UAV` on the ground before `UAV` take-off or after `UAV` landing. It is even recommended to perform the two acquisitions in order to control the stability of the sensors. During our experiments, we achieved an absolute accuracy of 2 cm ± 1.4 cm on check points

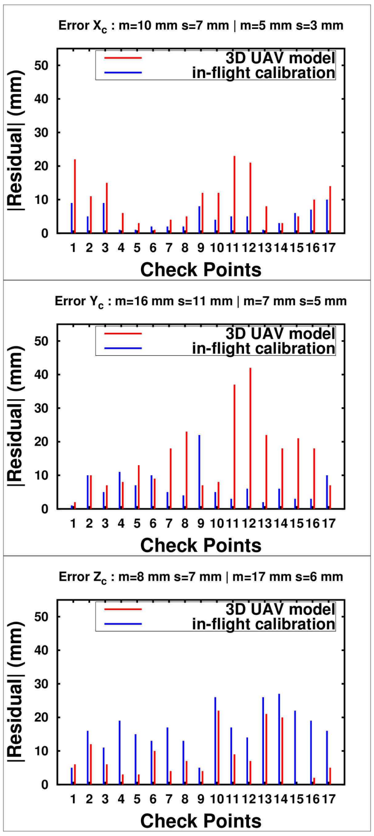

Figure 4.11: Comparison of absolute residuals using two different lever-arm calibration techniques

using the pseudo-materialization method whereas the classical in-flight one achieved an absolute accuracy of $1.8\ cm \pm 0.8\ cm$. Nevertheless, this second method requires external measurements (`GCPs`) and that the mechanical configuration remains the same from one flight to another so that it remains valid.

This result does not allow us to conclude about the accuracy achieved by the pseudo-materialization method. Indeed, this method theoretically allows a determination of about less than one centimeter of the lever-arm vector [Vallet & Skaloud 2004]. The statistical results of the differences on the control points between the two techniques is in the measurement noise ($\sim$ 2 mm). Further experiments must be conducted in different configurations and with more accurate ground truth data (for example by performing a `GCP` field survey by topometric measurements instead of `GNSS` `RTK` measurements). The determination of the phase center of the `GPS` antenna must also be improved. Indeed, the determination with our photogrammetric method shows a range of variation of the phase center of 1.1 cm over 4 different observation sessions. The determination of the phase center with respect to the `ARP` of the antenna is replaced by a network of targets materialized on the waterproof case which includes the `GPS` module and the antenna. This does not affect in any way the determination of the phase center. Finally, the duration of the observations of the carrier-phase data can be increased.

The analysis of the residuals of Figure 4.11 shows that the determination of the vertical component is more accurate for the pseudo-materialization method than for the in-flight estimation method. In contrast, the classical method shows a better determination of the planimetric components of the spatial offset. This is due to the fact that the `UAV` changes orientation at each flight line which has the effect of reducing the correlation between the planimetric components of the lever arm and the principal point which leads to a better determination.

4.2.3 Synchronization Issue

Ensuring the same time-scale is crucial when using various data sources [Rehak & Skaloud 2017b]. Time synchronization between `GPS` measurements and images taken by the camera can be neglected if we have, for example, a high sampling of `GPS` data which allows the use of interpolation techniques. To achieve the best time synchronization, we opted for a camera-triggering controlled by a `GPS`. **`U-blox TimePulse`** signal feature provides clock pulses with configurable duration [u-blox 2016].The constraint of this feature is that the interval between pulses should be an integer multiple so that the pulse is aligned with the `TOW`.

During our first experiments, we chose the `Sony-RX1` camera model. Although this camera is not the one used in the following experiments, we present the synchronization aspect using a commercial camera. We show that this type of cameras is not adapted to perform sensor synchronization, although it is possible to correct this error by modifying the model that links observations. The `Sony-RX1` is a professional full-frame 24 Mpx compact camera. The lens has a fixed focal of 35 mm. The optical quality of this lens is very honorable making the `Sony-RX1` a good commercial photogrammetric camera. However, there are a few disadvantages: no interchangeable optical lens capability and the camera is quite heavy (482 g), which is not suitable for a small `UAV` with relatively little flight autonomy. In addition, this camera is not cheap as it costs about €2500. Thanks to `LOEMI` team the `Sony-RX1` camera was customized to achieve `GPS` triggering.

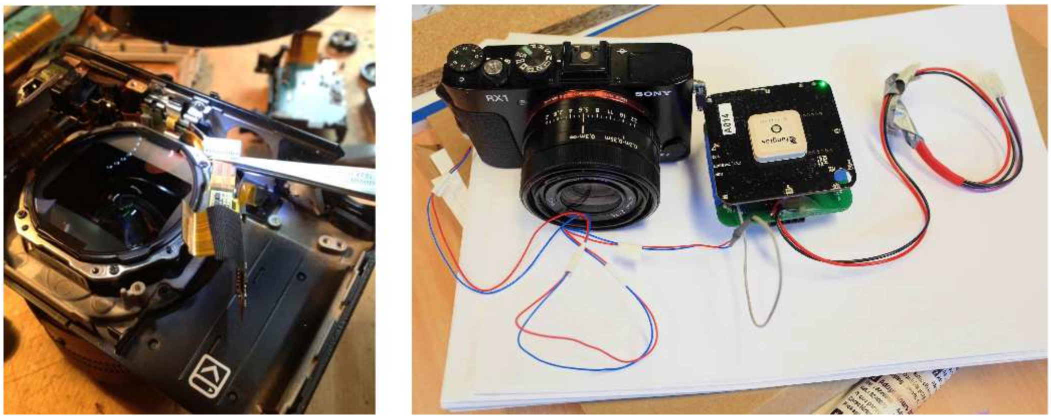

Figure 4.12: Adapting Sony-RX1 camera triggering to GPS module TimePulse feature

A first measurement of the electronic delay was achieved in the laboratory. The measurement was carried out with an oscilloscope that shows both the waveform of the two electrical signals from the GPS pulse that triggers the camera and the outbreak of the camera. Camera-trigging on the Sony-RX1 is considered as perfectly synchronized with the flash carrier whereas the measurement is performed on the CMOS pin control on IGN's light camera.

Figure 4.14 reports the pattern of the two signals. The red curve corresponds to the GPS pulse whose rising edge starts taking pictures with a delay of 0.4 *ms* on the falling edge of the flash pulse for the first camera and 64 *ms* for the second one.

This measurement highlights the existence of an electronic delay between the two sensors, however, it does not prove that this value is steady over time and can be considered as constant and permanent bias. Given the complexity of the measurement using an oscilloscope, another solution has allowed to describe the reproducibility of the electronic delay. The TimeMark feature in the u-blox GPS module is used to date events on the GPS's time-scale. Both cameras were adapted to recover the electronic pulse corresponding to the start of the exposure. Two events are dated: the TimePulse sent by the GPS to trigger the camera which is aligned to TOW and the *TimeMark* dated by the GPS, that is the actual trigger of the camera. The difference in time between these two events is exactly the electronic delay and is equivalent to our measurement performed in the laboratory with an oscilloscope. Figure

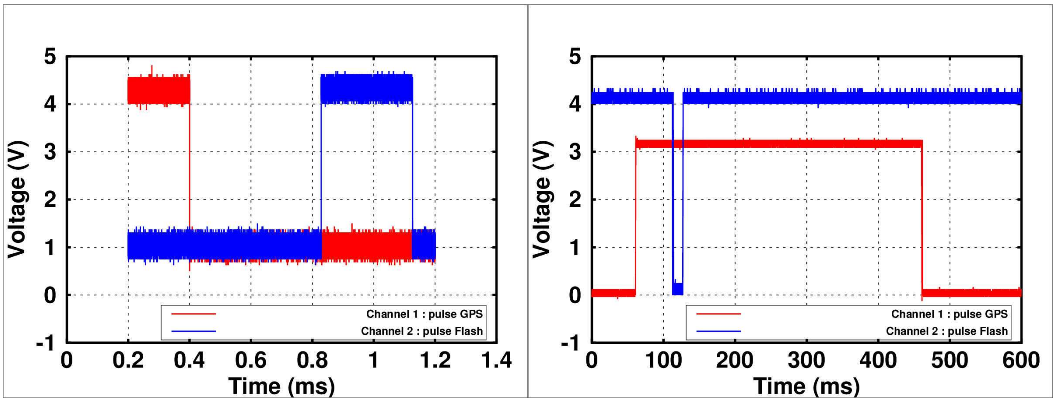

Figure 4.13: Measurement of electronic delay with an oscilloscope: between `GPS` and `IGN` light camera (left) and `Sony-RX1` (right)

(4.14) shows the reproducibility of the measurement of the delay.

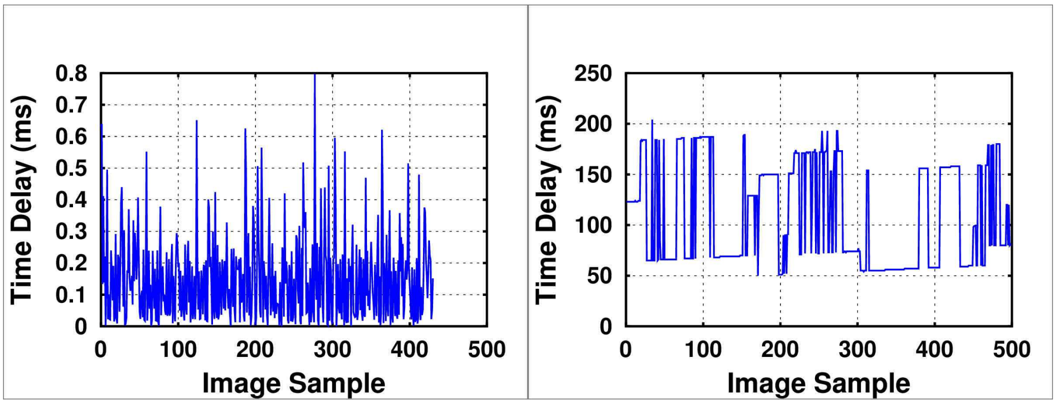

Figure 4.14: Measurements of electronic delay stability with time difference pulses: `IGN` light camera (left) and `SONY-RX1` (right)

For the camera manufactured internally, the electronic delay value is very stable over time. For each triggering of the camera the value is less than 1 ms, which represents a maximum error of 5 mm on the position at a typical `UAV` speed of 5 m/s. As for the `Sony-RX1` commercial camera, the value is unstable and changes over time, between 50 and 200 ms, which represents a maximum error of 1 m at the same speed.

In conclusion, even with the use of a high-end commercial camera, time synchronization remains a difficult problem to handle because standard cameras are not built to be used in such a context. The development of a home-made `UAV`-metric camera provides solutions to this kind of problem. The current delay of ~ 0.4 ms, managed by the camera's software, has been improved to ~ 200 ns and managed by the hardware. The goal is to make it very negligible in any configuration of use of the camera (multi-rotors or fixed-wing `UAVs`).

If it is impossible to achieve perfect time synchronization, for instance with the use of a commercial camera, and if the sampling of the `GPS` trajectory is not dense enough, it is possible to correct the electronic delay if measurements of instantaneous velocity of the `UAV` are available adopting a spatio-temporal aerial control model [Blázquez 2008]. In our case, the `u-blox GPS` receiver provides direct access to instantaneous velocities expressed in `ECEF` frame. If raw data of Doppler measurements are recorded by the `GPS` receiver, then it is possible to deduce instantaneous velocity values [Chalko 2007]. As a consequence a correction is added to the system of equations (4.4) in both cases, delay is stable [Blázquez & Colomina 2012] or variable and can be written as follows for an image k:

$$\begin{cases} \quad\quad\quad\quad\quad\quad \cdots\cdots \\ \vec{\mathcal{G}_k}|_t - \mathcal{S}(\vec{\mathcal{C}_k}|_r) - \mathcal{R}\cdot\mathcal{R}_k^T\cdot\vec{\mathcal{O}} - \vec{\mathcal{V}_k}|_t\cdot t_d = \vec{0} \\ \quad\quad\quad\quad\quad\quad || \\ \vec{\mathcal{G}_k}|_t - \mathcal{S}(\vec{\mathcal{C}_k}|_r) - \mathcal{R}\cdot\mathcal{R}_k^T\cdot\vec{\mathcal{O}} - \vec{\mathcal{V}_k}|_t\cdot t_d^k = \vec{0} \\ \quad\quad\quad\quad\quad\quad \cdots\cdots \end{cases} \tag{4.12}$$

where: $\mathcal{S}$ = $3D$ similarity application;
$\vec{\mathcal{V}_k}$ = instantaneous velocity of image k in absolute frame;
t_d = time delay parameter;
t_d^k = time delay parameter for image k.

An acquisition was performed using the `Sony-RX1` camera. This acquisition has 231 images and 10 ground control points. Images were acquired at a rate of 2 seconds. All ground control points were used to estimate parameters of system of equations (4.5) and (4.12). Figure 4.15 shows the residuals of the estimation assuming no electronic delay (10 parameters estimated) and variable delay (242 parameters estimated).

Taking electronic delay into account, as shown by the measurements in Figure 4.14, improves the relative accuracy between the two sensors by a factor of 12 for planimetric components, and by a factor of 4 for the vertical component. This error in the position largely impacts the planimetric axial components. Indeed, the flight controller system allows the `UAV` to maintain a constant flight height based on a barometric sensor that makes vertical speeds very low and reduces synchronization error for this component.

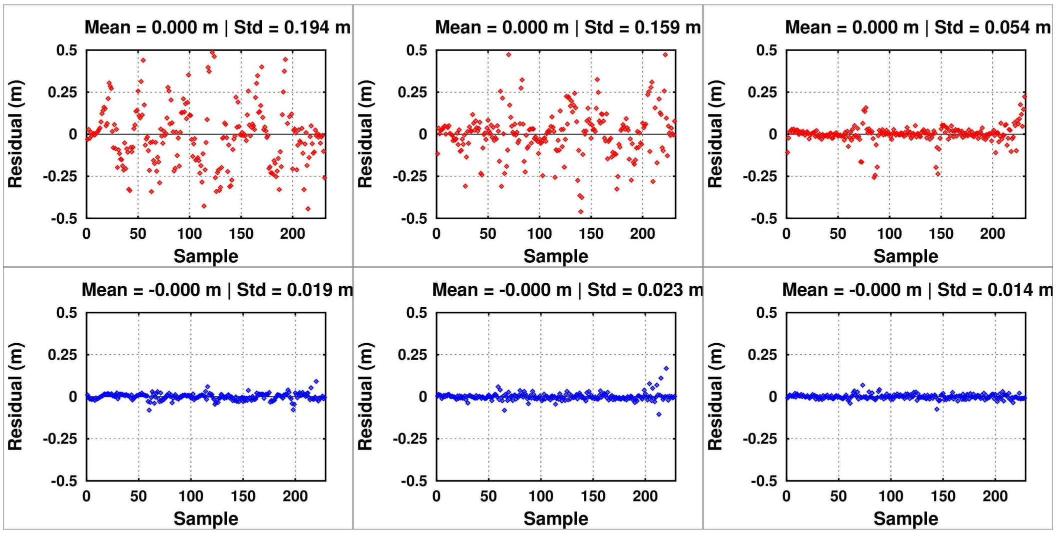

Figure 4.15: Comparison of residuals with and without taking delay into account. Planimetric components (left and center) and vertical component (right).

4.2.4 GPS positions & Camera Centers matching

When data acquisition with two different sensors is performed, it is common that the sampling frequencies are not equal. For aerial photogrammetric acquisitions, the maximum flight height allowed, longitudinal and lateral overlap values, and the desired `GSD` will impose the number of images and thus the optimal frame rate. In general, for a `UAV` acquisition, typical values vary in the range of an image every 2 to 5 seconds. On the other hand, the typical sampling frequency for `GPS` positioning is 1 Hz. So, there are two to five times more `GPS` positions than images acquired, including `GPS` data recorded during `UAV` take-off and landing. Figure 4.16 shows the result after processing both trajectories in their respective frames.

A common technique to identify corresponding `GPS` positions to camera centers is Geotagging images with approximate `GPS` positions determined

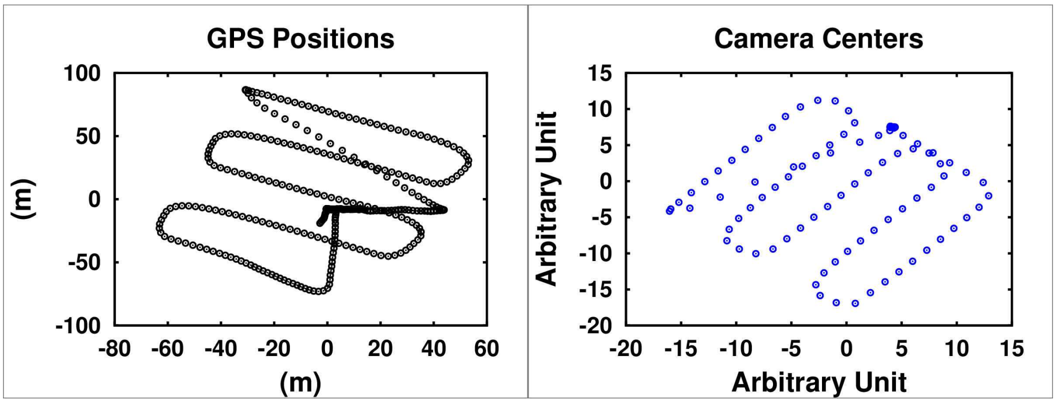

Figure 4.16: Trajectories in various frames with different sampling

on flight and based generally on `C/A` code observations. It is also possible to synchronize the internal clock of the camera with respect to the `GPS` time-scale. This second solution will be valid only if the internal clock of the camera is stable and does not drift. Another way is to date the triggering of the camera in the `GPS` time-scale. In our case the camera doesn't have an internal clock at this time and the system offers no possibility of Geotagging images.

After performing `GPS` processing data and relative exterior orientation, we get 2 trajectories expressed in different frames with different sampling. This technique of center matching may be useful for users of commercial cameras who cannot easily perform camera clock synchronization or images Geotagging. It may also be useful in the case where the interpolation of image position is not desired. Finally, it can also be used when the electronic delay of the camera is negligible and the triggering of the images is aligned with the `GPS TOW` for better synchronization accuracy. However, a constraint requires that the frequency should be constant for the entire duration of the acquisition. In this case, it is possible to identify the corresponding positions by computing all possible reasonable[1] combinations for all possible time offsets of successive ratios distances between image centers and a combination of `GPS` positions.

If a vector v contains n positions as $v = [\vec{P}_1, \ldots, \vec{P}_n]$, the vector $v^{'}$ of successive ratio distances will have $(n-1)$ size as $v^{'} = [r_1, \ldots, r_{n-1}]$,

---

[1] this means that the chronological order is respected using for example images names

where: $\vec{P}_i$ = camera center of image i;
$r_i = d(\vec{P}_i, \vec{P}_{i+1})/d(\vec{P}_i, \vec{P}_{i-1})$ current ratio of distances;
d = geometric distance.

Each time offset value, which is an integer multiple of a second and a possible combination that corresponds to the same length of camera centers vector, gives a curve of successive distances ratios of `GPS` positions which is compared to that of camera centers. The ratios are used because both the `GPS` absolute and the photogrammetric relative frames do not have the same geometric scale. The combination of an offset value which gives the maximum value of the correlation coefficient between the two curves gives the corresponding `GPS` positions to the camera centers. This method can be described as follows:

Algorithm 1 Matching `GPS` positions and Camera centers

input : GPS positions & Camera centers
output: Corresponding positions ⇔ centers

```
Compute($dcr$ = distances cameras ratios)
Compute($nbrMaxTO$ = maximum number of possible time offsets)
for $i \leftarrow 1$ to $nbrMaxTO$ do
    Compute($nbrMaxComb$ = maximum number of GPS trajectory combinaison)
    for $j \leftarrow 1$ to $nbrMaxComb$ do
        get(corresponding current GPS positions)
        Compute($djr_j$ = distances Gps ratios)
        Compute($c(i,j) = corr(dcr, djr_j)$)
    end
end
Compute($max(c)$)
```

Figure 4.17 illustrates the results of this method for a real dataset and gives results of maximum correlation coefficient for 3 values of time offset.

Values for all possible time offset between `GPS` positions and camera centers and a time offset combination gives the maximum possible value for the correlation coefficient between the curves of distances ratios. The greater the time offset between the two sensors is, the lower the number of combinations to be tested will be. This method has been tested on multiple datasets and a unique combination gives the maximum value of the correlation coefficient. This method qualifies the consistency between the relative displacements measured by each sensor and allows to match the measurements.

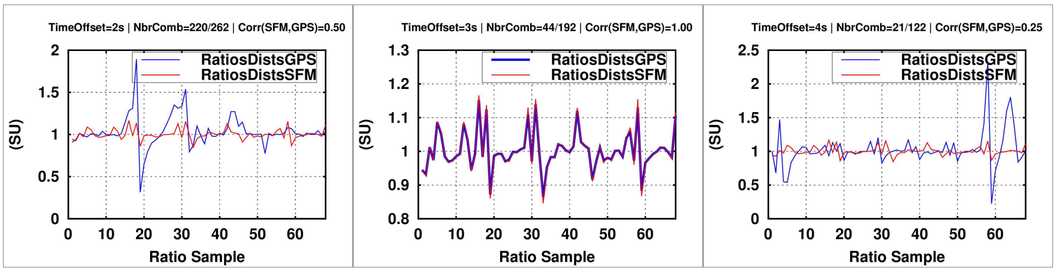

Figure 4.17: Correlation values between ratios distances curves after testing different temporal offset values

4.3 Data Fusion

An essential step to optimize the final accuracy of georeferencing process is to refine all parameters using all available observations in a bundle adjustment. The observations which can be used are tie points, `GPS` camera positions and, optionally, at least one ground control point if the lever-arm vector is unknown. This involves an estimate for N images of an acquisition, at least, $(6 \cdot N + 10)$ unknown parameters of the observation system assuming that the internal camera parameters are determined beforehand. `MicMac` photogrammetric suite also offers the opportunity to refine simultaneously the internal parameters of the camera which can improve the accuracy in case of a self-calibration bundle block adjustment based only on tie points. Figure 5.1 shows a summary of our processing chain. The latest (bundle block adjustment) step offers various coupling strategies which we will study below.

The same dataset of lever-arm calibration flight in part (4.2.2.1) is used. Five points are used as ground control points to calibrate the lever-arm vector, while the remaining 12 points are used as control measurements in order to qualify georeferencing accuracy. Table 4.3 provides statistical indicators of the gain in accuracy with the global compensation technique, assuming different strategies $[\![\mathcal{S}_1 : \mathcal{S}_5]\!]$.

Strategy $\mathcal{S}_1$ is a camera poses conversion from relative into absolute frame by estimating 10 parameters of the system of equations (4.5). Strategy $\mathcal{S}_2$ is a minimization of system of equations (4.5) and (4.1) through a bundle block adjustment where heterogeneous observations (tie points, `GPS` positions and `GCPs`) are used simultaneously. The parameters estimated here are the

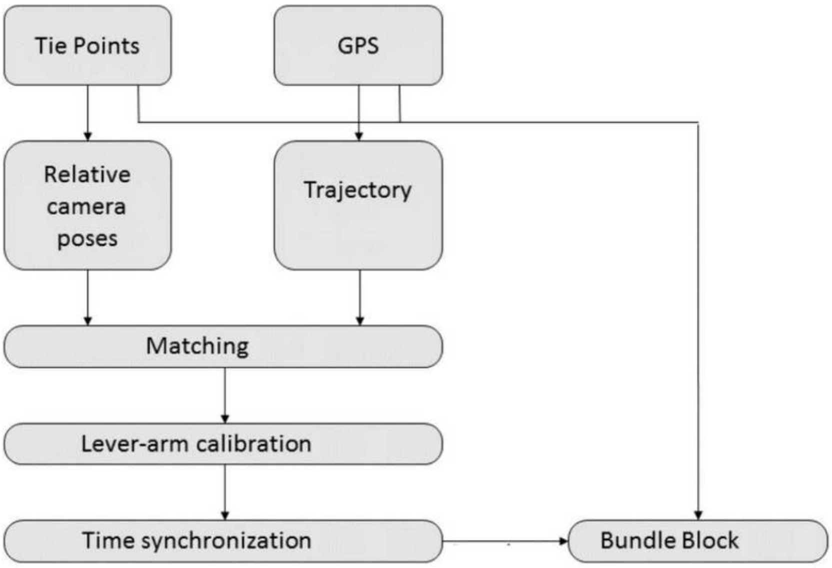

Figure 4.18: Data fusion processing workflow

parameters of $3D$ similarity and the position and orientation of each image. Strategy $\mathcal{S}_3$ introduces the lever-arm as a parameter to refine in the global compensation. Strategy $\mathcal{S}_4$ fixes the lever-arm while the camera model ζ of system of equations (4.5) is introduced as a parameter to refine. Strategy $\mathcal{S}_5 = \{\mathcal{S}_3 \cup \mathcal{S}_4\}$.

The lower residual obtained on check points is found by performing a global compensation with free internal parameters. However, the difference is very low when compared to a global compensation where only exterior parameters

	Estimated parameters				MAE (cm/px)	std (cm)
	Relative poses	Absolute Centers	Lever-arm	Camera model		
$\mathcal{S}_1$	(-)	(-)	(-)	(-)	2.4/2.0	0.8
$\mathcal{S}_2$	Tightly coupled		-	-	0.8/0.7	0.8
$\mathcal{S}_3$	Tightly coupled			-	0.8/0.7	0.8
$\mathcal{S}_4$	Tightly coupled		-	Tightly coupled	0.8/0.7	0.7
$\mathcal{S}_5$	Tightly coupled				0.8/0.7	0.8

Table 4.3: Residuals on check points depending on processing strategies

Table 4.4: Standard deviations of parameters for different strategies

	$\mathcal{S}_2$	$\mathcal{S}_3$	$\mathcal{S}_4$	$\mathcal{S}_5$
$\bar{\sigma}_{C_x}$ (m)	0.003	0.005	0.003	0.005
$\bar{\sigma}_{C_y}$ (m)	0.002	0.004	0.002	0.003
$\bar{\sigma}_{C_z}$ (m)	0.001	0.003	0.001	0.004
$\bar{\sigma}_{C_\omega}$ (°)	0.001	0.001	0.001	0.001
$\bar{\sigma}_{C_\phi}$ (°)	0.001	0.004	0.001	0.004
$\bar{\sigma}_{C_\kappa}$ (°)	0.001	0.003	0.001	0.003
σ_{O_x} (m)	-	0.002	-	0.003
σ_{O_y} (m)	-	0.001	-	0.003
σ_{O_z} (m)	-	0.004	-	0.041
σ_f (px)	-	-	0.27	0.75
σ_{PP_x} (px)	-	-	0.34	0.37
σ_{PP_y} (px)	-	-	0.35	0.39

are estimated again. This is a good indicator that the estimation of internal parameters by self-calibration gives a correct result using the strategy presented in (4.2.1) for this dataset. For the third strategy, estimating again the lever-arm value gives a variation of 3 *mm* in the norm of the vector that has a value of 15.0 *cm*. The last combination is a degenerate combination where the accuracy is still equivalent to other strategies but where the focal length and lever-arm estimation are wrong. In fact here, the variation of the lever-arm value is 7.4 *cm* and it impacts the vertical component by 95 %. This variation is compensated by a variation of 7 pixels of the focal length estimation, which still gives correct residuals on check points but incorrect parameter estimation. Indeed, in this configuration, the correlation between the focal length and the vertical component of the lever-arm vector makes the estimation of these two unknown parameters ambiguous.

In order to compare these different processing strategies, standard deviations of the estimated parameters can be discussed. Table (4.4) gives, for strategies with similar results ($\mathcal{S}_2$ to $\mathcal{S}_5$), the mean value of estimated standard deviation for external parameters, lever-arm vector, focal length and principal point. This table confirms that the $\mathcal{S}_5$ strategy gives an estimate with high uncertainty on the focal length (0.75 px) and the lever-arm offset (0.041 m), while the strategy that gives the lowest uncertainties is the $\mathcal{S}_4$ strategy. The final strategy adopted for data fusion of heterogeneous observations is the following: two successive compensations are performed to avoid degenerate configuration where the focal length is correlated with the vertical component of the lever-arm vector. Indeed, a first compensation is achieved by releasing the lever-arm to refine its estimate ($\mathcal{S}_3$), then the result is used as an input for a second compensation where, this time, the internal camera parameters are released to refine their estimates using not only tie points, but also external ground control points measurements ($\mathcal{S}_4$).

4.4 Experimental Data

This part will show the results of two `UAV` flights. The first flight is considered as a calibration flight and the second one is a flight used to qualify the repeatability of calibration parameters. The same flight plan is used to perform both flights based on `DJI Ground Station` software. Figure 4.19 (left) shows a screen-shot of the achieved flight plan. The flying height was set at 70 *m* for a `GSD` of 1 *cm*. Overlap parameters are 75%-35% and the surface covered is about 2 *ha*. Both flights are composed of a hundred images. The duration of each flight is less than 15 minutes. The scene has 17 ground control points whose coordinates were measured using a `GPS RTK` system.

The two images in Figure 4.19 (center and right) show the acquired images and the geometry of the acquisition. The monochromatic version of the camera is used. `GPS` positions are represented in blue, ground control points in yellow and check point in red.

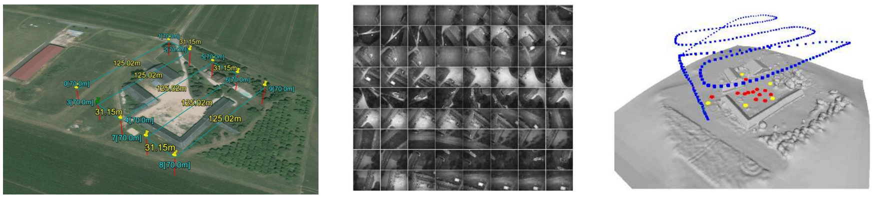

Figure 4.19: Flight plan (left), panel of images (center) and acquisition geometry (right)

4.4.1 Calibration flight

The first flight is used to calibrate all assumed parameters, constant from one acquisition to another, namely, internal parameters of the camera as well as lever-arm vector. It is assumed that the relative mounting of the sensors on the `UAV` is the same. Relative poses estimation based only on tie points gives an average residual of 0.26 px with more than 99% of extracted tie points used in the bundle. For this configuration electronic delay is considered as negligible. Table (4.5) gives residuals in available check points after parameters estimation using 5 ground control points used as a constraint for lever-arm estimation:

The accuracy[2] of the calibration procedure is estimated at 2σ level to: $\mu = 0.8 \pm 0.5\ cm$.

4.4.2 Second flight

The second flight is used, based on the previous calibration parameters, to evaluate the accuracy of the predictive ability of our system. The internal parameters and the lever-arm vector estimated during the previous flight (4.4.1) will be forced during data processing. The accuracy of georeferencing is evaluated through residuals in all available check points. Relative poses

---

[2] $\mu = \bar{x} \pm t \cdot \frac{s}{\sqrt{n}}$ where: $\bar{x} = ||\bar{\delta}_x^2 + \bar{\delta}_y^2 + \bar{\delta}_z^2||$, t = Student coefficient and n = size of sample

Nom Pt	δx (cm)	δy (cm)	δz (cm)	$\|\|\delta\|\|$ (cm)
Pt_1	-0.2	0.8	-0.3	0.9
Pt_2	0.2	0.5	0.4	0.6
Pt_3	0.4	0.3	0.3	0.6
Pt_4	-0.1	0.4	0.5	0.7
Pt_5	0.5	0.6	0.1	0.8
Pt_6	-0.5	1.0	1.5	1.9
Pt_7	-0.1	0.5	-0.2	0.6
Pt_8	0.0	0.4	1.6	1.6
Pt_9	0.0	0.1	1.8	1.8
Pt_{10}	0.0	0.1	0.3	0.3
Pt_{11}	-0.2	0.5	0.3	0.7
Pt_{12}	-0.1	-0.1	-0.2	0.2
MAE	0.2	0.5	0.6	0.8
s	0.3	0.3	0.7	0.8

Table 4.5: Residuals on check points for fligh calibration parameters

estimation based only on tie points, with the camera's internal parameters frozen, gives an average residual of 0.30 px with 98 % of extracted tie points used in the bundle. Table 4.6 shows residuals in available check points after correction of `GPS` estimated positions of lever-arm calibrated value:

The accuracy performed by our coupled system after performing a flight calibration is estimated at 2σ level to: $\mu = 2.0 \pm 0.5$ cm. Adding GCPs to the global compensation reduce the residuals on check points. For example, with the use of 1 `GCP`, the accuracy improves to 1.7 cm ± 0.4 cm while using 3 `GCPs` gives an accuracy of 1.0 cm ± 0.4.

4.4.3 GCPs Vs GPS

Quality control of final products is essential. In fact, the delivered results are orthoimages and computed `DSMs` expressed as a $3D$ point cloud. Check points allow us to control the accuracy of the georeferencing of camera poses but not that of the `DSM` calculated.

A conversion of relative cameras poses into absolute poses using all available ground measurements is performed. This set of orientations is considered as a reference parameters set. One of the techniques used to control the quality of the final product is to generate a dense reference point cloud which will be compared to the point cloud produced by a `GPS` integrated sensor orientation

Nom Pt	δx (cm)	δy (cm)	δz (cm)	$\|\|\delta\|\|$ (cm)
Pt_1	-0.7	0.3	-2.1	2.2
Pt_2	-1.4	-0.7	-1.7	2.3
Pt_3	-1.8	-0.2	-2.3	2.9
Pt_4	-1.1	-0.7	-1.1	1.7
Pt_5	-1.2	-0.4	-1.8	2.1
Pt_6	-1.0	-0.6	-1.7	2.1
Pt_7	-1.5	-0.2	-1.4	2.0
Pt_8	-1.0	-0.1	-1.7	2.0
Pt_9	-1.8	-1.7	-2.3	3.4
Pt_{10}	-1.1	-0.1	-0.2	1.1
Pt_{11}	-1.0	0.4	-1.1	1.6
Pt_{12}	-1.0	0.6	-1.3	1.7
Pt_{13}	-1.5	0.0	-0.6	1.6
Pt_{14}	-1.6	-0.4	-0.4	1.7
Pt_{15}	-1.7	-0.2	-1.1	2.1
Pt_{16}	-1.8	-0.1	-1.6	2.4
Pt_{17}	-2.0	-0.7	-1.9	2.8
MAE	1.4	0.4	1.4	2.0
s	0.4	0.5	0.6	0.9

Table 4.6: Residuals on check points for second flight

of camera poses. To perform this step, the module `MicMac`, based on a multi-scale and multi-resolution approach, is used to generate `DSMs` keeping the same parameters. Two point clouds are then compared, one generated with camera poses georeferenced based only on the embedded `GPS` data and the second one generated using camera poses georeferenced using all check points, computing Cloud-to-Mesh distances. This comparison is performed using `CloudCompare` [CloudCompare (version 2.6.0) [GPL software] 2016], a free open-source software for $3D$ point cloud and mesh processing. Figure 4.20 shows the result of the comparison between the two generated point clouds.

The result of the comparison gives a mean signed difference of 1.2 cm with a dispersion of 2.5 cm. The tendency is relatively of the same order of size as the control carried out on the quality of camera poses georeferencing. Point clouds comparison control is subject to matching errors, however, for many applications, mostly in earthworks, which is our case, the challenge is to identify the existence of potential bias on large surfaces. In general, the quality control of camera poses based on check points is a robust indicator of the

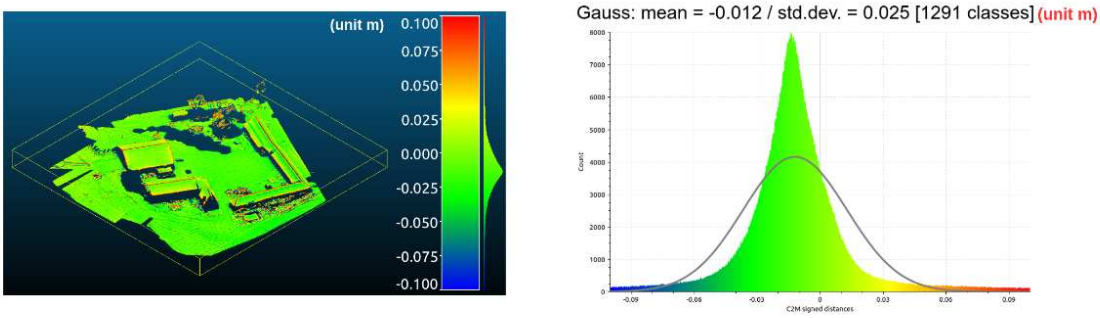

Figure 4.20: Comparison between both point clouds using `CloudCompare`

quality of absolute performed georeferencing.

4.5 Conclusion

In this Section we show that it is possible to perform direct sensor orientation of acquired images of a photogrammetric quality camera mounted on a `UAV` based only on a single-frequency `GPS` module. The hardware integration was performed in the laboratory, building home-made instruments based on available market sensors. This part in particular allowed us to control the geometric calibration aspect of our sensors as well as the time synchronization issue with our instruments. The system developed has also the singularity of being lightweight (2 kg) which makes it easy to transport. The accuracy achieved by our system is 2 cm ± 0.5 cm using 0 `GCP` based on calibration parameters (lever-arm offset and camera internal parameters) calculated on a first acquisition. The accuracy achieved using 1 `GCP` is 1.7 cm ± 0.4 cm while increasing the number of `GCPs` to 3 points gives an accuracy of 1.0 cm ± 0.4. These accuracy values our system achieved show that it meets the tolerances imposed in many mapping areas and makes it suitable to produce $3D$ models for metrological measurements applications where traditional techniques of surveying take time.

Chapter 5

Thermal deformation on images

Contents

5.1 Introduction 94

5.2 Algorithmic aspect 95

5.2.1 Image correlation 95

5.2.2 Thermal model 96

5.2.3 Space resection 97

5.2.4 Dataset processing workflow 99

5.3 Calibration experiments 99

5.3.1 2D Matching 99

5.3.2 Static space resection 106

5.3.3 Standard space resection 108

5.4 Experimental evaluation 110

5.4.1 Terrestrial photogrammetric acquisition 110

5.4.1.1 Standard configuration results 112

5.4.1.2 Single strip configuration results 114

5.4.2 Airborne photogrammetric acquisition 115

5.5 Conclusion 120

This chapter corresponds to:

- *[Daakir et al. 2017] M. Daakir, Y. Zhou, M. Pierrot-Deseilligny, C. Thom, O. Martin. Improvement of photogrammetric accuracy by modeling and correcting the thermal deformation on images. (submitted to ISPRS Journal of Photogrammetry and Remote Sensing on January 22, 2018).*

Abstract

This chapter presents a new method for improving the geometric accuracy of photogrammetric reconstruction by modeling and correcting the thermal effect of camera image sensor. The objective is to verify that the temperature of image sensor varies during the acquisition and image deformation induced by the temperature change is quantifiable, can be modeled and correctable. A temperature sensor integrated in the camera enables the measurement of image sensor temperature at the moment when one image is acquired. It is therefore natural and appropriate to take this effect into account and finally to model and to correct it after a calibration step. Nowadays, in cartography applications performed with `UAVs`, especially fixed wings, the frame rate of acquisitions is incredibly high. A high frame rate can result in an important temperature increase of the image sensor and thus a deformation in images. The correction of the above-mentioned effect can significantly improve the photogrammetric accuracy. We present three methods to calibrate this thermal effect and two datasets are carried out to verify the improvement in terms of the photogrammetric accuracy by taking into account this phenomena.

5.1 Introduction

Photogrammetry has undergone an unprecedented evolution in the past two decades. Its simplicity and efficiency make it an accessible and "low-cost" 3D modeling technique. Thus, thanks to its configurable accuracy, which only depends on the ground sampling distance of images, photogrammetry has become a staple technique for contactless metrological applications. Today, photogrammetry benefits from the development of cameras, the ever higher power of computers, the rise of aerial photogrammetry with `UAVs` and the multiplication of quasi-automatic software solutions to carry out data processing. However, the use of photogrammetry under metrological conditions requires total control of physical phenomena, such as: modeling of sensor internal geometry, the optical part of the apparatus and the condition of image acquisitions. With the continuous development of cameras, nowadays it is possible to obtain a temperature measurement of the sensor at the time when one image is taken.

When a camera is subjected to a variation of temperature, it undergoes a deformation which impacts internal parameters. In photogrammetry, it is recommended to use metric cameras of which internal parameters are stable during the acquisition. The quality of internal geometry modeling impacts directly the photogrammetric accuracy. If the assumption of stable internal parameters is not valid, it is possible, for instance, to estimate one camera calibration model for each image. However, this strategy is less accurate given the large number of parameters to estimate and strong correlations between internal and external parameters can lead to over-parametrization issues [Remondino & Fraser 2006]. If the camera deformation, which results in variation of internal parameters, is a deterministic function of temperature, and the temperature measurement of images is available, then it is possible to model and eventually to correct this thermal effect.

In this chapter we propose a new method for modeling the influence of thermal effect and correct this effect in order to improve the photogrammetric accuracy. Section 5.2 presents the algorithmic aspect of this study. In Section 5.3 different calibration experiments are carried out to highlight the thermal effect. Finally, Section 5.4 shows results obtained with experimental data to validate our approach.

5.2 Algorithmic aspect

In this section we will present the various algorithms used during the calibration process in Section 5.3.

5.2.1 Image correlation

Image correlation is a widely used technique for determining planimetric displacement between two images. In our case, images are supposed to be co-registered since the camera is supposed to be static. The movement in images introduced by the temperature variation is intrinsically 2 dimensional. Therefore, sub-pixel correlation is used to calculate the deformation on images induced by the temperature variation along planimetric components.

`MicMac`, a free open-source photogrammetric software correlator is used [Pierrot-Deseilligny & Paparoditis 2006]. This software allows to fine-tune sub-pixel correlation algorithm. In our case, the matching is performed on a scene which presents a two dimensional deformation of low amplitude. We adopt the parameters used in [Rosu *et al.* 2015] as the constraints are the same in terms of correlator parametrization. Moreover, the correlation problem here is easier because the diachrony effect is not presented. Table 5.1 gives values of parameters used for data processing.

Parameter	Value
Uncertainty on Parallax (px)	6
Discretization (px)	0.2
Correlation Threshold	0.5
Weight of correlation	2
Number of directions	7
Size of window	20

Table 5.1: Selected parameters for the correlator

The a priori uncertainty value on parallax specifies the two layers used to define the searching area. The value here is relatively high because it is twice the maximum value of expected deformation with a reasonable calculation time cost. The discretization is fixed at 0.2 px and corresponds to twice the target precision. The correlation threshold is set to 0.5. It means that values under this threshold have no influence. The higher the correlation weight, the closer the influence of the correlation score is to 1. Number of explored directions is set to 7 and is an empirical value. A lower value introduces anisotropic effect while a higher value leads generally to the same result but with a higher computation cost. The value of the window size is large because the pattern (Figure 5.3) has homogeneous areas and given the distance between the camera and the scene, this window size gives better correlation scores.

5.2.2 Thermal model

The displacement fields calculated by correlation then make it possible to estimate an analytical deformation model. Here, we choose to study a 4-parameter 2D spatial similarity as the analytical model. This model can be expressed as follows:

$$\begin{bmatrix} i_c \\ j_c \end{bmatrix} = \begin{bmatrix} T_i \\ T_j \end{bmatrix} + k \begin{bmatrix} cos(\theta) & -sin(\theta) \\ sin(\theta) & cos(\theta) \end{bmatrix} \times \begin{bmatrix} i_R \\ j_R \end{bmatrix} \tag{5.1}$$

where: $(i_T = c, j_c)$ = corrected image coordinates;
(T_i, T_j) = vector of translation;
k = scale factor;
θ = angle of rotation;
(i_R, j_R) = raw image coordinates.

This model is chosen since it allows to model variations of focal length as well as small rotational movements. It also allows to physically interpret the parameters. In practice the deformation is modeled by generic polynomials as they provide better accuracy.

The deformation due to thermal effect is assumed to be deterministic and is expected to be modeled as a function of temperature. For one image taken under a given temperature T, the deformation $\mathcal{M}_{T_0}^{T}(x, y)$ that the thermal effect introduces with respect to image of reference taken under T_0 is computed. As we cannot compute $\mathcal{M}_{T_0}^{T}(x, y)$ for all values of T, we estimate a deformation model from a set of computed deformations $(\mathcal{M}_{T_0}^{T_1}, \mathcal{M}_{T_0}^{T_2}, \cdots, \mathcal{M}_{T_0}^{T_N})$. The estimated deformation model is as follows:

$$\mathcal{M}_{T_0}^{T}(x, y) = \sum_{k=1}^{3} \sum_{i=1}^{4} \sum_{j=1}^{4} a_{k,i,j} T^k x^i y^j \tag{5.2}$$

Thereafter, a correction function to cancel out the deformation for any value of T is interpolated. This function is used to correct the image coordinates of extracted tie points and `GCP` image measurements in raw images as shown in Figure 5.1, which gives the general processing pipeline adopted for thermal deformation modeling.

5.2.3 Space resection

For the two experiments presented in Section 5.3.2 and 5.3.3 we use the space resection technique which, given a set of 3D terrain points and their corresponding 2D image projections, calculates the exact pose of an image. We assume that the internal model of the camera is known. In fact, we use here a pre-determined calibration model of which parameters (focal length and principal point) are subsequently re-estimated in a compensation (one focal length and one principal point per image in experiment 5.3.2, whereas one single value of focal length and principal point is estimated for each dataset in experiment 5.3.3).

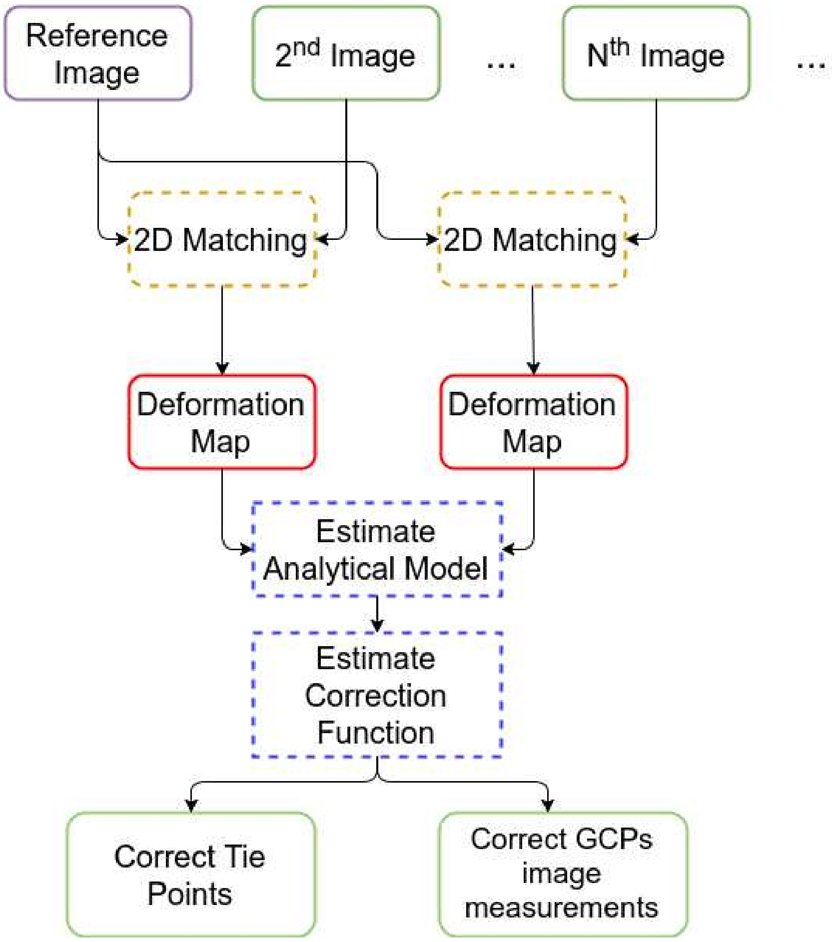

Figure 5.1: General pipeline for thermal deformation modeling

The equation system to be minimized for each image i can be written as follows:

$$I_l = \zeta(\pi(R_i(P_l - C_i))) \tag{5.3}$$

where:
I_l = $2d$ image position of `GCP` point l on image i (observation);
$\zeta = \mathbb{R}^2 \rightarrow \mathbb{R}^2$ application describing the camera model (not estimated);
$\pi = \mathbb{R}^3 \rightarrow \mathbb{R}^2$ projective application;
(R_i, C_i) = pose of image i (unknown);
P_l = $3d$ position of `GCP` l on image i (observation).

This formulation gives a fourth-degree equation and requires at least 3 points for pose estimation and 1 more point to remove the ambiguity. In general, we have much more than 4 points (in most cases, we have at least 20 `GCPs` in each image) to estimate the camera pose without ambiguity and to ensure the stability of the solution.

5.2.4 Dataset processing workflow

The processing of terrestrial and airborne photogrammetric datasets presented in sections 5.4.1 and 5.4.2 is also performed using `MicMac`. For each dataset, tie point extraction is performed with `SIFT` [Lowe 2004] algorithm and the `ANN` [Arya *et al.* 1998] algorithm is used for the matching of extracted tie points.

For the terrestrial dataset in section 5.4.1, the relative orientation between cameras is calculated based on tie points as observations with a self-calibration strategy [Fraser 1997]. A hybrid internal model is used coupling a high degree radial function (up to R^{15}) and a general polynomial one. `GCPs` are used to perform geo-referencing of the relative orientation and a bundle block adjustment is carried out by taking into account both tie points and ground control points as observations.

For the airborne dataset in section 5.4.2 a terrestrial convergent calibration is realized before the flight. The same bundle block self-calibration adjustment strategy is adopted. The pre-calibration permits to estimate 2 internal models, estimated based on raw observations and corrected one. These 2 internal models are during airborne data processing.

For all datasets, the photogrammetric accuracy is determined by the sum of residuals on `GCPs` and the gain in terms of precision for thermal deformation corrected images with respect to raw images is quantified by the improvement of this sum. Figure 5.2 shows our processing architecture.

5.3 Calibration experiments

In this chapter, we will present different calibration experiments for investigating image deformation due to the thermal effect.

5.3.1 2D Matching

Several acquisitions are performed on a textured wall. The main idea is to acquire image sequences with cameras fixed on a geodetic tripod. Two `CamLights` are used here for two types of acquisition. Type I acquisition consists in taking image sequences from the same point of view with an increase of camera temperature during the process. By exploiting images taken under

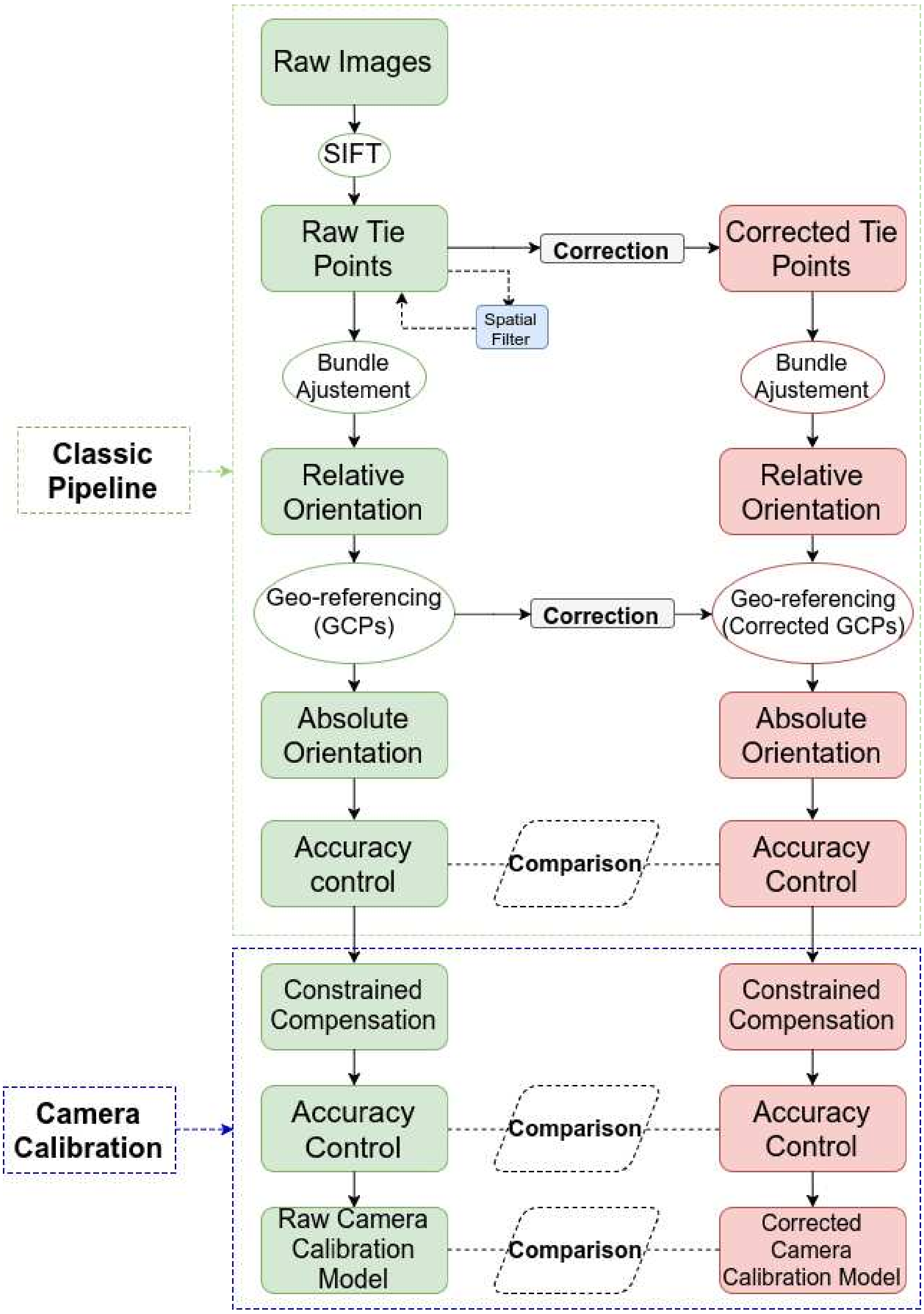

Figure 5.2: General workflow for data processing

different temperatures, the deformation due to the thermal effect can therefore be studied and eventually be modeled and corrected. Type II acquisition is performed with another `CamLight` whereas a peltier cooler is used as a temperature controller. “A peltier cooler is a solid-state active heat pump which transfers heat from one side of the device to the other, with consumption of electrical energy, depending on the direction of the current" [1]. The scene and the set-up of cameras and peltier cooler are as shown in Figure 5.3.

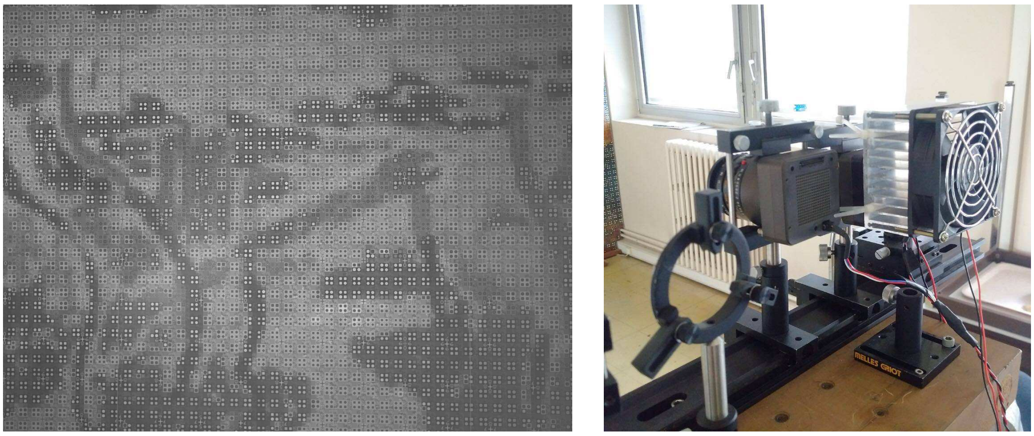

Figure 5.3: The scene of the textured wall (left) and the installation of cameras and peltier cooler (right)

Three type I acquisitions are performed, the first two are acquired successively on the same day with temperature rounding to an integer; the third acquisition is obtained on another day with temperature rounding to an increment of 0.3°C or 0.4°C. This setting is to study the influence of temperature precision on the quality of maps and to ensure that the deformation is stable over time. The frame rate is set to approximately 1 image every 4 seconds to get a significant increase of camera temperature.

For each acquisition, the first image is considered as the image of reference. The first step consists in generating deformation maps of the remaining images with respect to the image of reference. Figure 5.4 shows an example of the correlation map giving an indication of the matching quality between images and an example of a deformation map.

Type II acquisition is also completed. In this acquisition, we decrease the frame rate to 1 image per minute, with the cooling effect of the Peltier cooler, camera temperature varies within a small range. The temperature is rounded to an increment of 0.3°C or 0.4°C. Here we investigate two image couples; each image couple contains two images taken at the same temperature with a long time interval. A 2D deformation map per image couple is generated

---

[1] `https://en.wikipedia.org/wiki/Thermoelectric_cooling`

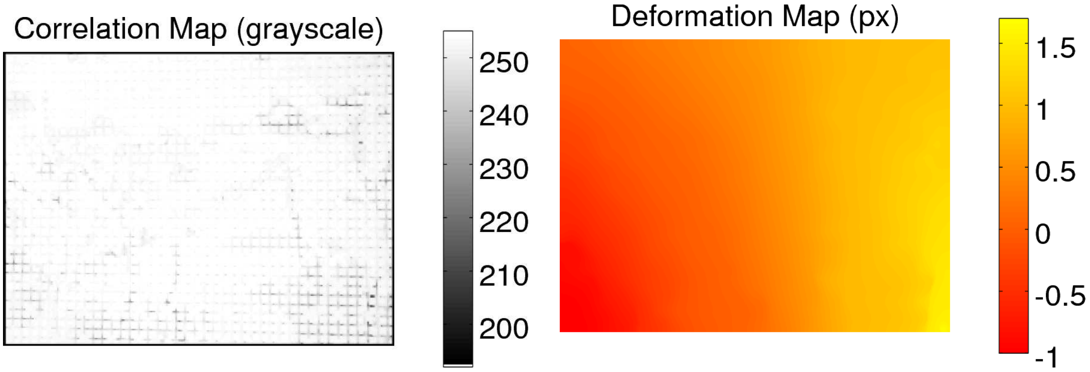

Figure 5.4: An example of a correlation map (left) and a 2D deformation map (right)

to verify if deformation occurs when images are taken under the same temperature.

Table 5.2 gives information on the 4 acquisitions; Figure 5.5 depicts the temperature variation of the 4 datasets. Table 5.3 gives information on investigated image couples of dataset 4.

	Type	Acquisition time (min)	Nb of images	Temperature range (°C)
Dataset 1	I	38	597	$[24, 49]$
Dataset 2	I	44	716	$[25, 50]$
Dataset 3	I	30	377	$[24.8, 56.2]$
Dataset 4	II	37	37	$[22.9, 23.6]$

Table 5.2: Information of 2D matching datasets

	Temperature (°C)	Time interval (min)
Couple 1	22.9	29
Couple 2	23.2	28

Table 5.3: Information of image couples

5.3.1.0.1 Results For each Type I acquisition performed on the textured wall, a 2D deformation map of one image can be calculated with respect to the reference image. The estimation is the result of 4 parameters: translations

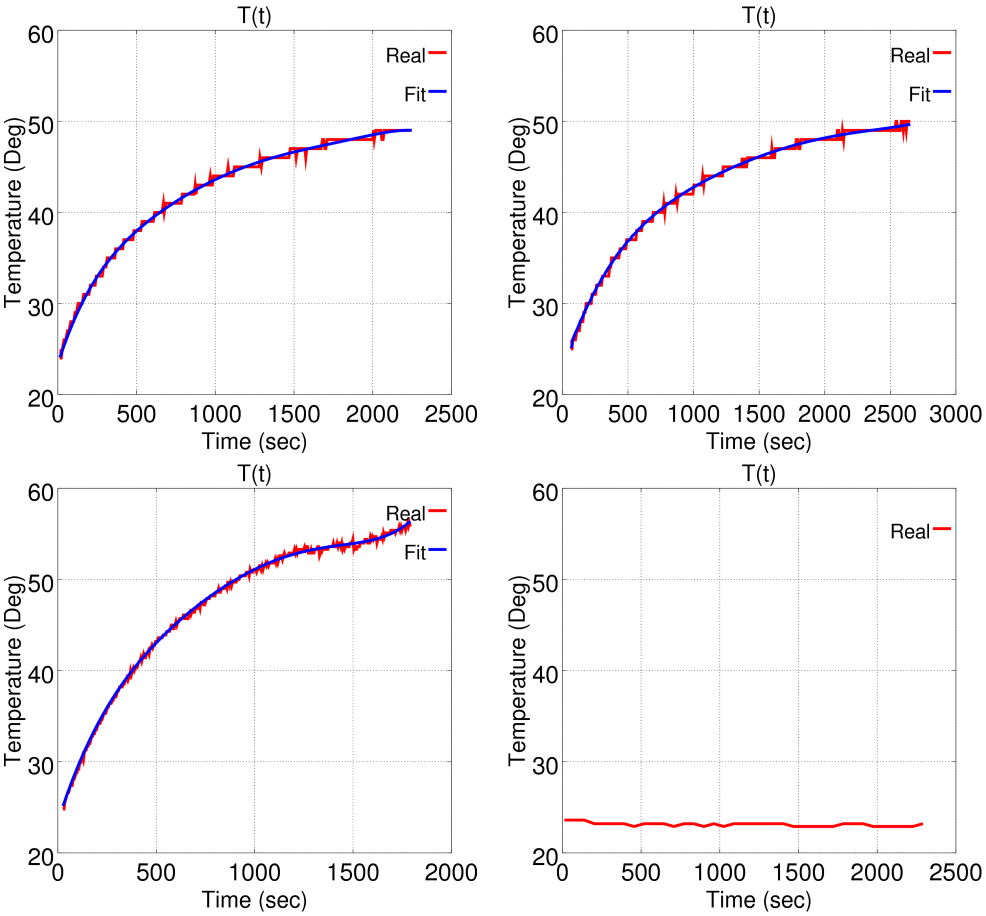

Figure 5.5: Temperature variation in Type I acquisition: dataset 1-4 (left to right, top to bottom)

T_x and T_y along axis x and y, rotation and scale factor are as shown in Figure 5.6-5.8.

From the above figures we can see that these 4 parameters all increase with temperature. The variation of translation corresponds to the deviation of principal point, the variation of the focal length and the rotation can be interpreted as the result of image sensor deformation caused by component dilatation as temperature changes. For dataset 1 and dataset 2 acquired on the same day, all the 4 parameters vary in the same way and a good repeatability of the thermal effect is observed. Dataset 3, acquired 4 months later, has a similar focal length variation; whereas, the variation of translation and rotation differ from dataset 1 and 2. For all 3 datasets, the variation of rotation remains insignificant during the acquisition (less

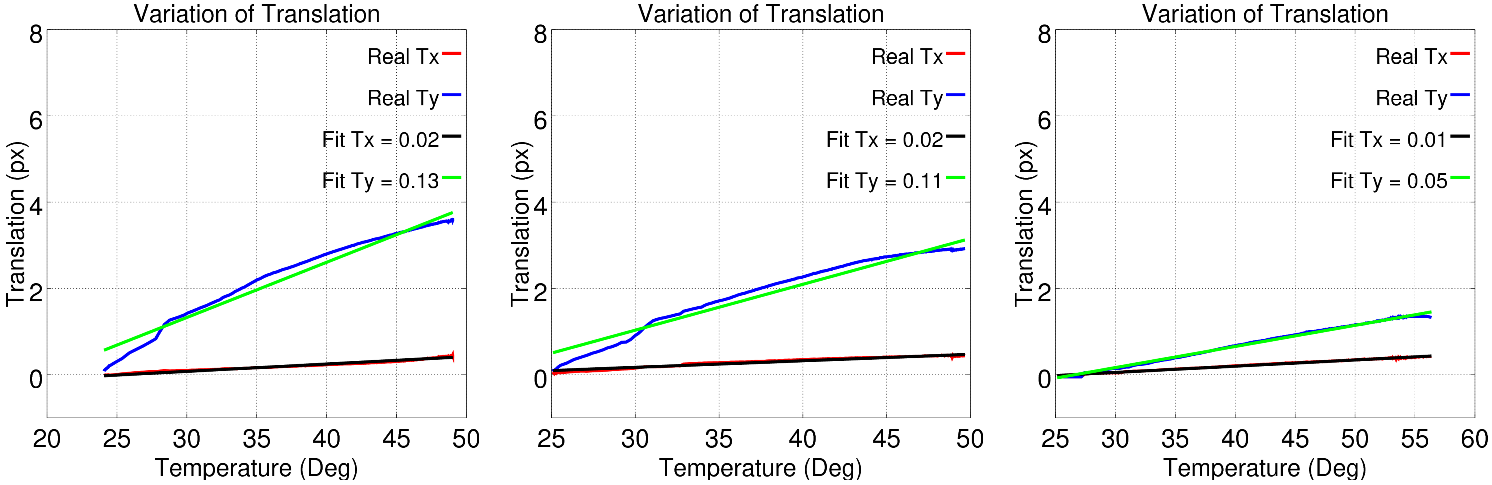

Figure 5.6: Estimation result of translation: dataset 1-3 (from left to right)

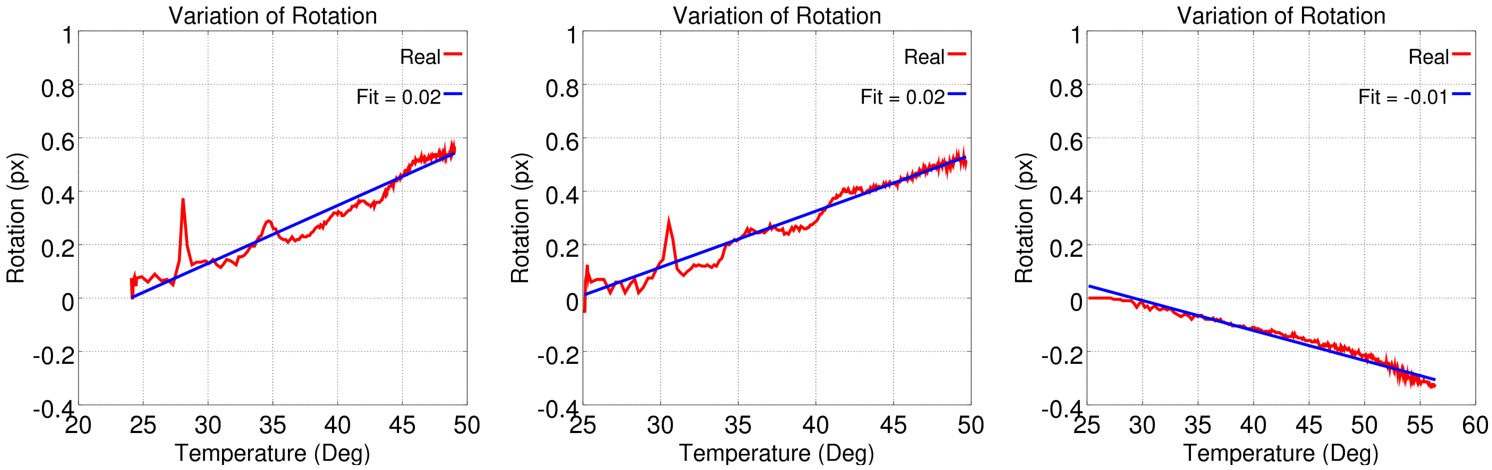

Figure 5.7: Estimation result of rotation: dataset 1-3 (from left to right)

than 0.02 px/°C). The thermal effect is reproducible but not repeatable over time for all parameters. We are not yet able to explain why translation varies differently over time. To be mentioned, the slope of the focal length variation (0.07-0.08 px/°C)) is of the same scale as the result presented in [Merchant 2012, Merchant 2006] (0.068 px/°C)).

For Type II acquisition, the 2D deformation maps of the investigated image couples are generated. In both image couples, the deformation is very slight along axis x and y. Figure 5.9 gives an example of the deformation maps since

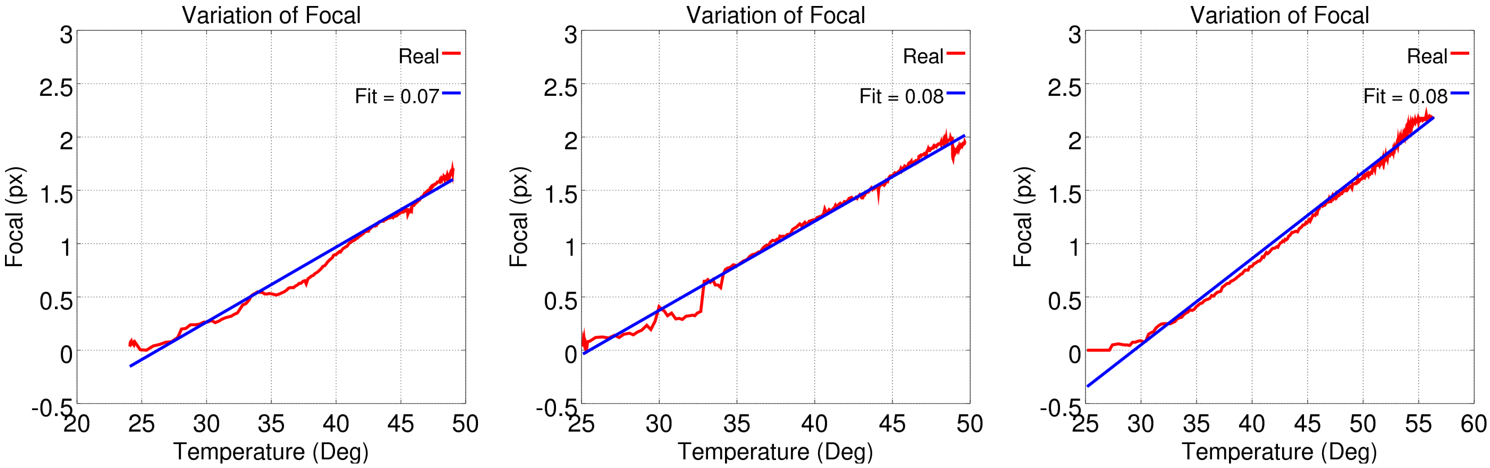

Figure 5.8: Estimation result of focal length: dataset 1-3 (from left to right)

they are all similar. Table 5.4 shows statistics of the deformation maps.

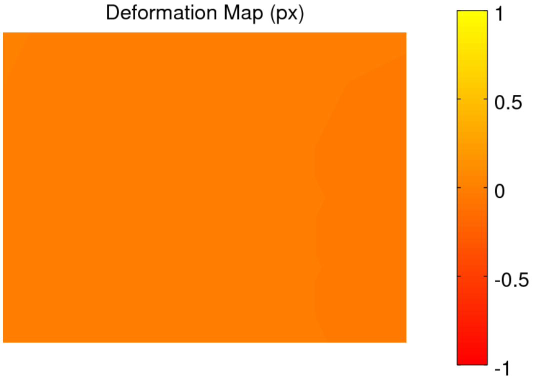

Figure 5.9: One of the deformation maps of the investigated image couples

	min (px)	max (px)	mean (px)	std (px)
Axis X Couple 1	-0.04	0	-0.01	0.01
Axis Y Couple 1	0	0	0	0
Axis X Couple 2	-0.04	0.04	-0.01	0.02
Axis Y Couple 2	0	0	0	0

Table 5.4: Statistics of image couple deformation

The deformation maps are homogeneous; along axis y, there is no deformation between two images taken under the same temperature with a time interval of 30 min while the deformation along axis x remains insignificant compared to the deformation when the temperature of `CMOS` image sensor increases. Therefore, the temperature variation is the main cause of the deformation on images and this deformation is repeatable and can be modeled.

5.3.2 Static space resection

An acquisition with the camera mounted on a heavy geodetic foot is performed on a scene equipped with `GCPs` of which 3D positions are estimated with topometric measurements. The idea of this experiment is to determine the influence of the temperature on certain camera internal parameters, in this case the focal length and the principal point. The position of the camera is considered as static during the acquisition, one focal length and one principal point is estimated for each image. Figure 5.10 shows an image of the scene and the variation of camera temperature during the acquisition. Table 5.5 gives information of the acquired dataset.

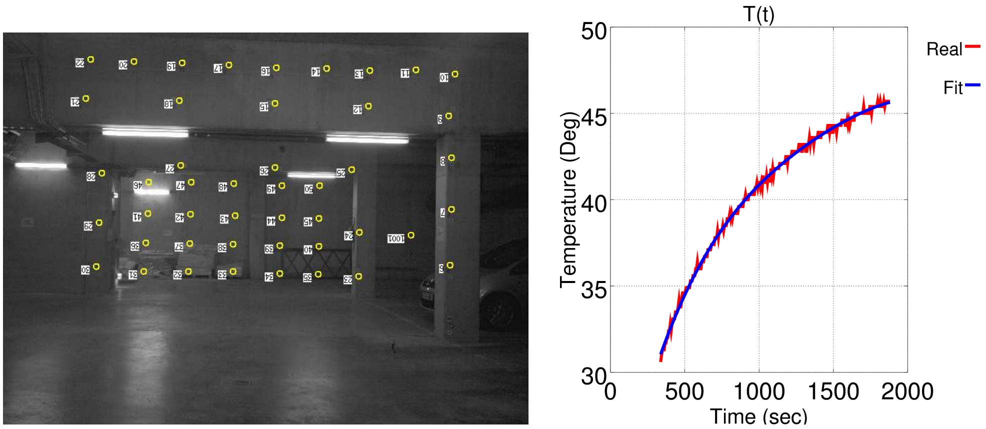

Figure 5.10: Image of the scene with equipped GCPs (left) and variation of temperature (right)

Given the huge number of acquired images and the density of `GCPs` network, image measurement of `GCPs` is performed manually only on the first image and is considered as a true measurement. The image measurement of the remaining images is obtained by performing correlation with the first image. Since we consider the camera as static, manual measurements are used as an initial prediction for correlation. The correlation threshold is set to 0.9 and the average deviation with respect to the true measurement (manual measurement of the first image) is 0.2 px. The average deviation is relatively

Acquisition time (min)	26
Number of images	263
Temperature range (°C)	[30.6,45.7]
Mean Nb of `GCPs` / image	21
Mean `GSD` (mm)	2.7
`DOF` Topometric Network	488
Mean `GCP` accuracy (mm)	1.7

Table 5.5: Information on static space resection dataset

small, the image measurements obtained with correlation is thus assumed valid.

5.3.2.0.1 Results Figure 5.11 shows the reprojection error of `GCPs`. The blue curve depicts the `GCP` reprojection error of the first image and gives an indication of the pose estimation quality. The black curve shows the average `GCP` reprojection error by estimating a focal length and a principal point per image. The reprojection error of the first image has an average of 0.57 px and a dispersion of 0.34 px while for the mean reprojection error, the average is of 0.16 px and the dispersion of 0.07 px. With the mechanical installation, the stability of the camera is ensured. Small residues indicate an accurate pose estimation and justify the imposition of the camera pose on other images. The estimation of focal length and principal point for images is therefore considered reliable.

Figure 5.12 shows the variation of focal length and principal point over temperature. The variation of the focal length is coherent with the results obtained in Section 5.3.1 while the planimetric trend of principal point does not correspond to the translation parameters. This is partly due to the fact that acquisitions are widely spaced over time. With different calculation techniques and independent datasets, the thermal deformation can be modeled and is reproducible at least for focal length.

We are aware that this calibration experience is similar to the 2D matching one (section 5.3.1). However, it allows a self-confirmation on at least focal length variation.

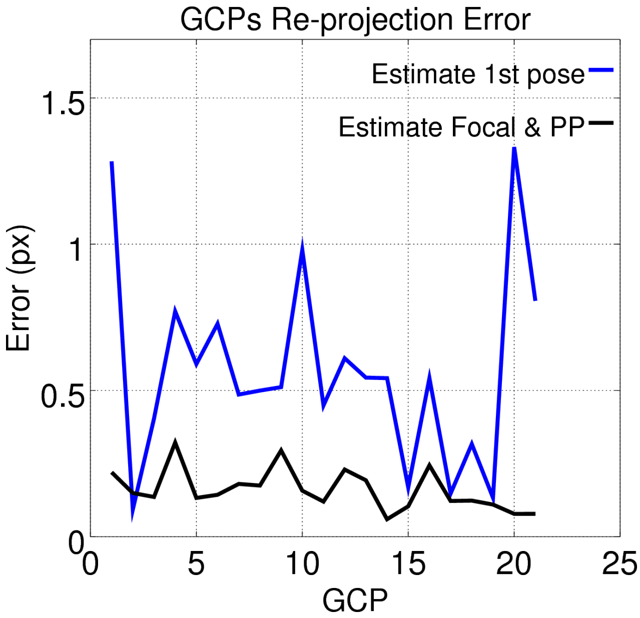

Figure 5.11: `GCP` re-projection error of the first image and mean `GCP` re-projection error of all images

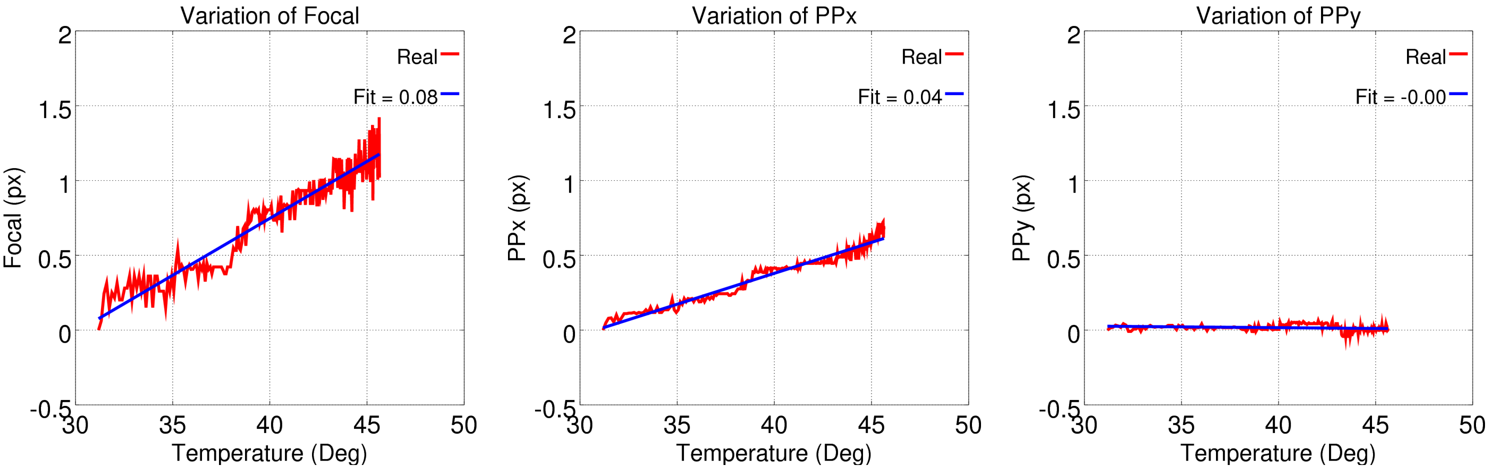

Figure 5.12: Evolution of estimated focal length and principal point values.

5.3.3 Standard space resection

This experiment consists in performing several stereoscopic acquisitions of the same scene as in the previous experiment. Each of these acquisitions is carried out in a very short time so as to assure a small temperature interval while each acquisition is performed under a different temperature. Figure 5.13 shows an image panel of one dataset and the geometry of the acquisition, Table 5.6 gives informations on all acquired datasets.

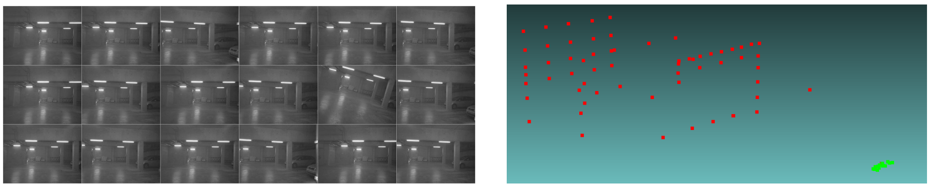

Figure 5.13: Panel of acquired images (left) and geometry of acquisition (right). Camera positions (green) and 3D positions of `GCPs` (red).

	Dataset 1	Dataset 2	Dataset 3
Number of images	14	16	18
Temperature range (°C)	[25.2,29.5]	[39.2,39.6]	[45.4,45.7]
Mean temperature (°C)	27.6	39.3	45.5
Mean `GSD` (mm)	2.7		
`DOF` Topometric Network	488		
Mean `GCP` accuracy (mm)	1.7		

Table 5.6: Information on standard space resection datasets

The aim of this experiment is to estimate one focal length and one principal point per dataset and investigate the relation between these two parameters and image sensor temperature as in the previous case. The observations consist of 3D coordinates of `GCPs` and their image measurements whereas camera poses and one single camera model per dataset are the unknowns to be estimated. The temperature variation of the first dataset is more important than the two other datasets, because the temperature increases more rapidly when the temperature is low.

5.3.3.0.1 Results For each dataset we estimate one camera model for the whole dataset. Figure 5.14 presents the average reprojection error of `GCPs`. Table 5.7 gives statistics of `GCP` reprojection error and internal parameter estimation (focal length and principal point). Figure 5.15 shows the variation of estimated parameters over temperature.

It is difficult to carry out image acquisitions at low temperatures because the temperature increases more rapidly. This experience should also be supplemented by additional datasets at other temperature values. However, we can

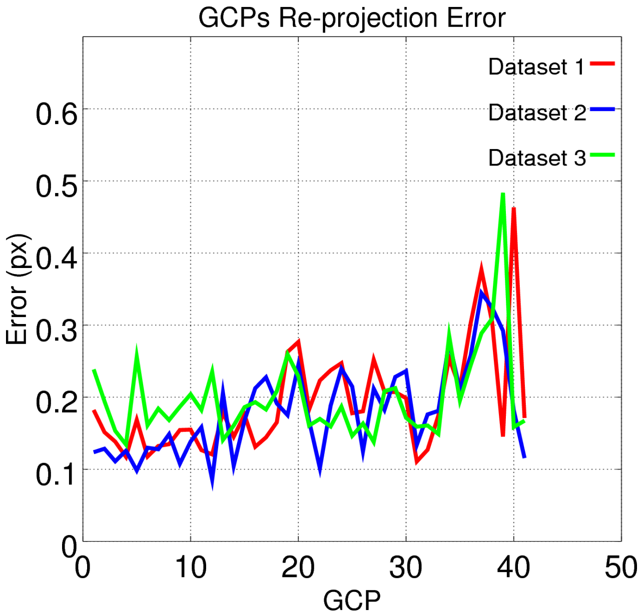

Figure 5.14: `GCP` reprojection error

	Dataset 1	Dataset 2	Dataset 3
mean (px)	0.19	0.18	0.20
std (px)	0.07	0.06	0.06
F (px)	5506.02±0.5	5506.16±0.6	5507.59±0.5
PP_x (px)	2528.49±0.5	2529.40±0.5	2527.27±0.4
PP_y (px)	1931.64±0.5	1933.90±1.1	1936.56±0.8

Table 5.7: `GCP` re-projection error and estimated focal length and principal point

point out that the focal length remains consistent with the results obtained by 2D matching and static space resection.

5.4 Experimental evaluation

5.4.1 Terrestrial photogrammetric acquisition

A terrestrial dataset is studied here to quantify the improvement in terms of photogrammetric accuracy introduced by the correction of thermal effect. The dataset shown in Figure 5.16 and Table 5.8 is an image sequence taken around a pylon (strong 3D scene with highly convergent camera angles and 90° rotated images in order to improve self-calibration bundle block

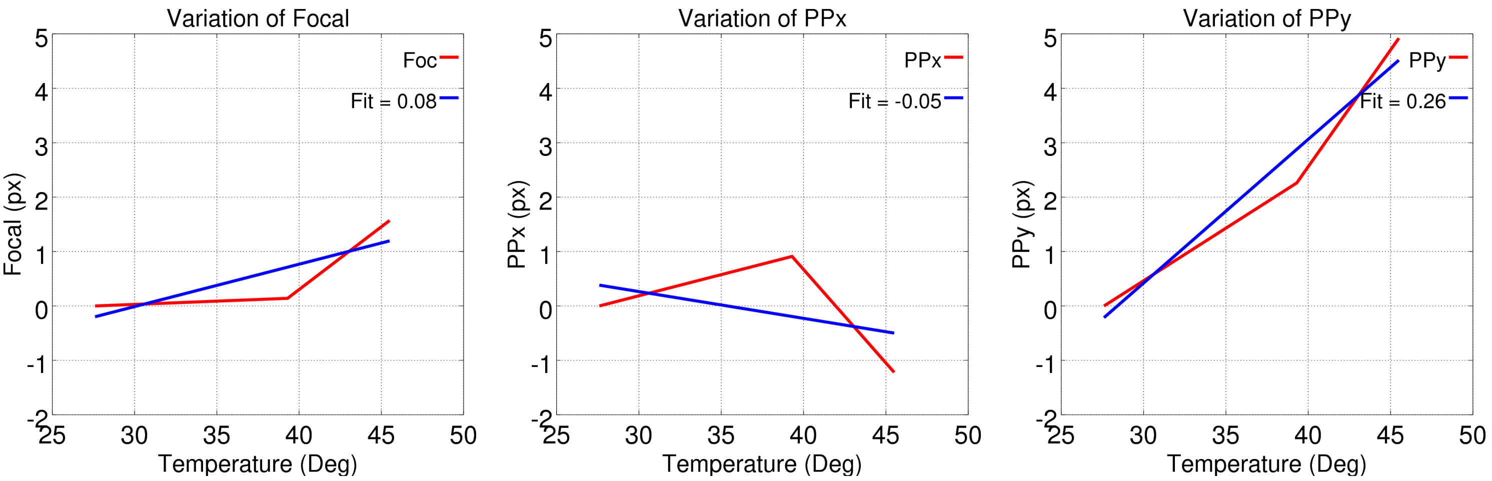

Figure 5.15: Estimated values of focal length and principal point.

adjustment accuracy) with an overlap between the first and the last image, i.e., the first and the last image are taken almost from the same point of view. The scene is equipped with a network of `GCPs` which coordinates are estimated based on topometric measurements. An important temperature increase is observed during the acquisition which can lead to image deformation.

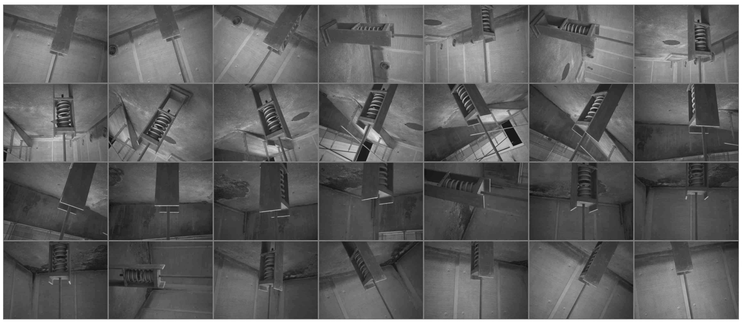

Figure 5.16: Dataset around a pylon

A correction of the thermal effect is applied respectively to tie points and image measurements of `GCPs` as explained in section 5.2. The average error of geo-referencing is investigated for two cases, the conditions of these two cases are as shown in Table 5.9.

In case 1, tie points are extracted with algorithm `SIFT` and image measurements are based on raw images. In case 2, tie points and `GCPs` image measurements are all generated by applying a correction on raw tie points co-

Number of images	28
Number of GCPs	13
Acquisition time (min)	14
Temperature range (°C)	[23,31]
Mean `GSD` (mm)	0.6
`DOF` Topometric Network	111
Mean `GCP` accuracy (mm)	0.3

Table 5.8: Information on terrestrial dataset

Correction ($\surd$ or $\times$)	Case 1	Case 2
Images	×	×
Tie points	×	$\surd$
`GCPs` image measurements	×	$\surd$

Table 5.9: 2 Cases of the terrestrial dataset

ordinates and raw image measurements of `GCPs`, respectively. The generation of corrected tie points has a significant advantage of being fast and resulting in higher photogrammetric accuracy compared to recomputing tie points on corrected images.

5.4.1.1 Standard configuration results

A standard photogrammetric pipeline is performed on the terrestrial dataset. We use three correction maps generated with three different datasets in section 5.3.1. Figure 5.17 shows the geometry of the acquisition. The geo-referencing residuals on `GCPs` are as shown in Figure 5.18 and some statistics are given in Table 5.10.

	min (mm)	max (mm)	mean (mm)	std (mm)
Raw images	1.8	7.9	4.7	1.8
Correction 1	2.2	6.7	4.2	1.4
Correction 2	2.4	6.5	4.2	1.3
Correction 3	0.5	7.3	3.2	2.0

Table 5.10: Statistics of geo-referencing residuals on `GCPs`

With the correction of thermal effect, the geo-referencing residuals on `GCPs` decrease. Both correction 1 and 2 give similar results whereas correction 3 gives a greater improvement. This is explained by the higher temperature

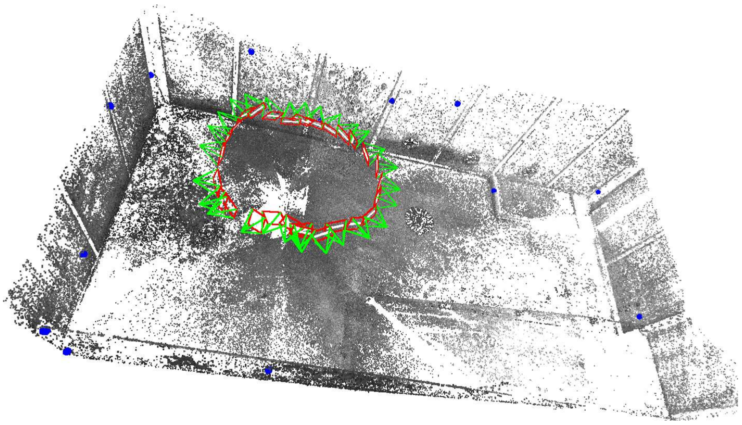

Figure 5.17: Geometry of terrestrial photogrammetric acquisition with `GCPs` (blue)

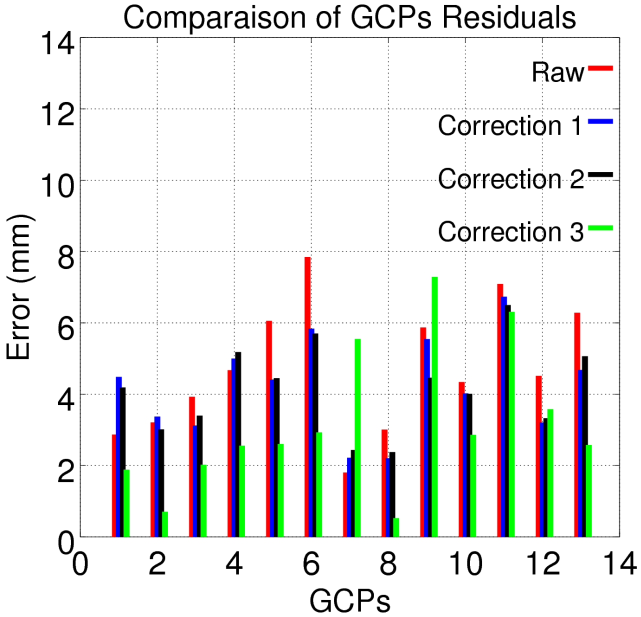

Figure 5.18: Residuals on `GCPs`

measurement precision as specified in Section 5.3.1. The correction of thermal effect improves by 1.5 times the photogrammetric accuracy in a classical configuration.

5.4.1.2 Single strip configuration results

In this configuration, we consider that the acquisition is linear despite the fact that the first and the last images share almost the same point of view, i.e., no tie points are extracted between these two images. This linear condition can lead to bent 3D models described as bowl effect [James & Robson 2014b]. Bowl effect is here demonstrated by the deviation of tie points quadruplets between the first two and the last two images, i.e., tie points that exist in all these 4 images. The 3D position of tie points is estimated by pseudo-intersection performed with the first two and the last two images.

To investigate the improvement introduced by the correction of thermal effect in terms of bowl effect, the 3D position deviation of tie point quadruplets between the first two and the last two images, also called closing error, is studied. Here, only the map giving the best correction is used, i.e., correction 3 (Table 5.10). Figure 5.19 depicts the overlapping situation between images in standard configuration (left) and single strip configuration (right), a line is plotted when two cameras take overlapping images. We notice that red lines connecting the first and last two images have been removed, which means no tie point extraction is performed within these four images.
Figure 5.20 gives the closing error in this terrestrial acquisition and Table 5.11 gives statistics of the deviations.

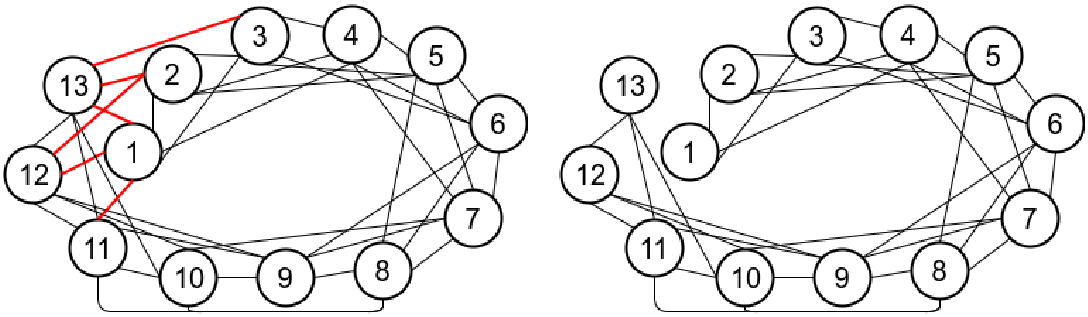

Figure 5.19: Demonstration of image overlapping situation: a single strip configuration is simulated when no tie point extraction is performed for image couples indicated with a red line

From Table 5.11 we can see that the closing error declines by 3.6 times when the thermal effect is corrected, which means the influence of bowl effect is less significant and a better photogrammetric accuracy can be achieved.

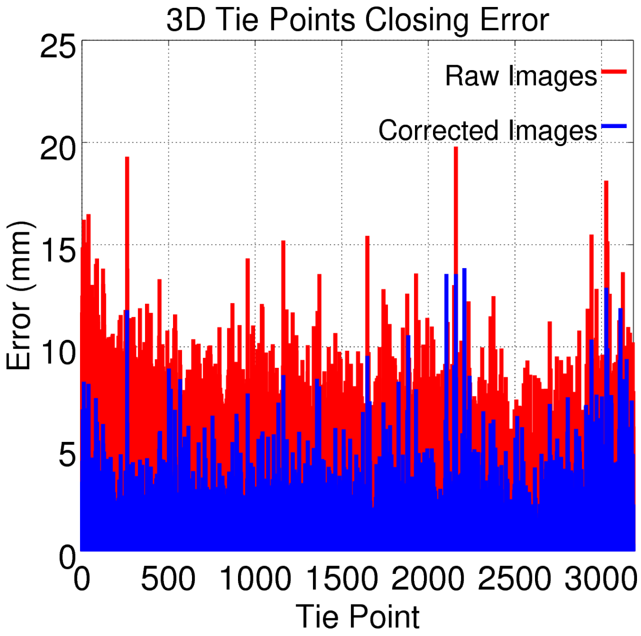

Figure 5.20: Closing error in the terrestrial photogrammetric acquisition on tie point quadruplets

	min (mm)	max (mm)	mean (mm)	std (mm)
Raw images	1.4	19.8	6.2	2.1
Correction 3	0.0	13.9	1.7	1.6

Table 5.11: Closing error of the terrestrial acquisition

5.4.2 Airborne photogrammetric acquisition

5.4.2.0.1 Terrestrial Camera Calibration A terrestrial dataset is acquired on a scene with an important variation of depth in order to robustly estimate a camera calibration model so as to be used as an input when processing the aerial dataset. In fact, aerial acquisition on a scene with a small range of elevation does not allow a reliable estimation of camera internal parameters in a self-calibration strategy due to the correlation between internal and external parameters during bundle block adjustment. This scene is equipped with a network of `GCPs` which coordinates are estimated by topometric measurements. The use of `GCPs` during bundle block adjustment allow to constrain the estimation of internal parameters with a hybrid compensation that mixes `GCPs` and tie points. Figure 5.21 shows a panel of the acquired convergent images and Table 5.12 gives information on the dataset.

Figure 5.21: Terrestrial images on a 3D scene for camera calibration

Number of images	43
Temperature range (°C)	[34.2,36]
Number of `GCPs`	28
Mean `GSD` (mm)	0.9
Mean `GCP` accuracy (mm)	0.5

Table 5.12: Information on terrestrial calibration dataset

This dataset allows the establishment of a camera model for raw images as well as for images where thermal effect has been corrected. Each of the two models will then be used as input during relative pose estimation of the aerial dataset. Although the amplitude of temperature variation is very small, the impact on camera model estimation remains perceptible as well as on the geometric accuracy.

5.4.2.0.2 Results The strategy of the processing is standard and follows the scheme given in Section 5.2.4. Figure 5.22 shows the geometry of the acquisition as well as the reprojection residuals of `GCPs` for both raw and corrected images.

For raw images, the mean average re-projection error of `GCPs` is 0.52 px with a dispersion of 0.22 px whereas for thermal effect corrected images the

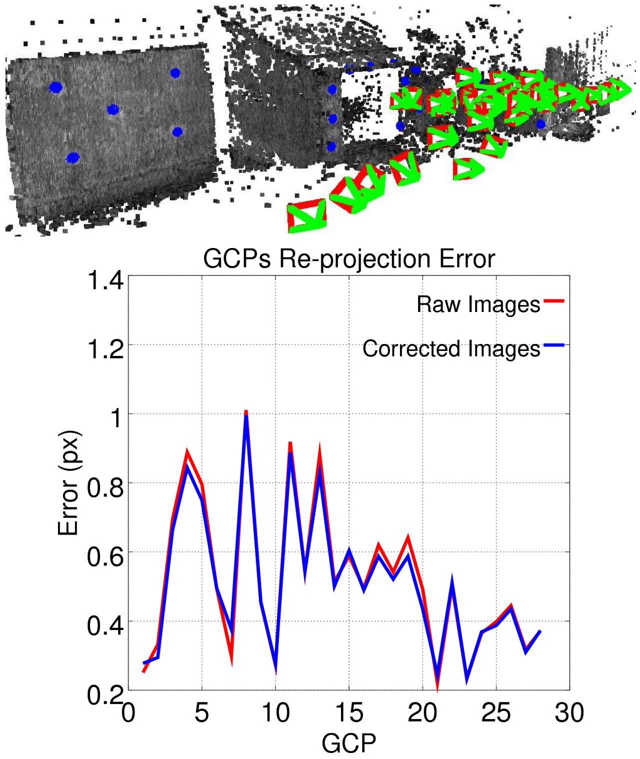

Figure 5.22: Geometry of acquisition for camera model calibration and `GCP` distribution (left), mean `GCPs` re-projection error (right)

average is 0.50 px with a dispersion of 0.20 px.

We note that for an identical processing, taking into account the temperature effect gives better statistics, even if the impact is almost negligible. This is explained by the fact that, the variation of temperature is almost insignificant (1.6°C) and due to correlation between internal and external parameters, the `GCP` re-projection errors is mainly due to `GCP` image measurement. However, we can still compare the estimated camera models ζ and $\zeta^{'}$ for raw and corrected images, respectively as follows:

$$d(\zeta,\zeta^{'}) = \min_{\mathcal{R}} \iint ||\zeta - \mathcal{R}\cdot\zeta^{'}||^2 dxdy$$

where: ζ estimated internal model for raw observations;
$\zeta^{'}$ estimated internal model for corrected observations;
$\mathcal{R}$ estimated rotation

Figure 5.23 shows the difference between these two internal models.

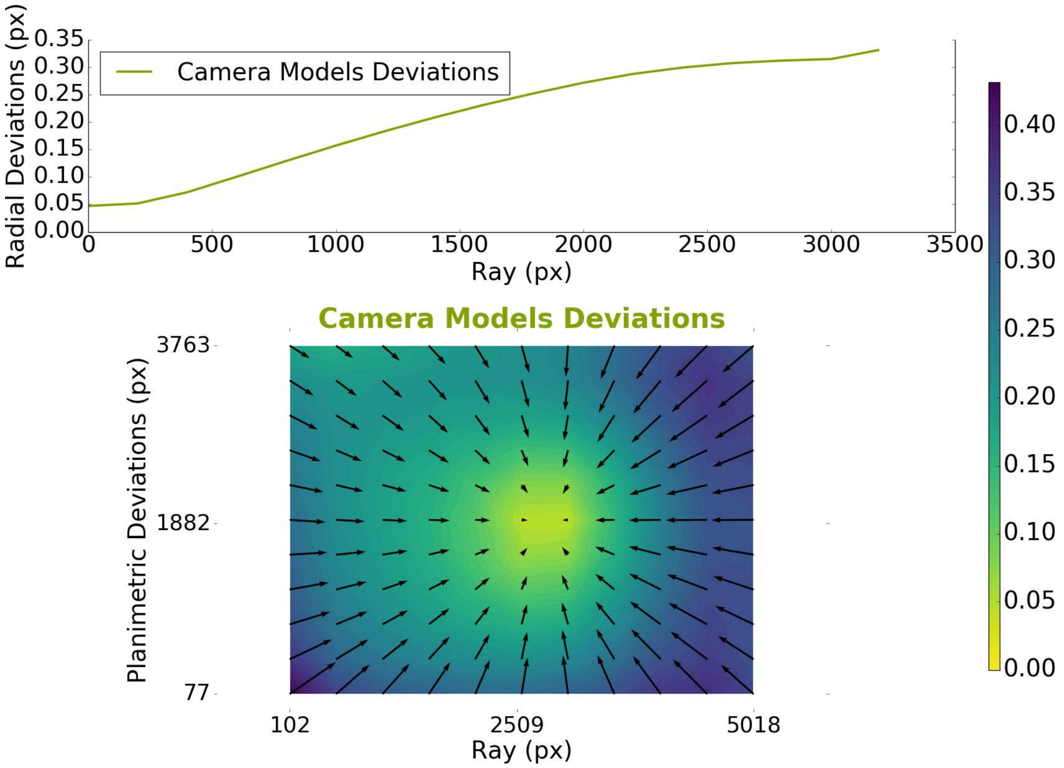

Figure 5.23: Comparison of the two estimated internal camera models

We notice that the temperature effect introduces a bias of 0.05 px and a deviation of up to 0.33 px on the corners of images. The value of the focal length has a variation of 0.61 px with an uncertainty of 0.14 px and the mean deviation on the whole image sensor is 0.23 px. The focal length has a significant variation and the average deviation is twice as expected. This result is partly due to the fact that the terrestrial acquisition does not allow to decorrelate enough the internal parameters. The profile of the difference of both internal models shows that the variation of focal length is compensated by a variation of distortion.

5.4.2.0.3 Aerial Dataset An aerial dataset is acquired with a `UAV` in a corridor configuration. The images consist of 2 strips presenting a linear road of about 500m. The aim of this experiment is to show the impact of the thermal effect correction on accuracy for cartographic purposes, for instance, where high accuracy is required. Figure 5.24 shows a panel of acquired images and temperature variation during image acquisition, Table 5.13 gives some information about the photogrammetric aerial dataset. Figure 5.25 shows the geometry of this corridor acquisition.

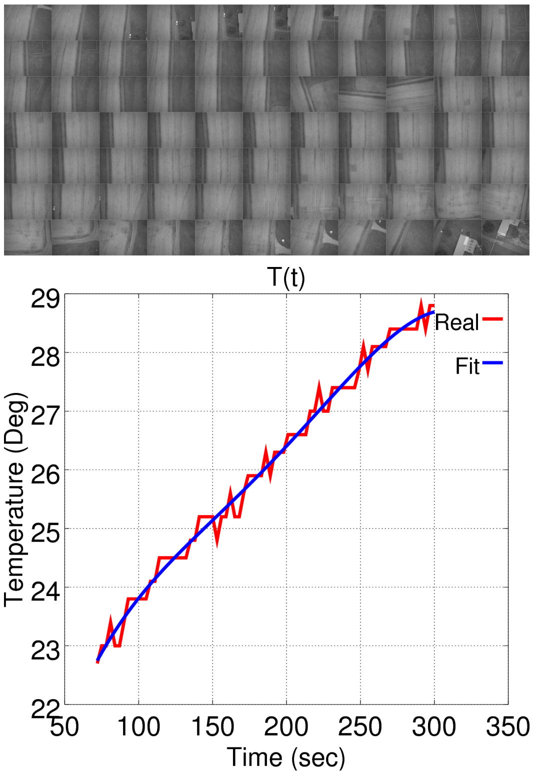

Figure 5.24: Panel of acquired corridor dataset (top) and image temperature variation (bottom).

Flight time (min)	15
Number of images	77
Number of `GCP`s	10
Flight height (m)	70
`GSD` (cm)	1
`GCP` accuracy (cm)	1
Overlap	75%,75%

Table 5.13: Information about aerial dataset

For this `UAV` acquisition, we investigate the impact of the thermal effect on the photogrammetric accuracy. An internal camera model is given

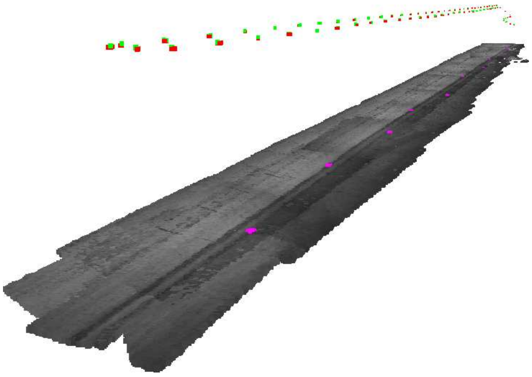

Figure 5.25: Geometry of corridor acquisition and distribution of `GCPs` along the scene (in purple).

as input based on the terrestrial pre-calibration. `GCPs` coordinates are estimated using `GNSS RTK` surveying. Residuals on `GCPs` are used to quantify the improvement of photogrammetric accuracy after thermal effect correction.

5.4.2.0.4 Results The geo-referencing residuals on `GCPs` quantify the accuracy improvement obtained with the thermal deformation correction. Figure 5.26 shows the residual on every `GCP` for both raw and corrected images. Table 5.14 shows the statistics of the geo-referencing residuals. For certain `GCPs` the geo-referencing residual slightly increases. Nevertheless, for the rest of the `GCPs` the residual declines significantly. Statistic results show that under real acquisition conditions, by correcting the thermal deformation on images, a better photogrammetric accuracy is performed. The accuracy improvement by 1.4 times is quite satisfying for an acquisition of a corridor configuration of 500m.

	min (mm)	max (mm)	mean (mm)	std (mm)
Raw images	5.9	39.6	21.4	11.0
Corrected images	5.9	24.9	15.5	6.6

Table 5.14: Geo-referencing residuals on `GCPs` for airborne dataset

5.5 Conclusion

This section presents different strategies for studying the thermal deformation on images due to the temperature variation of image sensor. To our best

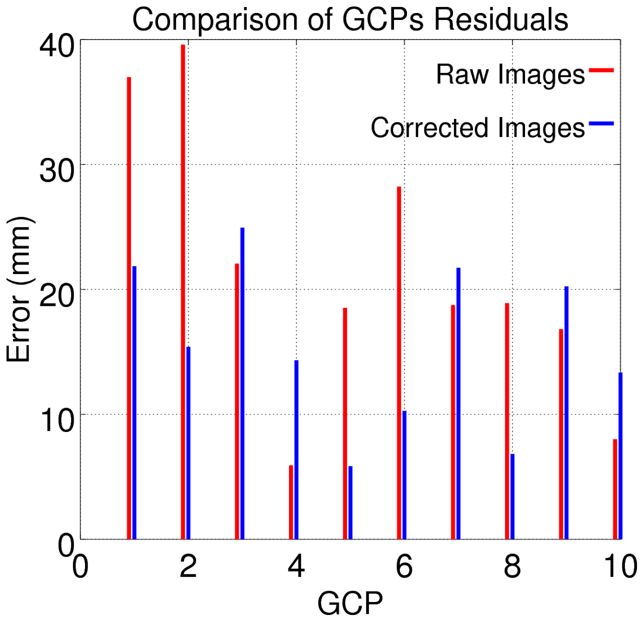

Figure 5.26: Geo-referencing residuals on each `GCP` for both raw and corrected images

knowledge, this is the first time the issue of thermal deformation is studied in the context of light weight metric camera devoted to `UAV` photogrammetric acquisitions.

The 2D matching experiment proves the existence of the thermal deformation on internal camera parameters and the temperature change of image sensor is the main reason. This method for quantifying the deformation is complete and exhaustive since it allows to study the deformation for every pixel of the image sensor. The variation of focal length and rotation can be interpreted as the result of image sensor deformation caused by component dilatation as temperature changes; the variation of translation can be explained by the deviation of principal point. A good repeatability over time of the focal length variation (0.07-0.08 px/°C) is observed and the variation corresponds to results presented in [Merchant 2006, Merchant 2012]. The impact of the thermal deformation on translation and rotation differ over time, but the variation of rotation remains insignificant (less than 0.02 px/°C during acquisition). The thermal deformation is therefore reproducible and can be modeled and corrected. Further investigations are required to study the long term stability.

The static space resection experience confirms the repeatability of the thermal impact on focal length using a different technique than 2D matching and independent datasets. An automatic target tracking method is applied for finding the position of `GCPs` in images. The standard space resection experience give the same tendency for focal length (0.08 px/°C) when the image sensor undergoes a temperature increase. However, the number of datasets remains insufficient and more datasets should be carried out so as to study thoroughly the issue. For those two types of space resection experiment, the variation of principal point is not reproducible, further investigations are required to better understand the problem.

With terrestrial and aerial dataset, a greater photogrammetric accuracy is achieved when taking the thermal effect of image sensor into account. For the terrestrial dataset, the photogrammetric accuracy is improved by 1.5 times in standard strip acquisition configuration and the bowl effect is quantified by a new approach consisting of calculating the closing error; this `GCP` free approach shows that by taking into account the thermal deformation, the bowl effect is decreased by 3.6 times. For the aerial dataset in a corridor configuration of 500m, a terrestrial calibration is carried out before the flight. For this acquisition, the temperature varies 1.6°C and the influence of thermal deformation can seem to be small. However, when processing the aerial dataset using the corrected calibration model, the photogrammetric accuracy is 1.4 times better.

Further works need to be focused on the study of the long term stability of the thermal effect. Although the reproducibility on the focal parameter has been verified thanks to dataset 3 of section 5.3.1 acquired 4 months after the first ones, we cannot be conclusive yet about the stability of the thermal deformation over time. Even if a calibration is required at regular intervals, our calibration method based on 2D Matching is simple to implement and fully automated. A possible limiting factor of the calibration strategy is the determination of interior parameters in a close range configuration and its use in aerial configurations [Lichti *et al.* 2008].

However, we observed an improvement of accuracy for an airborne dataset (Section 5.4.2) and the thermal effect seems, at the first order, independent of the variation of interior parameters. We can summarize our suggestion as follows:

$$\begin{aligned}\mathcal{C}(T,d) =& \mathcal{C}(T_0,d) + \frac{\partial \mathcal{C}_{(T_0,d)}}{\partial T}\delta T \\ =& \mathcal{C}(T_0,d) + \frac{\partial \mathcal{C}_{(T_0,d_0)}}{\partial T}\delta T + \frac{\partial^2 \mathcal{C}_{(T_0,d_0)}}{\partial T \partial d}\delta T \delta d\end{aligned}$$

where: $\mathcal{C}(T,d)$ is a correction function depending on temperature T and field depth d;

T_0 is the reference temperature;
d_0 is the field depth for calibration

The 2nd order term $\frac{\partial^2 \mathcal{C}_{(T_0,d_0)}}{\partial T \partial d}\delta T \delta d$ can be considered negligible and the correction function can be expressed as:

$$\mathcal{C}(T,d) = \mathcal{C}(T_0,d) + \frac{\partial \mathcal{C}_{(T_0,d_0)}}{\partial T}\delta T$$

Under this assumption, the in-lab close-range calibration procedure is still valid even at considerable aerial operating distances.

Finally, experiences should be carried out with different image sensors to better study this phenomena.

Acknowledgements

We wish to thank the `LOEMI` team of the `LaSTIG` laboratory for all their help and in particular for providing the equipment. We thank Mathieu Peyréga for the loan of the Peltier thermoelectric cooler. Finally, we thank `SIXENSE Mapping`, `Compagnie Nationale du Rhône` and `IGN` companies for funding this research.

Chapter 6

Conclusions & Perspectives

Contents

6.1 Conclusions 125

6.2 Perspectives 127

6.1 Conclusions

This thesis deals with `UAV` aerial survey carrying lightweight sensors for centimeter precision geometrical 3D modeling. The considerable evolution of aerial vectors, cameras and the miniaturization of navigation sensors (`GNSS` receivers, antennas and inertial units) increasingly light, more and more low-cost and more and more accurate allow to consider light acquisition systems which can reach centimeter accuracy in optimal conditions, thus considerably reducing field topographic work.

This research mainly addressed the problem of `GPS` assisted geo-referencing of a photogrammetric acquisition. We present a lightweight system whose mass does not exceed 2 kilograms. This system consists of sensors developed within the `LOEMI` instrumentation team of `IGN`'s `LaSTIG` laboratory. These sensors are the `GéoCube` and the `CamLight`. The system developed is specially designed for `UAV` acquisitions with a purpose of metrological use. It also permits to reduce the mass of the payload and to be able to benefit from the maximum `UAV` autonomy. Moreover, in the current version of the system, the `GNSS` receiver is integrated into the camera casing which makes the system even more compact.

The importance of internal, spatial, temporal and thermal calibration aspects are studied. The internal calibration of the camera's geometry consists in the use of a physical model coupled with a mathematical polynomial model. This hybrid model allows to improve the estimation accuracy of the internal parameters, in particular, the modeling of residual high frequency errors not taken into account by standard physical models.

The spatial calibration between the antenna center of the `GPS` and the optical center of the camera is also studied. The conventional in flight self-calibration method is compared to a new method of lever-arm calibration based on photogrammetric measurements. This method requires no mechanical constraint on the mounting of the sensors on the `UAV`. A 3D photogrammetric modeling of the drone allows to estimate this vector preceded by an instrumental calibration procedure for pseudo-materialization of the phase and optical centers. On a real dataset the accuracy achieved by this new method is 2 *cm* ± 1.4 *cm* on check points while the self-calibration method gives an accuracy of 1.8 *cm* ± 0.8 *cm*. The deviation is not significant and the accuracy achieved meets the tolerance demand in our work. However, the second method, has a considerable advantage in flexibility of implementation and requires no ground control points.

The issue of time synchronization is studied. The camera used in the course of our experiments has a negligible electronic delay given the typical conditions of acquisition of our system. This problem is however studied for a commercial camera. We show that for this type of commercial sensor, the electronic delay is not only important (for example 64 *ms* for the `Sony-RX1`) but also unstable and has a significant dispersion. We show, however, that it is possible to take into account this delay by modeling it as an unknown in the observation equation which links the `GPS` and photogrammetric observations, if instantaneous velocities measurements are provided.

A real dataset consisting of a calibration and a repeatability flights are studied. Different data fusion strategies are proposed for the first experiment. A study of the precision of the parameters estimated during the bundle adjustment allows to establish the optimal calibration strategy. For a robust estimation, it is essential to add constraints during the acquisition (ground control points, oblique images or images at different heights). This has the effect of better decorelate the internal and external parameters and particularly the focal length, the principal point and the lever-arm. The accuracy of the calibration acquisition is evaluated on check points. The accuracy achieved is 0.8 *cm* ± 0.5 *cm*. For the repeatability data, the parameters estimated during the previous calibration are used and the accuracy evaluated on check points is 2 *cm* ± 0.5 *cm*. We show that the developed system achieves a centimeter accuracy that meets the tolerances required on a large number of `UAV` mapping applications.

In order to improve photogrammetric positioning accuracy, an experimental study is proposed on the thermal deformation of images. Temperature measurements are made available by the imaging sensor of the camera. Different experiments of highlighting this effect are conducted: calculation of the thermal deformation by 2D matching, static space resection and finally by classical space resection. These different experiments show a repeatable effect on the internal parameters of the camera and reproducible for the focal length. We show on real data, terrestrial and aerial, that the modeling of this effect and its correction allows an improvement of the accuracy of a factor of 1.5 and a factor 3.6 in a single strip configuration.

6.2 Perspectives

Lever-Arm pseudo-materialization method In order to validate the lever-arm calibration method suggested here, it is necessary to conduct a second experiment where two independent datasets need to be acquired. The position and the orientation of the camera have to be different for each dataset. The first flight will be used to correct the value of the measured lever-arm on the ground from the multi-path effect, whereas the second flight will determine whether this correction improves the accuracy on check points in comparison with the results obtained using the standard calibration strategy with `GCPs`.

Integrated Sensor Orientation The system developed in this study shows that it is possible to achieve centimeter absolute accuracy using low-cost sensors whose development and integration were performed in a laboratory. In further work, the stability of the system, the stability of the internal parameters of the camera will be particularly investigated, while the lever-arm offset can be estimated robustly by adapting the flight plan. If the camera has a proper reproducibility it is possible to use this system with 0 `GCP` although it is always advisable to have at least 1 `GCP` to improve final accuracy. The data fusion strategy can also be improved by integrating, for example, the possibility of estimating different lever-arm vectors per group of images during the compensation. This allows, for example, to integrate oblique images for a better estimation of camera's internal parameters in self-calibration configuration. Future work will continue, with the aim of improving accuracy, for example by testing the addition of a second frequency and using a multi-constellation receiver. This is why, today, the significant development of `OEM` for embedded systems is encouraging manufacturers to offer cheap dual-frequency `GNSS` models.

Thermal deformation For the modeling of the thermal effect, further studies on the influence of temperature on optics could be considered. In addition, it would be interesting to conduct the same study on commercial sensors.

Appendix A

MicMac Installation

A.1 Dependencies

`MicMac` installation requires several software dependencies. It is possible to use `MicMac` with the compiled binaries however we present here the instructions to follow in order to compile `MicMac` from source files and thus guarantee the proper functioning of the software to realize B and C tutorials. This installation is only valid for `Linux` operating systems and has been verified on the following distribution: `Ubuntu 16.04.3 LTS`. For other operating systems users, no guarantee is provided for the use of the software and the processing of available sample data below. For more informations, please refer to the installation instructions available in the official `MicMac` documentation repository `https://github.com/micmacIGN/Documentation`.

`MicMac` external dependencies are free softwares used for managing image conversion, reading/writing image meta-data, managing coordinate systems, parallel processing management and the use of a graphical interface for image measurements and 3D visualization.

For dependencies installation proceeds as follows:

```
:~$ sudo apt-get install x11proto-core-dev
    make libx11-dev imagemagick gcc
    exiftool exiv2 qt-sdk git
:~$ wget http://download.osgeo.org/proj/proj-5.0.0.tar.
   gz
:~$ wget http://download.osgeo.org/proj/proj-datumgrid
   -1.7.tar.gz
:~$ tar xzf proj-5.0.0.tar.gz
:~$ cd proj-5.0.0/nad
:~$ tar xzf ../../proj-datumgrid-1.7.tar.gz
:~$ cd .. && ./configure && make && sudo make install
```

A.2 Download

Once `MicMac` dependencies are properly installed, it is possible to download and install the software from its official repository. `MicMac` uses `Git` as a version control system.

```
:~$ git clone https://github.com/micmacIGN/micmac.git
```

A.3 Compilation

For the purposes of the tutorials below we will compile `MicMac` in a configuration that will allow us to use external softwares and a graphical interface. This configuration is specified at the build process step using `-DWITH_` and `-DBUILD_` arguments. In particular, we will compile `rnx2rtkp`, the `RTKlib` `GNSS` data post-processing module. The compilation commands are as follows:

```
:~$ cd micmac/ && mkdir build && cd build
:~$ cmake ../ -DWITH_QT5=1 -DBUILD_RNX2RTKP=ON
              -DBUILD_POISSON=ON
:~$ NbProc=$(cat /proc/cpuinfo | grep processor | wc -l)
:~$ make clean
:~$ make install -j$NbProc
```

To check if the installation was successful, the following command returns "found" for each dependency.

```
:~$ ./../bin/mm3d CheckDependencies
```

```
git revision : v1.0.beta11-483-gcc5285e
byte order   : little-endian
address size : 64 bits
micmac directory : [/home/micmac/]
auxilary tools directory : [/home/micmac/binaire-aux/linux/]
--- Qt enabled : 5.5.1
library path:  [/usr/lib/x86_64-linux-gnu/qt5/plugins]
make:  found (/usr/bin/make)
exiftool:  found (/usr/bin/exiftool)
exiv2:  found (/usr/bin/exiv2)
convert:  found (/usr/bin/convert)
proj:  found (/usr/local/bin/proj)
cs2cs:  found (/usr/local/bin/cs2cs)
```

To use `MicMac` in a simple way, we can add it to the environment variables as follows:

```
:~$ echo "export PATH=/home/daakir/micmac/bin:'$PATH'"
    >> ~/.bashrc
```

Appendix B

Integrated Sensor Orientation Workflow

B.1 Presentation of the Dataset

The following link [1] contains a set of data which will allow us to perform a relative and absolute integrated sensor orientation with aerial position control of images based on embedded `GPS` data. Below we will detail all the necessary steps to achieve maximum ground accuracy, here, in the range of `1-2 cm` for a classical `UAV` photogrammetric acquisition, based on sensors presented in Section 3.3 and processing strategy presented in Section 4.3. First, we will compute different `GPS` trajectories in order to make comparisons and in a second time we will focus on the fusion of these results with the photogrammetric processing part.

This `UAV` acquisition has been performed by the surveying service of `Vinci Construction Terrassement`. A `DJI-F550` hexa-copter has been used to achieve the flight. The images were acquired by the `IGN` monochromatic light camera developed at the `LasSTIG` laboratory within the `LOEMI` team. The on-board `GPS` raw measurements were acquired by the `GeoCube`, a multi-sensor geo-monitoring system developed at the same laboratory.

The file `Viabon/Pipeline-Viabon.txt` contains all command lines related to this workflow. The data in `Viabon/` directory consist of:

- 73 nadir images in `.tif` raw format
- `15073106.obs` `RINEX` file of rover receiver
- `00012120.15O` `RINEX` file of pivot/base station
- `ct19212z.15o` `RINEX` file of closest `RGP`[1] network station
- `ct19212z.15n` `GPS` satellites navigation file

---

[1] `GNSS` Permanent Network: `http://rgp.ign.fr/`

- `ct19212z.15g` `GLONASS` satellites navigation file
- `igs08.atx` satellites and receiver antennas calibration values
- `CpleImgs.xml` images couples for tie points computation
- `Pts_GeoC.txt` ground points coordinates
- `MesImages.xml` image measurements of ground points
- `SysCoRTL.xml` file for system coordinates transformation

Figure B.1 shows a panel of the acquired images generated with the `mm3d PanelIm` command.

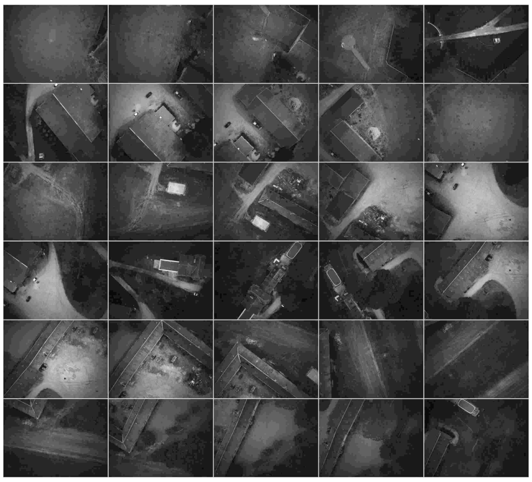

Figure B.1: Panel of Images of the dataset

B.2 Processing Static & Kinematic GNSS Data

For `GPS` data processing we will use `RTKLIB` an open-source `GNSS` processing software. `RTKLIB` consists of several modules (`convbin`, `rnx2rtkp`, `rtkrcv`, ...etc). For more information, please refer to Section 3.4.2. We will only use `rnx2rtkp` module which will allow us to perform post-processing of our data based on different positioning modes.

B.2.1 Reference Station Processing

First we use `mm3d TestLib GpsProc` command to compute the position of the base station which will be used as a reference station to process the `UAV` trajectory. The data recorded by the on-board `GPS` receiver are single-frequency measurements. This implies, for optimal accuracy, having a base station within a maximum radius of ∼10 km. A base station has been installed near the acquisition area (file `00012120.15O`). This station is a multi-constellation dual-frequency `Novatel GNSS` receiver. The position of this receiver is estimated relatively to a reference station of the French permanent `GNSS` network (file `ct19212z.15o`).

First we estimate the position of the static base station.

```
:~$ mm3d TestLib GpsProc './' static 00012120.15O
         ct19212z.15o ct19212z.15n NavSys=5
         GloNavFile=ct19212z.15g Freq=l1_l2
         AntFileRCV=igs08.atx AntFileSATs=igs08.atx
         AntBType=TRM55971.00
```

First mandatory argument is the current directory. Second mandatory argument is the processing mode. Here we tell the software that we want to estimate a position from `static` measurements. Third mandatory argument is the `RINEX` file of a known station, here `CT19`[2] of the French permanent `GNSS` network. Last mandatory argument contains `GPS` constellation navigation parameters. For optional arguments, `NavSys=5` means that we use both constellations `GPS` and `GLONASS` with respect to `RTKlib` conventions. In this case, we need then to give the navigation file of `GLONASS` constellation too using the optional argument `GloNavFile=ct19212z.15g`. Once both receivers are dual-frequency receivers, we perform the processing in both frequencies. This is specified with the optional argument `Freq=l1_l2`. Finally, we use optional arguments to perform antennas corrections and we specify the antenna model for `CT19` as the antenna is listed in The `igs08.atx` file.
Then, 3 files are created:

- `./rtkParamsConfigs.txt` a summary of the options used by `rnx2rtkp`
- `./Output_static.txt` the processing result in `RTKLIB` format
- `./Output_static.xml` the processing result in `.xml` format for `MicMac` internal using

B.2.2 GPS Trajectories Processing

All `UAVs` have at least a single-frequency `GPS` chip which records at least L1 Coarse/Acquisition code signal. First, we process a trajectory based solely on

---

[2] http://rgp.ign.fr/STATIONS/#CT19

this data in order to evaluate its accuracy in the case we have a system which delivers only available code positions.

```
:~$ mm3d TestLib GpsProc './' single 15073106.obs
         NONE ct19212z.15n
```

Here the second mandatory argument, corresponding to positioning mode, value is `single`. This means that we process only rover code measurements. Next mandatory argument is the `RINEX` file of raw measurements of rover receiver (`15073106.obs`). As no relative processing is performed, we give the value `NONE` for the 4th argument. Last mandatory argument correspond to `GPS` constellation satellites navigation parameters. The trajectory is saved in the `RTKlib` and `MicMac` format respectively in files `Output_single.txt` and `Output_single.xml`. The conversion to the `.xml` format can be performed with the `mm3d TestLib ConvRtk` command.

Assume that the `GPS` module of the `UAV` flight controller allow us to record L1 C/A code raw data. Then, it is possible to process a trajectory in a relative mode based on code data in order to improve the accuracy of the estimated trajectory.

```
:~$ mm3d TestLib GpsProc './' dgps 15073106.obs
          00012120.15O ct19212z.15n AntBPosType=XYZ
          StaPosFile=Output_static.xml
```

The positioning mode is `dgps`. Here we give as input file `RINEX` raw measurements of the base station(`00012120.15O`). As the position has been estimated in B.2.1, optional arguments `StaPosFile=Output_static.xml` is used to give reference position of the base station and `AntBPosType=XYZ` specifies the format of the given position.

The on-board `GPS` module in the `GéoCube` is a `u-blox LEA-6T-0-001` model. This `GPS` ship allows recording carrier-phase raw measurements. As noise measurement on carrier-phase is much less important than on code measurements, we perform a relative processing based on raw carrier-phase data.

```
:~$ mm3d TestLib GpsProc './' kinematic 15073106.obs
          00012120.15O ct19212z.15n AntBPosType=XYZ
          StaPosFile=Output_static.xml
```

The positioning mode value is `kinematic`. As for previous command, we give reference position of pivot station using optional arguments. Carrier-phase trajectory is stored in `Output_kinematic.xml` and `Output_kinematic.txt` files.

B.3 Processing Photogrammetry Data

B.3.1 Computing Tie Points

`CpleImgs.xml` file is used with the `mm3d Tapioca` command to accelerate tie points extraction. This file contains all pairs of overlapping images. We perform tie points extraction based on images sub-sampled by a factor of 3.

```
:~$ mm3d Tapioca File CpleImgs.xml 1700
```

`mm3d SEL` command allows to visualize matched tie points between 2 images as shown in Figure B.7.

```
:~$ mm3d SEL './' image_002_00069.tif image_002_00070.
   tif KH=NB
```

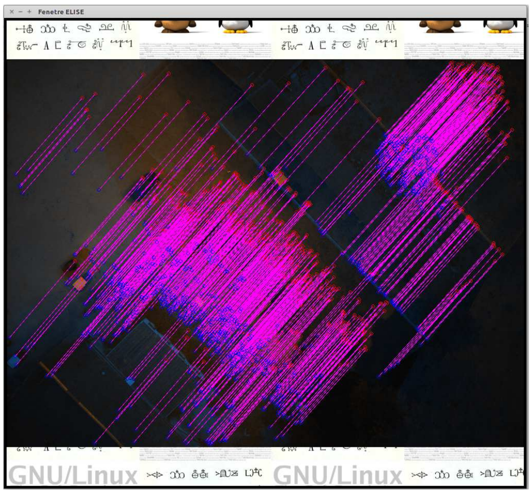

Figure B.2: Tie points visualization using `mm3d SEL` command

Computing Exterior Orientation

To speed up the relative exterior orientation, bloc image is initialized using `mm3d Martini` command adapted for large acquisitions. `mm3d AperiCloud` command is used to export estimated exterior orientation in a `.ply` file format and one can visualize it using the free open-source software `meshlab`. The result is shown in Figure B.3.

```
:~$ mm3d Martini ".*tif"
:~$ mm3d AperiCloud ".*tif" Martini
:~$ meshlab AperiCloud_Martini.ply
```

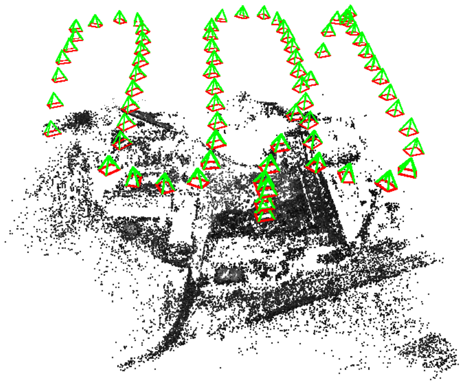

Figure B.3: 3D visualization of exterior orientation

The command `mm3d Tapas` is used to perform relative exterior orientation based on the approximate exterior parameters estimated with `mm3d Martini` command. We use the `RadialStd` camera internal model which has 8 degrees of freedom:

- 1 for focal length
- 2 for principal point
- 2 for distortion center
- 3 for coefficients of radial distortion (r^3,r^5,r^7)

```
:~$ mm3d Tapas RadialStd ".*tif" InOri=Martini
         Out=All-RS
:~$ mm3d AperiCloud ".*tif" All-RS
         ColCadre=[0,0,255]
         ColRay=[255,0,255]
:~$ meshlab AperiCloud_All-RS.ply
```

GPS Positions & Camera Centers Matching

Time synchronization of sensors (camera & `GPS`) was investigated in the laboratory. The electronic delay is negligible ($\sim$ 0.5 ms) and the `GPS` receiver is in charge of triggering the camera. This means that image centers are aligned with `GPS` positions. However, sampling of both trajectories is different. The camera does not have an internal clock (so no time information in `.EXIF` header is available) and camera triggering is not dated in the `GPS` time-scale

(`TimeMark` feature was not available). The matching of corresponding positions is done here by computing the best correlation score of distances ratios curves and by testing all possible time shifts. This is performed using the `mm3d TestLib MatchCenters` command.

```
:~$ mm3d TestLib MatchCenters './' Ori-All-RS/
         Output_single.xml ".*tif"
:~$ mm3d TestLib MatchCenters './' Ori-All-RS/
         Output_dgps.xml ".*tif"
:~$ mm3d TestLib MatchCenters './' Ori-All-RS/
         Output_kinematic.xml ".*tif"
```

Output files (`Ori-Output_single.txt`, ...) contain for each image center the corresponding `GPS` position. Then, the `mm3d OriConvert` command is used to convert output files into the `MicMac` orientation `.XML` format. At the same time, we perform a coordinate system transformation using the optional argument `ChSys`.

```
:~$ mm3d OriConvert "#F=N_X_Y_Z"
        Ori-Output_single.txt Nav-Code
        ChSys=GeoC@SysCoRTL.xml
:~$ mm3d OriConvert "#F=N_X_Y_Z"
         Ori-Output_dgps.txt Nav-DCode
         ChSys=GeoC@SysCoRTL.xml
:~$ mm3d OriConvert "#F=N_X_Y_Z"
         Ori-Output_kinematic.txt Nav-DPhase
         ChSys=GeoC@SysCoRTL.xml
```

At this stage different `GPS` trajectories estimation have been performed. We also have computed exterior orientation based on bundle block adjustment using only tie points observations. For each `GPS` trajectory solution (absolute code, differential code and differential carrier-phase), we have computed correspondences between `GPS` positions and images centers which will allow us to convert the relative exterior orientation into absolute one.

Images Georeferencing

Let's first convert ground points file from `.txt` to `.XML` `MicMac` format using the `mm3d GCPConvert` command and performing at the same time a coordinate system transformation using the optional argument `ChSys`.

```
:~$ mm3d GCPConvert "#F=N_X_Y_Z_Ix_Iy_Iz"
         Pts_GeoC.txt Out=AllPts-RTL.xml
         ChSys=GeoC@SysCoRTL.xml
```

We first start by comparing 3D similarity transformations using different `GPS` estimated trajectories. The command `mm3d CenterBascule` is used to generate absolute exterior orientation, here stored in the folder `Ori-Bascule-RS-XXX/`. Then the command `mm3d GCPCtrl` is used to control ground accuracy by computing residuals on all available ground points here all considered as check points.
First for absolute code measurements estimated trajectory.

```
:~$ mm3d CenterBascule ".*tif" Ori-All-RS/
         Ori-Nav-Code/ Bascule-RS-Code
:~$ mm3d GCPCtrl ".*tif" Bascule-RS-Code
         AllPts-RTL.xml MesImages.xml
```

```
============================= ERRROR MAX PTS FL ======================
   ||    Value=140.12 for Cam=image_002_00100.tif and Pt=7 ; MoyErr=130.967
======================================================================
=== GCP STAT ===  Dist,  Moy=1.52601 Max=1.65398
```

Here for differential code estimated trajectory.

```
:~$ mm3d CenterBascule ".*tif" Ori-All-RS/
         Ori-Nav-DCode/ Bascule-RS-DCode
:~$ mm3d GCPCtrl ".*tif" Bascule-RS-DCode
         AllPts-RTL.xml MesImages.xml
```

```
============================= ERRROR MAX PTS FL ======================
   ||    Value=71.3855 for Cam=image_002_00058.tif and Pt=1 ; MoyErr=53.4976
======================================================================
=== GCP STAT ===  Dist,  Moy=0.640848 Max=0.844784
```

Here for differential carrier-phase estimated trajectory.

```
:~$ mm3d CenterBascule ".*tif" Ori-All-RS/
         Ori-Nav-Dphase/ Bascule-RS-DPhase
:~$ mm3d GCPCtrl ".*tif" Bascule-RS-DPhase
         AllPts-RTL.xml MesImages.xml
```

```
============================= ERRROR MAX PTS FL ======================
   ||    Value=40.8538 for Cam=image_002_00076.tif and Pt=4 ; MoyErr=21.3675
======================================================================
=== GCP STAT ===  Dist,  Moy=0.32083 Max=0.470131
```

We notice after performing the 3 georeferencing computations that the re-projection error is improved by a factor of ∼ 2.5 (for this dataset) when code measurements are used in differential mode (`dgps`). The best georeferencing results are of course obtained using the carrier-phase measurements estimated trajectory which has a mean re-projection error of about 21 pixels.

Bundle Block Adjustment with GPS Positions

We perform here, using the `mm3d Campari` command, a heterogeneous adjustment using tie points and `GPS` camera positions estimated using `GPS` observations. In addition, we take into account the fact that camera optical center and `GPS` antenna phase center are separated by a spatial offset called the lever-arm vector using the optional argument `GpsLa`.

For bundle block adjustment using C/A code positions, planimetric uncertainty is fixed to 3 m and vertical component uncertainty is fixed to 5 m in the optional argument `EmGPS`.

```
:~$ mm3d Campari ".*tif" Ori-Bascule-RS-Code/
          Compense-RS-Code-La GpsLa=[0,0,0]
          EmGPS=[Ori-Nav-Code/,3,5]
:~$ mm3d GCPCtrl ".*tif" Compense-RS-Code-La
          AllPts-RTL.xml MesImages.xml
```

```
LA: [0.263412,0.034836,-2.03753]
============================= ERRROR MAX PTS FL ======================
   ||    Value=212.782 for Cam=image_002_00110.tif and Pt=10 ; MoyErr=195.637
======================================================================
=== GCP STAT ===  Dist,  Moy=2.89733 Max=2.96082
```

For the estimated `GPS` trajectory based on differential code measurements, the planimetric uncertainty is fixed to 0.8 m and vertical component uncertainty is fixed to 1 m.

```
:~$ mm3d Campari ".*tif" Ori-Bascule-RS-DCode/
          Compense-RS-DCode-La GpsLa=[0,0,0]
          EmGPS=[Ori-Nav-DCode/,0.8,1]
:~$ mm3d GCPCtrl ".*tif" Compense-RS-DCode-La
          AllPts-RTL.xml MesImages.xml
```

```
LA: [0.254068,0.106455,-2.40184]
```

```
============================ ERRROR MAX PTS FL ======================
   ||    Value=82.723 for Cam=image_002_00093.tif and Pt=9 ; MoyErr=72.9078
====================================================================
=== GCP STAT ===  Dist,  Moy=1.29547 Max=1.43259
```

For the estimated `GPS` trajectory based on carrier-phase measurements, the planimetric uncertainty is fixed to 1.5 *cm* and vertical component uncertainty is fixed to 2.5 *cm*.

```
:~$ mm3d Campari ".*tif" Ori-Bascule-RS-DPhase/
          Compense-RS-DPhase-La GpsLa=[0,0,0]
          EmGPS=[Ori-Nav-DPhase/,0.015,0.025]
:~$ mm3d GCPCtrl ".*tif" Compense-RS-DPhase-La
          AllPts-RTL.xml MesImages.xml
```

```
LA: [0.10641,-0.0544187,-0.462974]

============================ ERRROR MAX PTS FL ======================
   ||    Value=18.6601 for Cam=image_002_00074.tif and Pt=3 ; MoyErr=12.5342
====================================================================
=== GCP STAT ===  Dist,  Moy=0.282267 Max=0.309341
```

Using all available observations during the bundle block adjustment improves the accuracy for the last `GPS` trajectory, the most accurate one computed on carrier-phase measurements while for trajectories based on code measurements residuals on check points are more important compared to the results of a 3D spatial similarity estimation B.3.1. This is due to the fact that the high uncertainty on code absolute and relative estimated trajectories strongly impacts the estimation of the lever-arm vector during the adjustment.

Advanced Internal Camera Model

High degree distortion polynomial function is used here. While the `RadialStd` model used above contains 3 polynomial coefficients (r^3, r^5, r^7), the `Four15x2` model contains 7 polynomial coefficients $(r^3, \ldots, r^{15})$. The optional argument `DegRadMax=3` means that the first three polynomial coefficients are estimated (in a first step). The optional argument `DegGen=0` means that planimetric systematics we are note taking into account. This several steps strategy is used to initialize internal calibration model avoiding the risk of over-parametrization. From here, we will only use the results of the `GPS` trajectory based on carrier-phase measurements.

```
:~$ mm3d Tapas Four15x2 ".*tif" DegGen=0
         DegRadMax=3 Out=Calib-Four
:~$ mm3d CenterBascule ".*tif" Ori-Calib-Four/
         Ori-Nav-DPhase/ Bascule-CF-DPhase
:~$ mm3d GCPCtrl ".*tif" Bascule-CF-DPhase
         AllPts-RTL.xml MesImages.xml
```

```
============================= ERRROR MAX PTS FL ======================
   ||    Value=19.4863 for Cam=image_002_00076.tif and Pt=4 ; MoyErr=9.30796
======================================================================
=== GCP STAT ===  Dist,  Moy=0.11394 Max=0.221325
```

Then we perform a bundle block adjustment using `GPS` positions.

```
:~$ mm3d Campari ".*tif" Ori-Bascule-CF-DPhase/
         Compense-CF-DPhase-La GpsLa=[0,0,0]
         EmGPS=[Ori-Nav-DPhase/,0.015,0.025]
:~$ mm3d GCPCtrl ".*tif" Compense-CF-DPhase-La
         AllPts-RTL.xml MesImages.xml
```

```
LA: [0.0959945,-0.0505342,-0.360517]

============================= ERRROR MAX PTS FL ======================
   ||    Value=11.8484 for Cam=image_002_00074.tif and Pt=3 ; MoyErr=8.97186
======================================================================
=== GCP STAT ===  Dist,  Moy=0.209958 Max=0.226384
```

For the second stage, we add general parameters of degree 2.

```
:~$ mm3d Tapas Four15x2 ".*tif" InOri=Calib-Four
         DegGen=2 Out=All-F15
:~$ mm3d CenterBascule ".*tif" Ori-All-F15/
         Ori-Nav-DPhase/ Bascule-AF15-DPhase
:~$ mm3d GCPCtrl ".*tif" Bascule-AF15-DPhase
         AllPts-RTL.xml MesImages.xml
```

```
============================= ERRROR MAX PTS FL ======================
   ||    Value=7.62354 for Cam=image_002_00081.tif and Pt=4 ; MoyErr=5.11739
======================================================================
=== GCP STAT ===  Dist,  Moy=0.0659771 Max=0.0942006
```

Then we perform a bundle block adjustment using `GPS` positions.

```
:~$ mm3d Campari ".*tif" Ori-Bascule-AF15-DPhase/
         Compense-AF15-DPhase-La GpsLa=[0,0,0]
         EmGPS=[Ori-Nav-DPhase/,0.015,0.025]
:~$ mm3d GCPCtrl ".*tif" Compense-AF15-DPhase-La
         AllPts-RTL.xml MesImages.xml
```

```
LA: [0.0949466,-0.0561756,-0.261616]
============================= ERRROR MAX PTS FL ======================
   ||    Value=9.8082 for Cam=image_002_00071.tif and Pt=6 ; MoyErr=7.29489
======================================================================
=== GCP STAT ===  Dist,  Moy=0.163896 Max=0.178663
```

For the last stage, we add a general polynomial model. Only residual distortion is estimated to avoid over parametrization issues.

```
:~$ mm3d Tapas AddPolyDeg7 ".*tif" InOri=All-F15
         Out=All-F15-AddP7
:~$ mm3d CenterBascule ".*tif" Ori-All-F15-AddP7/
         Ori-Nav-DPhase/ Bascule-AF15P7-DPhase
:~$ mm3d GCPCtrl ".*tif" Bascule-AF15P7-DPhase
         AllPts-RTL.xml MesImages.xml
```

```
============================= ERRROR MAX PTS FL ======================
   ||    Value=7.1342 for Cam=image_002_00081.tif and Pt=4 ; MoyErr=5.69632
======================================================================
=== GCP STAT ===  Dist,  Moy=0.0932433 Max=0.106558
```

```
:~$ mm3d Campari ".*tif" Ori-Bascule-AF15P7-DPhase/
         Compense-AF15P7-DPhase-La GpsLa=[0,0,0]
         EmGPS=[Ori-Nav-DPhase/,0.015,0.025]
:~$ mm3d GCPCtrl ".*tif" Compense-AF15P7-DPhase-La
         AllPts-RTL.xml MesImages.xml
```

```
LA: [0.094229,-0.0559327,-0.239925]
============================= ERRROR MAX PTS FL ======================
   ||    Value=8.45862 for Cam=image_002_00071.tif and Pt=6 ; MoyErr=6.2671
======================================================================
=== GCP STAT ===  Dist,  Moy=0.138502 Max=0.153681
```

We perform the same adjustment releasing the focal and the principal point as parameters to be re-estimated using optional arguments `FocFree & PPFree`. Since the camera model is build of a large number of parameters, it is not reliable to release all parameters during the bundle adjustment. During next steps, we will use the best absolute exterior orientation estimation `Ori-Compense-AF15P7-DPhase-La/` performing a mean re-projection error of ~ 6 pixels on check points.

```
:~$ mm3d Campari ".*tif" Ori-Bascule-AF15P7-DPhase/
         Compense-AF15P7-DPhase-La GpsLa=[0,0,0]
         EmGPS=[Ori-Nav-DPhase/,0.015,0.025]
         FocFree=true PPFree=true
:~$ mm3d GCPCtrl ".*tif" Compense-AF15P7-DPhase-La
         AllPts-RTL.xml MesImages.xml
```

```
LA: [0.0931686,-0.0576498,-0.148083]
============================= ERRROR MAX PTS FL ======================
   ||    Value=7.36595 for Cam=image_002_00071.tif and Pt=6 ; MoyErr=5.67418
======================================================================
=== GCP STAT ===  Dist,  Moy=0.106254 Max=0.120522
```

Releasing blablabla

Bundle Block Adjustment with GPS Position & 1 GCP

We perform the same processing by releasing the same internal parameters (focal length and principal point) and introducing a constraint using 1 ground control point using the optional argument `GCP`. We start by splinting the file containing all ground points (`AllPts-RTL.xml`) into 2 different files. The first one will contain only 1 point which will be used during the bundle block adjustment as a ground control point and the remaining points will be used as check points for accuracy control.

```
:~$ mm3d TestLib SplitPts ./ AllPts-RTL.xml
         GCPs=[10] OutGCPs=GCP_LA_Calib-RTL.xml
         OutCPs=CPs_LA_Calib-RTL.xml
```

Then we perform a constrained bundle block adjustment using 1 ground control point.

```
:~$ mm3d Campari ".*tif" Ori-Bascule-AF15P7-DPhase/
         Compense-AF15P7-DPhase-La GpsLa=[0,0,0]
         EmGPS=[Ori-Nav-DPhase/,0.015,0.025]
```

```
           FocFree=true PPFree=true
           GCP=[GCP_LA_Calib-RTL.xml,0.1,MesImages.xml
              ,0.5]

mm3d GCPCtrl ".*tif" Compense-AF15P7-DPhase-La
      CPs_LA_Calib-RTL.xml MesImages.xml
```

```
LA: [0.0943014,-0.0574927,-0.146457]
============================= ERRROR MAX PTS FL ======================
   ||    Value=1.84504 for Cam=image_002_00121.tif and Pt=5 ; MoyErr=0.933554
======================================================================
=== GCP STAT ===  Dist,  Moy=0.0124384 Max=0.0270012
```

The value 0.1 is a multiplicative factor of the uncertainty field given in the file `GCP_LA_Calib-RTL.xml` and whose value is fixed to 1 *cm* for planimetric components and 2 *cm* for vertical component. As the number of tie points observations is more important during the adjustment, external measurements should be more weighted in order to constrain the estimation (specially when its number is very low, as here, we have only one GCP measurement). The value of 0.1 means that weight of this measurement is 10 times more important than its physical weight. One can check that with a value of 1 instead of 0.1 the accuracy on check points is two times worse.
We show here that with no prior calibration and with a low-cost GPS receiver, coupled with a photogrammetric quality camera, that it is possible to achieve with only one single ground control point sensor orientation with an accuracy of $\sim$ 1 *px*.

GCPs Indirect Sensor Orientation

We perform here a classical conversion of relative camera poses into absolute ones using (a reduced number) ground control points. We start by spliting gound points into ground control points and check points. (We need at least 3 ground control points).

```
:~$ mm3d TestLib SplitPts ./ AllPts-RTL.xml
          GCPs=[1,4,10,15,17]
          OutGCPs=Reduced_GCPs-RTL.xml
          OutCPs=Reduced_CPs-RTL.xml
```

Here we perfom the similarity transformation using the `mm3d GCPBascule` command:

```
:~$ mm3d GCPBascule ".*tif" Ori-All-F15-AddP7/
          Basc-GCPs-F15-AddP7
          Reduced_GCPs-RTL.xml MesImages.xml

:~$ mm3d GCPCtrl ".*tif" Basc-GCPs-F15-AddP7
          Reduced_CPs-RTL.xml MesImages.xml
```

```
============================ ERRROR MAX PTS FL ======================
   ||    Value=1.01048 for Cam=image_002_00071.tif and Pt=6 ; MoyErr=0.722451
=====================================================================
=== GCP STAT ===  Dist,  Moy=0.00770411 Max=0.0182981
```

We perform a bundle block adjustment using reduced ground control points in the compensation and releasing some internal parameters of the camera.

```
:~$ mm3d Campari ".*tif" Basc-GCPs-F15-AddP7
          Compense-GCPs-F15-AddP7
          FocFree=true PPFree=true
          GCP=[Reduced_GCPs-RTL.xml,1,MesImages.xml,0.5]

:~$ mm3d GCPCtrl ".*tif" Compense-GCPs-F15-AddP7
          Reduced_CPs-RTL.xml MesImages.xml
```

```
============================ ERRROR MAX PTS FL ======================
   ||    Value=0.945775 for Cam=image_002_00071.tif and Pt=6 ; MoyErr=0.706563
=====================================================================
=== GCP STAT ===  Dist,  Moy=0.00779557 Max=0.0187995
```

Dense Matching

First, we export optimal dataset of camera poses, here using GPS measurements, in a .ply format using the `mm3d AperiCloud` command.

```
:~$ mm3d AperiCloud ".*tif"
          Ori-Compense-AF15P7-DPhase-La/
```

Then, with the `mm3d SaisieMasqQT` command, we draw a 3d polygon in order to limit the area of matching.

```
:~$ mm3d SaisieMasqQT AperiCloud_Compense-AF15P7-DPhase-
   La.ply
```

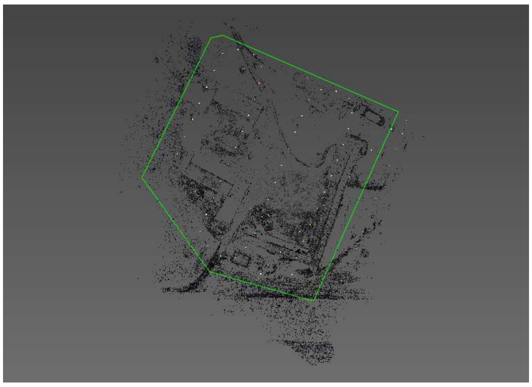

Figure B.4: Drawing a mask

The `mm3d PIMs` command is used to generate the digital surface model using the mode `QuickMac`. The optional arguments `Masq3D` and `FilePair` are used to speed up the processing time cost.

```
:~$ mm3d PIMs QuickMac ".*tif"
            Ori-Compense-AF15P7-DPhase-La/
            Masq3D=AperiCloud_Compense-AF15P7-DPhase-
                La_polyg3d.xml
            FilePair=CpleImgs.xml
```

Orthorectification

We use `mm3d PIMs2Mnt` command to merge the result of the stereo depth maps computed above. The optional argument `DoOrtho` is used to generate individual orthoimages.

```
:~$ mm3d PIMs2Mnt QuickMac DoOrtho=1
```

The orthomosaic image is generated using the `mm3d Tawny` command without performing any radiometric equalization.

```
:~$ mm3d Tawny PIMs-ORTHO/ RadiomEgal=false
```

Figure B.5: Orthoimage

The shading image of depth map is computed using the `mm3d Grshade` command.

```
:~$ mm3d Grshade PIMs-TmpBasc/PIMs-Merged_Prof.tif
             Out=Shading.tif ModeOmbre=IgnE
```

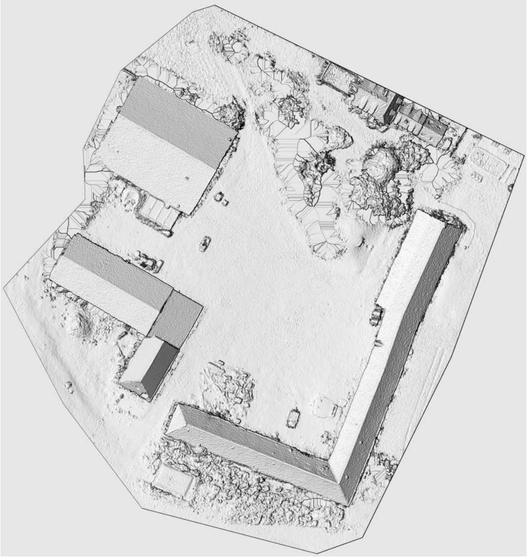

Figure B.6: Shading image

To convert the depth map into a hypsometric representation we use the `mm3d` `to8Bits` command.

```
:~$ mm3d to8Bits PIMs-TmpBasc/PIMs-Merged_Prof.tif
         Out=Hypso.tif Circ=1
```

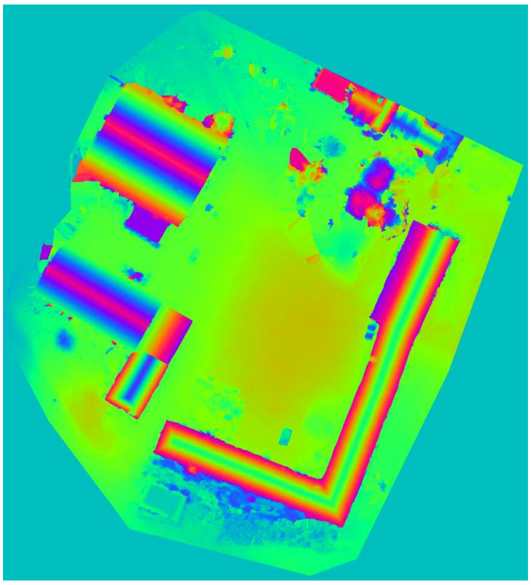

Figure B.7: Hypsometric image

The command `mm3d Nuage2Ply` is used to export a dense points cloud.

```
:~$ mm3d Nuage2Ply PIMs-TmpBasc/PIMs-Merged.xml
         Attr=PIMs-ORTHO/Orthophotomosaic.tif
         RatioAttrCarte=2 Out=GpsNuage.ply
         Scale=1
```

Visualization of the 3d points cloud using `meshlab`.

```
:~$ meshlab GpsNuage.ply
```

Appendix C

Thermal Deformation Workflow

C.1 Presentation of Data

The following link [1] contains a dataset for performing thermal deformation calibration as well as the correction of its effect on an independent photogrammetric dataset. The camera used is the lightweight camera developed at the `IGN`'s `LaSTIG` laboratory within the `LOEMI` instrumentation team. The images are acquired with the monochromatic version of the camera. The `CMOSIS 20000` incorporates a temperature sensor which allows the measurement of temperature value at the time of image acquisition. The value of this temperature is available in the meta-data of the images.

The file `Thm_Proc/Piepline-ThmProc.txt` contains all command lines for performing the calibration and correction of thermal effect on images. Data available in the `Thm_Proc/` folder are organized as follows:

- `Extract_Thm_Data.sh` is a script file to extract temperature data from image header for each pattern of the following folders
- `Calib_Data/` folder contains calibration data
  - a pattern of 76 images in a `.tif` format
  - `MM-DeformThermik.xml` is a `.xml` file modified configuration of the `MicMac` correlator
- `Exp_Data/` folder contains photogrammetric evaluation data
  - a pattern of 28 images in a `.tif` format
  - `Pts_Ter.xml` is a `.xml` file containing GCPs ground measurements
  - `MesImg.xml` is a `.xml` file containing GCPs image measurements
  - `MicMac-LocalChantierDescripteur.xml` is a `.xml` file giving informations about the camera sensor in `MicMac` format

C.2 Extraction of Thermal Measurements

The first command consist of extracting thermal measurements from images header. The first command is launched from `Thm_Proc/` folder as follows:

```
:~$ sh Extract_Thm_Data.sh
```

In each folder (`Calib_Data/` and `Exp_Data/`) a file named `all_name_temp.txt` is created and contains 2 columns. The first corresponds to the name of the image and the second to the temperature of the sensor at image acquisition time.

C.3 Calibration of Thermal Effect

In this part we will focus on the calibration of the thermal effect. The processing will be done in the `Thm_Proc/Calib_Data/` folder.

```
:~$ cd Calib_Data/
```

Figure C.1 shows a sample of calibration images.

Figure C.1: Sample of calibration images acquisition

C.3.1 2D Matching

The first step in the calibration process is the calculation of deformation maps. The first image `img_029_001_00020.thm.tif` is considered as the reference image and for each subsequent image we compute a deformation map by 2D matching. The images are co-registered as the camera is static during acquisition and records an image of the same scene. The only parameter that varies is the temperature of the sensor. The command `mm3d TestLib ThermikProc` automates the call to low-level commands that generally performs a step of the calibration process on a couple of images. We indicate these commands for the interested reader and launch step by step the same `mm3d TestLib ThermikProc` for better comprehension.

The calculation of the deformation maps is carried out by the `mm3d MICMAC` command which takes as argument the configuration file `MM-DeformThermik.xml`. The following command performs this calculation for all the following pairs of images:

- `img_029_001_00020.thm.tif-img_029_001_00120.thm.tif`
- ...
- `img_029_001_00020.thm.tif-img_029_007_07520.thm.tif`

```
:~$ mm3d TestLib ThermikProc ".*tif" DoMEC=1 Clean=1
```

For each pair a folder[1] is created containing deformations maps along each axis. The optional argument `Clean` permits to remove all intermediate results for saving storage space. It is possible to visualize a deformation map using the `mm3d Vino` command. Figure C.3 shows an example for the last pair.

```
:~$ mm3d Vino MEC—img_029_001_00020.thm.tif-
    img_029_007_07520.thm.tif/Px1_Num9_DeZoom1_LeChantier
    .tif
```

Figure C.2: Deformation Map along x axis between a pair of images

---

[1] the format is: `MEC-img_029_001_00020.thm.tif-img_029_007_0XXXX.thm.tif`

It is also possible to compute some statistics on this image using the `mm3d StatIm` command. We notice that the deformation has a range of ∼2.3 pixels.

```
:~$ mm3d StatIm MEC—img_029_001_00020.thm.tif–
    img_029_007_07520.thm.tif/Px1_Num9_DeZoom1_LeChantier
    .tif [0,0] Sz=[5120,3840]
```

```
ZMoy=0.428044 ; Sigma=0.64405
ZMinMax=[-0.61514 , 1.66831]
MoyAbs=0.640813
```

C.3.2 Estimate Analytical Model

In order to estimate an analytical model, all deformation maps must first be converted to the `Homol` format of `MicMac`. This conversion is performed by the `mm3d DMatch2Hom` command for a pair of images. In order to perform this conversion on all available pairs, we use the following command.

```
:~$ mm3d TestLib ThermikProc ".*tif" DoConv2H=1
```

A folder named `HomolDM/` is created which contains all observations (deformation maps) that will be used to estimate the analytical model. The estimation is performed with `mm3d CalcMapXYT` command. This command offers the possibility to choose between different deformation models with more or less degrees of freedom. The available models are the following:

- homothetic transformation
- 2D similarity
- affine
- homography
- polynomial

We use the polynomial model as given in equation (5.2). The following command estimates the deformation model.

```
:~$ mm3d TestLib ThermikProc ".*tif" CmpEvolMap=1
```

First, the command makes a conversion of `all_name_temp.txt` file into (`.xml`) `MicMac` format. The file `MicMac-LocalChantierDescripteur.xml` gives association between image name and its temperature value. The deformation model is saved in `PolOfTXY.xml` file which contains the coefficients of the estimated polynomial function. For each image, statistics on observations residuals are printed and the global mean residual is given.

```
...
Residual, For img_029_004_06020.thm.tif
              moy=0.0246325
              med=0.0204172
              %80=0.0329822
...
*** MOY DIST GLOB = 0.0268955 ***
```

C.4 Correction of Thermal Effect

Once the analytical model estimated based on the calibration data it is possible to correct the thermal effect on images acquired in a photogrammetric acquisition configuration. The purpose is to investigate the improvement of photogrammetric accuracy by taking into account the influence of this parameters.

C.4.1 Estimate Correction Function

The estimation of the correction function, based on the analytical model and on temperature values measured for the photogrammetric dataset, is performed with the `mm3d CalcMapOfT` command. To compute the correction for all images we will use the following command.

```
:~$ mm3d TestLib ThermikProc ".*tif"
          PatToCorr="../Exp_Data/.*tif"
```

For each value of temperature of evaluation data images, a `.xml` file named `Deg_XX.000000.xml` is created. These files contain the correction function to apply to image observations for each respective image.

C.4.2 Photogrammetric Processing

As a first step, we will process raw images in order to calculate the accuracy which can be reached without applying any correction. A standard processing worflow is adopted consisting of:

1. extraction tie points using a specific strategy
2. estimating relative exterior orientation,
3. converting relative exterior orientation to absolute one using GCPs
4. evaluate residuals on GCPs

The following processing is performed in the evaluation data folder.

```
:~$ cd ../Exp_Data/
```

C.4.2.1 Tie Points Extraction

The tie points extraction is realized with the `mm3d Tapioca` command. We perform this calculation at full image resolution. In order to better evaluate the influence of temperature, as the acquisition is circular, we calculate tie points by taking into account this geometry using the option `Line` of `mm3d Tapioca`. Furthermore, we do not calculate tie points between the first and last images as optional argument is set to `Circ=0`. In this way, the acquisition is of type of a single strip one. This particular configuration allows to highlight bowl effect and maximizes the effects of accumulated errors.

```
:~$ mm3d Tapioca Line ".*tif" -1 5 Circ=0
```

C.4.2.2 Exterior Orientation

Bundle block adjustment is performed with the `mm3d Tapas` command. The camera model adopted is the `RadilaStd` one which has 8 degree of freedom as presented in Section B.3.1. The exterior orientation is converted to `.ply` format and can be visualized with `meshlab` software.

```
:~$ mm3d Tapas RadialStd ".*tif" Out=Raw
:~$ mm3d AperiCloud ".*tif" Ori-Raw/
:~$ meshlab AperiCloud_Raw.ply
```

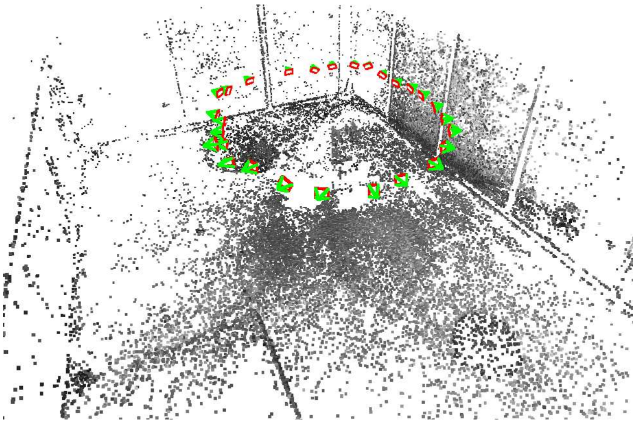

Figure C.3: Geometry of acquisition

C.4.2.3 Indirect Sensor Orientation

Indirect sensor orientation is performed with the `mm3d GCPBascule` command.

```
:~$ mm3d GCPBascule ".*tif" Ori-Raw/ Basc-Raw
         Pts_Ter.xml MesImgs.xml
```

C.4.2.4 Accuracy Control

Accuracy control on `GCPs` is performed with the `mm3d GCPControl` command.

```
:~$ mm3d GCPCtrl ".*tif" Ori-Basc-Raw/ Pts_Ter.xml
         MesImgs.xml
```

C.4.2.5 Image Measurements Correction

In a second step, performing thermal correction is realized by correction image measurements using estimated correction function. First we correct tie points coordinates with the command `mm3d Testlib ReechHomol` as follows.

```
:~$ mm3d Testlib ReechHomol './' Homol/
         all_name_temp.txt
```

The folder `Homol_Reech/` is created containing corrected tie points coordinates. Afterwards, `GCPs` image measurements are also corrected using `mm3d TestLib ReechMAF`.

```
:~$ mm3d TestLib ReechMAF MesImgs.xml
         all_name_temp.txt
```

The file `ReechMAF.xml` is created and contain image coordinate of each `GCP` corrected for each image taking into account its temperature.

C.4.2.6 Exterior Orientation (corrected data)

Bundle block adjustment is performed with the `mm3d Tapas` command. The same camera internal model is used for both raw and corrected images. The folder containing corrected tie points is specified with the optional argument `SH`.

```
:~$ mm3d Tapas RadialStd ".*tif" Out=Corr SH=_Reech
```

C.4.2.7 Indirect Sensor Orientation (corrected data)

Indirect sensor orientation is performed with the `mm3d GCPBascule` command.

```
:~$ mm3d GCPBascule ".*tif" Ori-Corr/ Basc-Corr
         Pts_Ter.xml ReechMAF.xml
```

C.4.2.8 Accuracy Control (corrected data)

Accuracy control on `GCPs` is performed with the `mm3d GCPControl` command.

```
:~$ mm3d GCPCtrl ".*tif" Basc-Corr Pts_Ter.xml
         ReechMAF.xml
```

Bibliography

[Arya *et al.* 1998] Sunil Arya, David M. Mount, Nathan S. Netanyahu, Ruth Silverman and Angela Y. Wu. *An Optimal Algorithm for Approximate Nearest Neighbor Searching Fixed Dimensions.* J. ACM, vol. 45, no. 6, pages 891–923, November 1998. (Cited on page 99.)

[Audi *et al.* 2017] Ahmad Audi, Marc Pierrot-Deseilligny, Christophe Meynard and Christian Thom. *Implementation of an IMU Aided Image Stacking Algorithm in a Digital Camera for Unmanned Aerial Vehicles.* Sensors, vol. 17, no. 7, 2017. (Cited on page 52.)

[Bendea *et al.* 2008] H Bendea, Piero Boccardo, S Dequal, Fabio Giulio Tonolo, Davide Marenchino and Marco Piras. *Low cost UAV for post-disaster assessment.* ISPRS - International Archives of the Photogrammetry, Remote Sensing and Spatial Information Sciences, vol. 37, no. Part B, pages 1373–1379, 2008. (Cited on page 48.)

[Benoit *et al.* 2015] L. Benoit, P. Briole, O. Martin, C. Thom, J.-P. Malet and P. Ulrich. *Monitoring landslide displacements with the Geocube wireless network of low-cost GPS.* Engineering Geology, vol. 195, pages 111 – 121, 2015. (Cited on page 53.)

[Benoit 2014] Lionel Benoit. *Positionnement GPS précis et en temps-réel dans le contexte de réseaux de capteurs sans fil type Geocube : application à des objets géophysiques de taille kilométrique.* PhD thesis, École Normale Supérieure, 2014. (Cited on page 36.)

[Bláha *et al.* 2011] M. Bláha, H. Eisenbeiss, D. Grimm and P. Limpach. *Direct Georeferencing of UAVS.* ISPRS - International Archives of the Photogrammetry, Remote Sensing and Spatial Information Sciences, vol. XXXVIII-1/C22, pages 131–136, 2011. (Cited on page 48.)

[Blázquez & Colomina 2012] Marta Blázquez and Ismael Colomina. *On INS/GNSS-based time synchronization in photogrammetric and remote sensing multi-sensor systems.* Photogrammetrie-Fernerkundung-Geoinformation, vol. 2012, no. 2, pages 91–104, 2012. (Cited on page 80.)

[Blázquez 2008] M Blázquez. *A new approach to spatio-temporal calibration of multi-sensor systems.* In ISPRS Congress, International Archives of the

Photogrammetry, Remote Sensing and Spatial Information Sciences, Beijing, China, pages 481–486, 2008. (Cited on page 80.)

[Blázquez & Colomina 2012] M. Blázquez and I. Colomina. *Relative INS/GNSS aerial control in integrated sensor orientation: Models and performance.* ISPRS Journal of Photogrammetry and Remote Sensing, vol. 67, pages 120 – 133, 2012. (Cited on page 47.)

[Brabant 2003] Michel Brabant. Maîtriser la topographie : des observations au plan. Eyrolles, 2003. (Cited on page 35.)

[Chalko 2007] Thomas J Chalko. *High accuracy speed measurement using GPS (Global Positioning System).* NU Journal of Discovery, vol. 4, pages 1–9, 2007. (Cited on page 80.)

[Chiang *et al.* 2012] Kai-Wei Chiang, Meng-Lun Tsai and Chien-Hsun Chu. *The Development of an UAV Borne Direct Georeferenced Photogrammetric Platform for Ground Control Point Free Applications.* Sensors, vol. 12, no. 7, page 9161, 2012. (Cited on page 48.)

[CloudCompare (version 2.6.0) [GPL software] 2016] CloudCompare (version 2.6.0) [GPL software]. `http://www.cloudcompare.org/`, 2016. (Accessed 03 August, 2016). (Cited on page 90.)

[CMOSIS 2013] CMOSIS. *Application note for CMV - Temperature Sensor Calibration*, 2.1 édition, 08 2013. (Cited on page 52.)

[CMOSIS 2015] CMOSIS. *20 Megapixel global shutter CMOS image sensor - Datasheet*, 01 édition, 06 2015. (Cited on page 51.)

[Colomina & Molina 2014] I. Colomina and P. Molina. *Unmanned aerial systems for photogrammetry and remote sensing: A review.* ISPRS Journal of Photogrammetry and Remote Sensing, vol. 92, pages 79 – 97, 2014. (Cited on page 48.)

[Colomina 1993] I Colomina. *A note on the analytics of aerial triangulation with GPS aerial control.* Photogrammetric engineering and remote sensing, vol. 59, no. 11, pages 1619–1624, 1993. (Cited on page 47.)

[Colomina 1999] Ismael Colomina. *GPS, INS and Aerial Triangulation: What is the Best Way for the Operational Determination of Photogrammetric Image Orientation?* International Archives of Photogrammetry and Remote Sensing, vol. 32, no. 3; SECT 2W5, pages 121–130, 1999. (Cited on page 47.)

[Colomina 2007] I Colomina. *From off-line to on-line geocoding: the evolution of sensor orientation.* In Photogrammetric Week, Stuttgart, pages 173–183, 2007. (Cited on page 47.)

[Cramer *et al.* 2013] M. Cramer, S. Bovet, M. Gültlinger, E. Honkavaara, A. McGill, M. Rijsdijk, M. Tabor and V. Tournadre. *On the use of RPAS in national mapping ; the EUROSDR point of view.* ISPRS - International Archives of the Photogrammetry, Remote Sensing and Spatial Information Sciences, vol. XL-1/W2, pages 93–99, 2013. (Cited on page 21.)

[Cucci *et al.* 2017] Davide Antonio Cucci, Martin Rehak and Jan Skaloud. *Bundle adjustment with raw inertial observations in UAV applications.* ISPRS Journal of Photogrammetry and Remote Sensing, vol. 130, pages 1 – 12, 2017. (Cited on page 48.)

[Daakir *et al.* 2015] M. Daakir, M. Pierrot-Deseilligny, P. Bosser, F. Pichard and C. Thom. *UAV onboard photogrammetry and GPS positionning for earthworks.* ISPRS - International Archives of the Photogrammetry, Remote Sensing and Spatial Information Sciences, vol. XL-3/W3, pages 293–298, 2015. (Cited on page 65.)

[Daakir *et al.* 2016] M. Daakir, M. Pierrot-Deseilligny, P. Bosser, F. Pichard, C. Thom and Y. Rabot. *Study of lever-arm effect using embedded photogrammetry and on-board GPS receiver on UAV for metrological mapping purpose and proposal of a free ground measurements calibration procedure.* ISPRS - International Archives of the Photogrammetry, Remote Sensing and Spatial Information Sciences, vol. XL-3/W4, pages 65–70, 2016. (Cited on page 65.)

[Daakir *et al.* 2017] M. Daakir, M. Pierrot-Deseilligny, P. Bosser, F. Pichard, C. Thom, Y. Rabot and O. Martin. *Lightweight UAV with on-board photogrammetry and single-frequency GPS positioning for metrology applications.* ISPRS Journal of Photogrammetry and Remote Sensing, vol. 127, pages 115 – 126, 2017. Geospatial Week 2015. (Cited on page 52.)

[DJI Innovations 2014] DJI Innovations. *WooKong-M Quick Start Guide.* `http://dl.djicdn.com/downloads/wkm/en/WooKong-M_Quick_Start_Guide_v1.14_en.pdf`, 2014. (Accessed 03 August, 2016). (Cited on page 54.)

[DJI Innovations 2015a] DJI Innovations. *FlameWheel 550 User Manual.* `http://dl.djicdn.com/downloads/flamewheel/en/F550_User_`

`Manual_v2.0_en.pdf`, 2015. (Accessed 03 August, 2016). (Cited on page 54.)

[DJI Innovations 2015b] DJI Innovations. *Ground Station Wireless Data-link User Manual.* `http://dl.djicdn.com/downloads/groundstation/en/Ground_Station_User_Manual_en_v3.04.pdf`, 2015. (Accessed 03 August, 2016). (Cited on page 54.)

[Duane 1971] C Brown Duane. *Close-range camera calibration.* Photogramm. Eng, vol. 37, no. 8, pages 855–866, 1971. (Cited on page 41.)

[Eisenbeiß 2004] Henri Eisenbeiß. *A mini unmanned aerial vehicle (UAV): system overview and image acquisition.* International Archives of Photogrammetry. Remote Sensing and Spatial Information Sciences, vol. 36, no. 5/W1, 2004. (Cited on page 47.)

[Eisenbeiß 2009] Henri Eisenbeiß. *UAV photogrammetry.* PhD thesis, Institut für Geodesie und Photogrammetrie, ETH-Zürich. Zürich, Switzerland, 2009. (Cited on pages 17, 19 and 48.)

[Fiedler & Müller 2013] David Fiedler and Heinrich Müller. Impact of thermal and environmental conditions on the kinect sensor, pages 21–31. Springer Berlin Heidelberg, Berlin, Heidelberg, 2013. (Cited on page 43.)

[Fischler & Bolles 1987] Martin A Fischler and Robert C Bolles. *Random sample consensus: a paradigm for model fitting with applications to image analysis and automated cartography.* In Readings in computer vision, pages 726–740. Elsevier, 1987. (Cited on page 45.)

[Francois Gervaix 2017] Yannick Gasser Francois Gervaix. *The senseFly S.O.D.A. genesis.* Presented at UAV Metric Camera Special Sessions DGPF Annual Meeting 2017 - Würzburg, Germany, March 8-10 2017. (Cited on page 50.)

[Fraser 1997] Clive S Fraser. *Digital camera self-calibration.* ISPRS Journal of Photogrammetry and Remote sensing, vol. 52, no. 4, pages 149–159, 1997. (Cited on pages 41 and 99.)

[Grenzdörffer *et al.* 2008] GJ Grenzdörffer, A Engel and B Teichert. *The photogrammetric potential of low-cost UAVs in forestry and agriculture.* The International Archives of the Photogrammetry, Remote Sensing and Spatial Information Sciences, vol. 31, no. B3, pages 1207–1214, 2008. (Cited on page 47.)

[Grussenmeyer & Al Khalil 2002] Pierre Grussenmeyer and Omar Al Khalil. *Solutions for exterior orientation in photogrammetry: a review.* The photogrammetric record, vol. 17, no. 100, pages 615–634, 2002. (Cited on page 44.)

[Grussenmeyer 2016] Pierre Grussenmeyer. *Photogrammétrie : bilan et perspectives de 150 années d'histoires*, mars 2016. (Cited on page 40.)

[Hothmer 1958] J. Hothmer. *Possibilities and Limitations for Elimination of Distortion in Aerial Photographs.* The Photogrammetric Record, vol. 2, no. 12, pages 426–445, 1958. (Cited on page 43.)

[Jacobsen 2007] Karsten Jacobsen. *Geometric handling of large size digital airborne frame camera images.* Optical 3D Measurement Techniques VIII, Zürich, vol. 2007, pages 164–171, 2007. (Cited on page 42.)

[James & Robson 2014a] Mike R. James and Stuart Robson. *Mitigating systematic error in topographic models derived from UAV and ground-based image networks.* Earth Surface Processes and Landforms, vol. 39, no. 10, pages 1413–1420, 2014. (Cited on page 63.)

[James & Robson 2014b] Mike R James and Stuart Robson. *Mitigating systematic error in topographic models derived from UAV and ground-based image networks.* Earth Surface Processes and Landforms, vol. 39, no. 10, pages 1413–1420, 2014. (Cited on page 114.)

[Klaas Pauly 2017] Bastien Mancini Klaas Pauly Jean-François Aumont. *From off-the-shelf to off-the-charts: shifting the camera paradigm in commercial fixed wing UAS to increase accuracy.* Presented at UAV Metric Camera Special Sessions DGPF Annual Meeting 2017 - Würzburg, Germany, March 8-10 2017. (Cited on page 50.)

[Klobuchar 1987] J. A. Klobuchar. *Ionospheric Time-Delay Algorithm for Single-Frequency GPS Users.* IEEE Transactions on Aerospace and Electronic Systems, vol. AES-23, no. 3, pages 325–331, May 1987. (Cited on page 36.)

[Kölbl 1976] Otto R Kölbl. *Metric or non-metric cameras.* Photogrammetric Engineering and Remote Sensing, vol. 42, no. 1, pages 103–113, 1976. (Cited on page 42.)

[Kraft *et al.* 2016] Thomas Kraft, Matthias Gessner, Henry Meißner, Michael Cramer, Heinz-Jürgen Przybilla, Markus Gerke*et al.* *Evaluation of* *a Metric Camera System Tailored for High Precision UAV Applications.* International Archives of the Photogrammetry, Remote Sensing and Spatial Information Sciences-ISPRS Archives, 2016. (Cited on page 50.)

[Kraft *et al.* 2017] Thomas Kraft, Henry Meißner, Ralf Berger and Karsten Stebner. *Preliminary results of developing a metric aerial camera for UAV applications.* Presented at UAV Metric Camera Special Sessions DGPF Annual Meeting 2017 - Würzburg, Germany, March 8-10 2017. (Cited on page 50.)

[Lichti *et al.* 2008] Derek Lichti, Jan Skaloud and Philipp Schaer. *On the calibration strategy of medium format cameras for direct georeferencing.* In International Calibration and Orientation Workshop EuroCOW, number TOPO-PRESENTATION-2008-001, 2008. (Cited on page 122.)

[Lin *et al.* 2010] Dong-Long Lin, Ching-Chun Wang and Chia-Ling Wei. *Quantified temperature effect in a CMOS image sensor.* IEEE Transactions on Electron Devices, vol. 57, no. 2, pages 422–428, 2010. (Cited on page 43.)

[Lisein *et al.* 2013] Jonathan Lisein, Marc Pierrot-Deseilligny, Stéphanie Bonnet and Philippe Lejeune. *A photogrammetric workflow for the creation of a forest canopy height model from small unmanned aerial system imagery.* Forests, vol. 4, no. 4, pages 922–944, 2013. (Cited on page 47.)

[Lisein 2016] Jonathan Lisein. *UAV Photogrammetry applied to the characterization of forest ecosystem ressources.* Theses, Université Paris-Est, December 2016. (Cited on pages 13 and 18.)

[Lowe 2004] David G. Lowe. *Distinctive Image Features from Scale-Invariant Keypoints.* International Journal of Computer Vision, vol. 60, no. 2, pages 91–110, 2004. (Cited on page 99.)

[Martin *et al.* 2014] O Martin, C Meynard, M Pierrot-Deseilligny, JP Souchon and C Thom. *Réalisation d'une caméra photogrammétrique ultra légère et haute résolution.* `https://drone.teledetection.fr/articles/Souchon_CAMLIGHT_IGN_rev.pdf`, 2014. (Accessed 07 December, 2016). (Cited on page 51.)

[Mcglone *et al.* 1980] Chris Mcglone, Edward Mikhail and Jim Bethel. Manual of Photogrammetry. American Society of Photogrammetry, 5th édition, 1980. (Cited on page 42.)

[Meier *et al.* 2011] L. Meier, P. Tanskanen, F. Fraundorfer and M. Pollefeys. *PIXHAWK: A system for autonomous flight using onboard computer vision.* In 2011 IEEE International Conference on Robotics and Automation, pages 2992–2997, May 2011. (Cited on page 24.)

[Meier *et al.* 2012] Lorenz Meier, Petri Tanskanen, Lionel Heng, Gim Hee Lee, Friedrich Fraundorfer and Marc Pollefeys. *PIXHAWK: A micro aerial vehicle design for autonomous flight using onboard computer vision.* Autonomous Robots, vol. 33, no. 1, pages 21–39, Aug 2012. (Cited on page 24.)

[Merchant 2006] Dean C Merchant. *Influence of temperature on focal length for the airborne camera.* In Proc. of MAPPS/ASPRS Fall Conference, 2006. (Cited on pages 43, 104 and 121.)

[Merchant 2012] Dean C Merchant. *Aerial Camera Metric Calibration—History and Status.* In Proceedings of ASPRS 2012 Annual Conference, Sacramento, Calif, 2012. (Cited on pages 43, 104 and 121.)

[Mian *et al.* 2015] O. Mian, J. Lutes, G. Lipa, J. J. Hutton, E. Gavelle and S. Borghini. *Direct georeferencing on small unmanned aerial platforms for improved reliability and accuracy of mapping without the need for ground control points.* ISPRS - International Archives of the Photogrammetry, Remote Sensing and Spatial Information Sciences, vol. XL-1/W4, pages 397–402, 2015. (Cited on page 48.)

[Moulon 2014] Pierre Moulon. *Robust and accurate calibration of camera networks.* Theses, Université Paris-Est, January 2014. (Cited on pages 14 and 45.)

[Nex & Remondino 2014] Francesco Nex and Fabio Remondino. *UAV for 3D mapping applications: a review.* Applied Geomatics, vol. 6, no. 1, pages 1–15, Mar 2014. (Cited on page 50.)

[Niethammer *et al.* 2012] U. Niethammer, M.R. James, S. Rothmund, J. Travelletti and M. Joswig. *UAV-based remote sensing of the Super-Sauze landslide: Evaluation and results.* Engineering Geology, vol. 128, pages 2 – 11, 2012. Integration of Technologies for Landslide Monitoring and Quantitative Hazard Assessment. (Cited on page 47.)

[Pfeifer *et al.* 2012] N. Pfeifer, P. Glira and C. Briese. *Direct georeferencing with on board navigation componants of light weight UAV platforms.*

ISPRS - International Archives of the Photogrammetry, Remote Sensing and Spatial Information Sciences, vol. XXXIX-B7, pages 487–492, 2012. (Cited on page 48.)

[Pierrot-Deseilligny & Clery 2011] M. Pierrot-Deseilligny and I. Clery. *APERO, an open source Bundle Adjustement software for automatic calibration and orientation of set of images.* ISPRS - International Archives of the Photogrammetry, Remote Sensing and Spatial Information Sciences, vol. XXXVIII-5/W16, pages 269–276, 2011. (Cited on page 44.)

[Pierrot-Deseilligny & Paparoditis 2006] Marc Pierrot-Deseilligny and Nicolas Paparoditis. *A multiresolution and optimization-based image matching approach: An application to surface reconstruction from SPOT5-HRS stereo imagery.* Archives of Photogrammetry, Remote Sensing and Spatial Information Sciences, vol. 36, no. 1/W41, 2006. (Cited on page 96.)

[Pierrot-Deseilligny 2017] Marc Pierrot-Deseilligny. *MicMac, Apero, Pastis and Other Beverages in a Nutshell!* `https://github.com/micmacIGN/Documentation/blob/master/DocMicMac.pdf`, 2017. (Accessed 05 October, 2017). (Cited on pages 46 and 57.)

[Rehak & Skaloud 2015] M. Rehak and J. Skaloud. *Fixed-Wing Micro Aerial Vehicle for Accurate Corridor Mapping.* ISPRS Annals of Photogrammetry, Remote Sensing and Spatial Information Sciences, vol. II-1/W1, pages 23–31, 2015. (Cited on page 64.)

[Rehak & Skaloud 2016] M. Rehak and J. Skaloud. *Applicability of New Approaches of Sensor Orientation to Micro Aerial Vehicles.* ISPRS Annals of Photogrammetry, Remote Sensing and Spatial Information Sciences, vol. III-3, pages 441–447, 2016. (Cited on page 48.)

[Rehak & Skaloud 2017a] M. Rehak and J. Skaloud. *Performance assessment of Integrated Sensor Orientation with a Low-Cost GNSS receiver.* ISPRS Annals of Photogrammetry, Remote Sensing and Spatial Information Sciences, vol. IV-2/W3, pages 75–80, 2017. (Cited on page 48.)

[Rehak & Skaloud 2017b] M. Rehak and J. Skaloud. *Time synchronization of consumer cameras on Micro Aerial Vehicles.* ISPRS Journal of Photogrammetry and Remote Sensing, vol. 123, no. Supplement C, pages 114 – 123, 2017. (Cited on page 77.)

[Rehak *et al.* 2013] M. Rehak, R. Mabillard and J. Skaloud. *A Micro-UAV with the capability of Direct Georeferencing.* ISPRS - International Archives of the Photogrammetry, Remote Sensing and Spatial Information Sciences, vol. XL-1/W2, pages 317–323, 2013. (Cited on page 48.)

[Remondino & Fraser 2006] Fabio Remondino and Clive Fraser. *Digital camera calibration methods: considerations and comparisons.* International Archives of Photogrammetry, Remote Sensing and Spatial Information Sciences, vol. 36, no. 5, pages 266–272, 2006. (Cited on page 95.)

[Remondino *et al.* 2011] Fabio Remondino, L Barazzetti, Francesco Nex, Marco Scaioni and Daniele Sarazzi. *UAV photogrammetry for mapping and 3d modeling–current status and future perspectives.* International Archives of the Photogrammetry, Remote Sensing and Spatial Information Sciences, vol. 38, no. 1, page C22, 2011. (Cited on page 47.)

[Remondino *et al.* 2012] Fabio Remondino, Silvio Del Pizzo, Thomas P. Kersten and Salvatore Troisi. *Low-Cost and Open-Source Solutions for Automated Image Orientation – A Critical Overview.* In Marinos Ioannides, Dieter Fritsch, Johanna Leissner, Rob Davies, Fabio Remondino and Rossella Caffo, editors, Progress in Cultural Heritage Preservation, pages 40–54, Berlin, Heidelberg, 2012. Springer Berlin Heidelberg. (Cited on page 44.)

[Rieke *et al.* 2011] Matthes Rieke, Theodor Foerster, Jakob Geipel and Torsten Prinz. *High-precision positioning and real-time data processing of UAV-systems.* International Archives of Photogrammetry, Remote Sensing and Spatial Information Sciences, vol. 38, pages 1–C22, 2011. (Cited on page 48.)

[Rosu *et al.* 2015] Ana-Maria Rosu, Marc Pierrot-Deseilligny, Arthur Delorme, Renaud Binet and Yann Klinger. *Measurement of ground displacement from optical satellite image correlation using the free open-source software MicMac.* ISPRS Journal of Photogrammetry and Remote Sensing, vol. 100, pages 48 – 59, 2015. High-Resolution Earth Imaging for Geospatial Information. (Cited on page 96.)

[Rupnik *et al.* 2017] Ewelina Rupnik, Mehdi Daakir and Marc Pierrot Deseilligny. *MicMac – a free, open-source solution for photogrammetry.* Open Geospatial Data, Software and Standards, vol. 2, no. 1, page 14, 2017. (Cited on pages 14, 56 and 57.)

[Saastamoinen 1972] J Saastamoinen. *Atmospheric correction for the troposphere and stratosphere in radio ranging satellites.* The use of artificial satellites for geodesy, pages 247–251, 1972. (Cited on page 36.)

[Sauer 2001] Donald Jon Sauer. *CMOS image sensor with reduced fixed pattern noise*, November 20 2001. US Patent 6,320,616. (Cited on page 43.)

[Schwartz 2010] Joerg Schwartz. *New CMOS image sensor is useful in extreme temperatures*, 2010. (Cited on page 43.)

[Skaloud *et al.* 1996] J Skaloud, M Cramer and KP Schwarz. *Exterior orientation by direct measurement of camera position and attitude.* International Archives of Photogrammetry and Remote Sensing, vol. 31, no. B3, pages 125–130, 1996. (Cited on page 47.)

[Skaloud *et al.* 2014] J. Skaloud, M. Rehak and D. Lichti. *Mapping with MAV: Experimental Study on the Contribution of Absolute and Relative Aerial Position Control.* ISPRS - International Archives of the Photogrammetry, Remote Sensing and Spatial Information Sciences, vol. XL-3/W1, pages 123–129, 2014. (Cited on page 48.)

[Skaloud 1999] Jan Skaloud. Optimizing georeferencing of airborne survey systems by ins/dgps. University of Calgary, 1999. (Cited on page 47.)

[Skaloud 2002] Jan Skaloud. *Direct georeferencing in aerial photogrammetric mapping.* Photogrammetric Engineering and Remote Sensing, vol. 68, no. 3, 2002. (Cited on page 47.)

[Smith & Cope 2010] MJ Smith and E Cope. *The effects of temperature variation on single-lens-reflex digital camera calibration parameters.* International Archives of Photogrammetry, Remote Sensing and Spatial Information Sciences, vol. 38, no. Part 5, 2010. (Cited on page 43.)

[Stempfhuber & Buchholz 2011] W. Stempfhuber and M. Buchholz. *A precise, Low-Cost RTK GNSS system for UAV applications.* ISPRS - International Archives of the Photogrammetry, Remote Sensing and Spatial Information Sciences, vol. XXXVIII-1/C22, pages 289–293, 2011. (Cited on page 48.)

[Subirana *et al.* 2013] J Sanz Subirana, JM Juan Zornoza and M Hernández-Pajares. *GNSS Data processing. Volume 1: Fundamentals and Algorithms.* Technical report, ESA TM-23/1. ESA Communications, 2013. (Cited on page 58.)

[Takasu & Yasuda 2008] Tomoji Takasu and Akio Yasuda. *Evaluation of RTK-GPS performance with low-cost single-frequency GPS receivers.* In Proceedings of international symposium on GPS/GNSS, pages 852–861, 2008. (Cited on page 58.)

[Takasu & Yasuda 2009] Tomoji Takasu and Akio Yasuda. *Development of the low-cost RTK-GPS receiver with an open source program package RTKLIB.* In international symposium on GPS/GNSS, pages 4–6. International Convention Centre Jeju, Korea, 2009. (Cited on page 57.)

[Tang *et al.* 2012] Rongfu Tang, Dieter Fritsch and Michael Cramer. *New rigorous and flexible Fourier self-calibration models for airborne camera calibration.* ISPRS journal of photogrammetry and remote sensing, vol. 71, pages 76–85, 2012. (Cited on page 42.)

[Tang 2013] Rongfu Tang. *Mathematical methods for camera self-calibration in photogrammetry and computer vision.* PhD thesis, University of Stuttgart, 2013. (Cited on page 64.)

[Tomoji 2013] Takasu Tomoji. *RTKLIB ver.2.4.2 Manual.* `http://www.rtklib.com/prog/manual_2.4.2.pdf`, 2013. (Accessed 05 October, 2016). (Cited on pages 57 and 59.)

[Tournadre *et al.* 2014] V. Tournadre, M. Pierrot-Deseilligny and P. H. Faure. *UAV photogrammetry to monitir dykes - calibration and comparison to terrestrialLIDAR.* ISPRS - International Archives of the Photogrammetry, Remote Sensing and Spatial Information Sciences, vol. XL-3/W1, pages 143–148, 2014. (Cited on page 47.)

[Tournadre *et al.* 2015] V. Tournadre, M. Pierrot-Deseilligny and P. H. Faure. *UAV linear photogrammetry.* ISPRS - International Archives of the Photogrammetry, Remote Sensing and Spatial Information Sciences, vol. XL-3/W3, pages 327–333, 2015. (Cited on page 63.)

[Tournadre 2015] Vincent Tournadre. *Métrologie par photogrammétrie aéroportée légère : application au suivi d'évolution de digues.* PhD thesis, Université Paris-Est, 2015. Thèse de doctorat dirigée par Pierrot-Deseilligny, Marc Signal, Image, Automatique Paris Est 2015. (Cited on page 51.)

[Triggs *et al.* 1999] Bill Triggs, Philip F McLauchlan, Richard I Hartley and Andrew W Fitzgibbon. *Bundle adjustment - a modern synthesis.* In International workshop on vision algorithms, pages 298–372. Springer, 1999. (Cited on page 45.)

[Turner *et al.* 2014] David Turner, Arko Lucieer and Luke Wallace. *Direct georeferencing of ultrahigh-resolution UAV imagery.* Geoscience and Remote Sensing, IEEE Transactions on, vol. 52, no. 5, pages 2738–2745, 2014. (Cited on page 48.)

[u-blox 2013] u-blox. *u-blox 6 Receiver Description Including Protocol Specification.* `https://www.u-blox.com/sites/default/files/products/documents/u-blox6_ReceiverDescrProtSpec_%28GPS.G6-SW-10018%29_Public.pdf?utm_source=en%2Fimages%2Fdownloads%2FProduct_Docs%2Fu-blox6_ReceiverDescriptionProtocolSpec_%28GPS.G6-SW-10018%29.pdf`, 2013. (Accessed 03 August, 2016). (Cited on page 53.)

[u-blox 2015] u-blox. *LEA-6 u-blox 6 GPS Modules Data Sheet Objective Specification.* `https://www.u-blox.com/sites/default/files/products/documents/LEA-6_DataSheet_(UBX-14044797).pdf`, 2015. (Accessed 03 August, 2016). (Cited on page 53.)

[u-blox 2016] u-blox. *u-center GNSS evaluation software for Windows User Guide.* `https://www.u-blox.com/sites/default/files/u-Center_UserGuide_(UBX-13005250).pdf`, 2016. (Accessed 03 August, 2016). (Cited on page 77.)

[Vallet & Skaloud 2004] Julien Vallet and Jan Skaloud. *Development and experiences with a fully-digital handheld mapping system operated from a helicopter.* International Archives of the Photogrammetry, Remote Sensing and Spatial Information Sciences, vol. 35, pages 1–6, 2004. (Cited on page 76.)

[Vallet 2002] Julien Vallet. *Saisie de la couverture neigeuse de sites avalancheux par des systèmes aéroportés.* 2002. (Cited on page 38.)

[Vallet 2007] Julien Vallet. *GPS/IMU and LiDAR integration to aerial photogrammetry: Development and practical experiences with Helimap System.* Vorträge Dreiländertagung, vol. 27, 2007. (Cited on page 43.)

[Wu 2014] Changchang Wu. *Critical configurations for radial distortion self-calibration.* In Proceedings of the IEEE Conference on Computer Vision and Pattern Recognition, pages 25–32, 2014. (Cited on page 63.)

[Yastikli & Jacobsen 2005] Naci Yastikli and Karsten Jacobsen. *Influence of system calibration on direct sensor orientation.* Photogrammetric Engineering & Remote Sensing, vol. 71, no. 5, pages 629–633, 2005. (Cited on page 43.)